SYNTHESIS AND CHARACTERIZATION OF ZnMn₂O₄ AND PVDF/Ca-Al LDH NANOFIBERS FOR SUSTAINABLE ENERGY APPLICATIONS

Thesis

Submitted in partial fulfillment of the requirements for the degree of
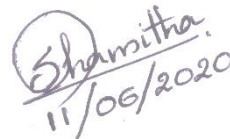
DOCTOR OF PHILOSOPHY

By

SHAMITHA C

DEPARTMENT OF METALLURGICAL AND MATERIALS ENGINEERING

NATIONAL INSTITUTE OF TECHNOLOGY KARNATAKA,

SURATHKAL, MANGALURU – 575 025

June, 2020

DECLARATION

By the Ph.D. Research Scholar

I hereby *declare* that the Research Thesis titled "**Synthesis and Characterization of ZnMn$_2$O$_4$ and PVDF/Ca-Al LDH Nanofibers for Sustainable Energy Applications**", which is being submitted to the **National Institute of Technology Karnataka, Surathkal** in partial fulfillment of the requirements for the award of the Degree of **Doctor of Philosophy** in **Metallurgical and Materials Engineering** is a *bonafide report of the research work carried out by me*. The material contained in this Research Thesis has not been submitted to any University or Institution for the award of any degree.

SHAMITHA C
Register number: 148024MT14F11
Department of Metallurgical and Materials Engineering
National Institute of Technology Karnataka, Surathkal

Place: NITK-Surathkal

Date: 11-06-2020

CERTIFICATE

This is to *certify* that the Research Thesis titled "**Synthesis and Characterization of ZnMn$_2$O$_4$ and PVDF/Ca-Al LDH Nanofibers for Sustainable Energy Applications**", submitted by **SHAMITHA C** (Register No: **148024MT14F11**) as the record of the research work carried out by her, is *accepted as the Research Thesis submission* in partial fulfillment of the requirements for the award of degree of **Doctor of Philosophy**.

Prof. S. Anandhan
Research guide
(Signature with date and seal)

Prof. K. Narayan Prabhu
Chairman-DRPC
(Signature with date and seal)

Dedicated to my beloved family, friends, and teachers …

ACKNOWLEDGEMENT

ABSTRACT

ZnMn$_2$O$_4$ (ZMO) and PVDF/Ca-Al LDH (PCAL) nanocomposite nanofibers were synthesized from using electrospinning technique. For the synthesis of ZMO nanofibers styrene-acrylonitrile random copolymer (SAN) was used as the sacrificial polymeric binder and the nanofibers were calcined at three different temperatures (773, 873, and 973 K). Structural, morphological and optical properties of these ceramic nanofibers were characterized. X-ray diffraction and X-ray photoelectron spectroscopy results revealed the presence of hexagonal ZnMnO$_3$ and MnO phases in the ZMO nanofibers produced. Based on the findings, a plausible mechanism of formation of ZMO nanofibers was proposed. The nanofibers calcined at 773 K exhibited a specific surface area of 79.5 m^2.g^{-1}, which is higher than that of the zinc manganite nanofibers synthesized hitherto by sol-gel electrospinning. The suitability of ZMO nanofibers was investigated as bifunctional electrocatalysts for water splitting towards Oxygen Evolution Reaction (OER) and Hydrogen Evolution Reaction (HER). The results demonstrate that ZMO nanofibers are promising candidate as bifunctional electrocatalysts for water-splitting applications.

A new synthetic route for Ca-Al layered double hydroxide (LDH) nanosheets was adapted and these two-dimensional nanosheets were used as filler for poly(vinylidene fluoride) (PVDF) to produce composite nanofibers by electrospinning. The polymorphism, crystallinity, and the interaction between PVDF and LDH were studied by Fourier transform infrared spectroscopy, X-ray diffraction, and differential scanning calorimetry. The synergetic effect of PVDF-LDH interaction and *in situ* stretching due to electrospinning facilitates the nucleation of electroactive β phase up to 82.79%, which makes it a suitable material for piezoelectric-based nanogenerators. The piezoelectric performance of PCAL nanofibers was demonstrated by hand slapping and frequency-dependent mechanical vibration modes, which delivered a maximum open-circuit output voltage of 4.1 and 5.72 V, respectively. Moreover, the applicability of PCAL nanofibers was explored in lithium-ion batteries (LIBs) as gel polymer electrolyte (GPE). The PCAL based GPE exhibited enhanced electrochemical properties, such as high ionic conductivity, optimal Li-ion transference number, and improved electrolyte uptake due to the presence of a highly interconnected porous

structure. They exhibited improved charge-discharge profile compared to pristine PVDF and commercial Celgard® 2400 separator membrane. Along with high electrochemical performance, the PCAL based GPE showed superior mechanical and low thermal shrinkage properties, indicating its suitability in battery separator application.

CONTENTS

LIST OF FIGURES

i

LIST OF TABLES

NOMENCLATURE

$\overline{\mathrm{M}}_w$	Weight average molecular weight
$\overline{\mathrm{M}}_V$	Viscosity average molecular weight
%	Percentage
°	Degree
°C	Degree Celsius
Å	Angstrom
AFD	Average Fiber Diameter
AFM	Atomic force microscopy
BE	Binding energy
BET	Brunauer-Emmett-Teller
BJH	Barrett-Joyner-Halenda
BPA	bisphenol A
CAL	Ca-Al layered double hydroxide
cm	Centimeter
CNC	Composite nanofiber
CP	Chronopotentiometry
CuK_{α}	Copper k-alpha
CV	Cyclic voltammetry or voltammograms
D	Dimensional
D	Crystallite size
DC	Direct current
DEC	Diethyl carbonate
DMAc	Dimethylacetamide
DMF	N,N-dimethylformamide
DMSO	Dimethyl sulfoxide
DSC	Differential scanning calorimetry
DTG	Derivative Thermogravimetric analysis

EC	Ethylene carbonate
EDS	Energy dispersive x-ray spectroscopy
eV	Electron volt
FESEM	Field Emission Scanning Electron Microscopy or Microscope
FTIR	Fourier transform infrared spectroscopy
g	Gram
GPE	Gel polymer electrolyte
h	Hour
HER	Hydrogen evolution reaction
IUPAC	International Union of Pure and Applied Chemistry
K	Kelvin
KOH	Potassium hydroxide
kV	Kilovolt
LDH	Layered double hydroxide
LDH	Layered double hydroxide
LIB	Lithium-ion battery
LSV	Linear sweep voltammetry or voltammograms
m	Meter
M	Molar
mA	Milliampere
min	Minute
mL	Milliliter
mm	Millimeter
mM	Millimolar
MnAc	Manganese (III) acetate tetrahydrate
mV	Millivolt

mW	Milliwatt
NaOH	Sodium hydroxide
nm	Nanometer
OER	Oxygen evolution reaction
PAN	Poly(acrylonitrile)
PCAL	Poly(vinylidene fluoride)/Ca-Al layered double hydroxide
PE	Poly(ethylene)
PP	Poly(propylene)
PS	Poly(styrene)
PVA	Poly(vinyl alcohol)
PVAc	Polyvinyl acetate
PVC	poly(vinyl chloride)
PVDF	Poly(vinylidene fluoride)
PVP	Poly(vinyl pyrrolidone)
RE	Reference electrode
rpm	Revolutions per minute
s	Second
SAED	Selected area electron diffraction
SAN	Poly(styrene-*co*-acrylonitrile)
SCE	Saturated calomel electrode
SD	Standard deviation
SEM	Scanning Electron Microscopy or Microscope
Tc	Crystallization temperature
TEM	Transmission Electron Microscopy or Microscope
TEOS	Tetraethyl orthosilicate
TGA	Thermogravimetry or Thermogravimetric
T_m	Melting temperature

UV	Ultraviolet
V	Volt
WE	Working electrode
wt%	Weight percentage
wt/v%	Weight by volume percent
XPS	X-ray photoelectron spectroscopy
XRD	X-ray diffraction
ZMO	$ZnMn_2O_4$
ZnAc	Zinc(II) acetate dihydrate
θ	Theta
λ	Wavelength

CHAPTER 1

CHAPTER I

INTRODUCTION AND LITERATURE REVIEW

This chapter gives a brief overview of nanofibers, their synthesis methods, and applications. An overview of sol-gel assisted electrospinning technique has been discussed. A brief literature review on inorganic and polymeric nanofibers, their synthesis method, and applications have been presented. Finally, the problem identification, scope, and objectives of the present work are discussed.

1.1. BACKGROUND

The concept of nanotechnology was first pointed out by the Nobel laureate Richard P Feynman during his lecture at the meeting of American Physical Society, titled "*There is plenty of room at the bottom*". He envisioned the possibility and potential of nanomaterials that inspired many researchers and led to various scientific developments in nanotechnology (Feynman 1992). The term "nanotechnology" was first introduced by Norio Taniguchi during a scientific conference held in Japan in 1974. According to Taniguchi, nanotechnology deals with the processing of separation, consolidation, and deformation of materials by one atom or by one molecule.

The prefix *nano* in nanotechnology refers to a billionth (1×10^{-9}). Nanomaterials are defined as the materials with any external dimensions in the nanoscale (size ranging from 1-100 nm) or materials with internal or external structures in the nanoscale (ISO/TS 80004-1 2015). Classifications of nanomaterials as per ISO standard are shown in Fig. 1.1. Nanomaterials are classified into nano-object and nanostructured materials (ISO/TS 80004-2 2015). Materials with one or more external dimensions at the nanoscale are termed as nano-objects, which is further classified into nanoplate, nanofiber, and nanoparticle, whereas nanostructured materials have internal or the surface structure at the nanoscale. Nanostructured materials are further classified as nanocomposites, materials with nanostructured surfaces, shell structures, and assembled nanomaterials. The nanofiber is a nano-object with two external dimensions in nanoscale and one dimension significantly larger than nanoscale, and the nanoplates have one external dimension in nanoscale and other two larger than nanoscale.

Nanoparticles are defined as the nano-objects having all the three dimensions in nanoscale.
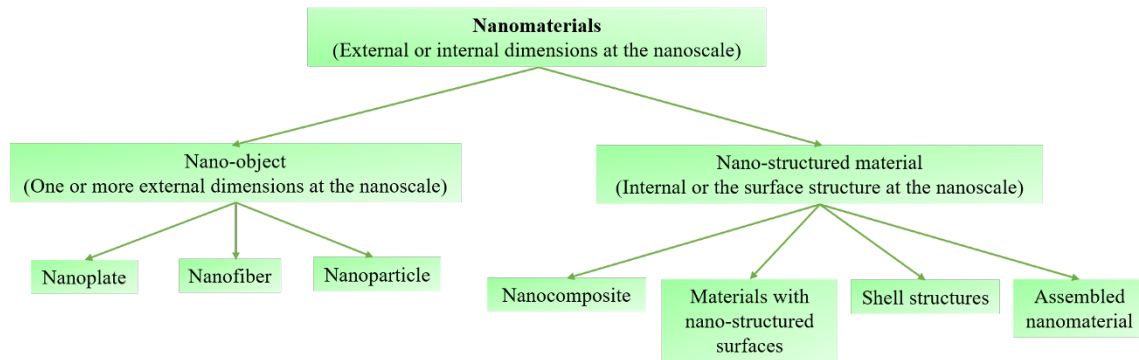
Fig. 1.1 Classifications of nanomaterials based on ISO specifications.

Among the various nanostructured materials, 1-D nanomaterials, including nanofibers, nanotubes, nanowires, and nanorods, have gained much research interest due to the unique properties exhibited by them. Apart from these nanomaterials, nanofibers possess special properties such as high surface to volume ratio, porosity, and morphological features. These unique properties are making them one of the attractive candidates in various applications such as biomedical, energy storage, water treatment, electrocatalysis, and sensing.

A variety of fiber-forming techniques are reported so far. Some of them are drawing, template synthesis, temperature-induced phase separation, molecular self-assembly, and electrospinning (Fig. 1.2). Among these techniques, electrospinning has gained significant attention due to its versatility and ability to produce uniform fibers in the range of nanoscale dimensions. The various fiber forming techniques are explained briefly.

Drawing: In this method, a micropipette is placed in a liquid droplet with the help of micromanipulator at the contact line and is released from the droplet with a speed of 1×10^{-4} ms^{-1} approximately (Alghoraibi and Alomari 2018). The nanofiber formed is being pulled by the micropipette and deposited on a surface by touching it with the tip of the micropipette. The process can be repeated several times to form continuous nanofiber. This method is limited to laboratory scale because nanofibers are produced

one by one and are time-consuming process. The fiber dimensions cannot be controlled and are operator dependent process.
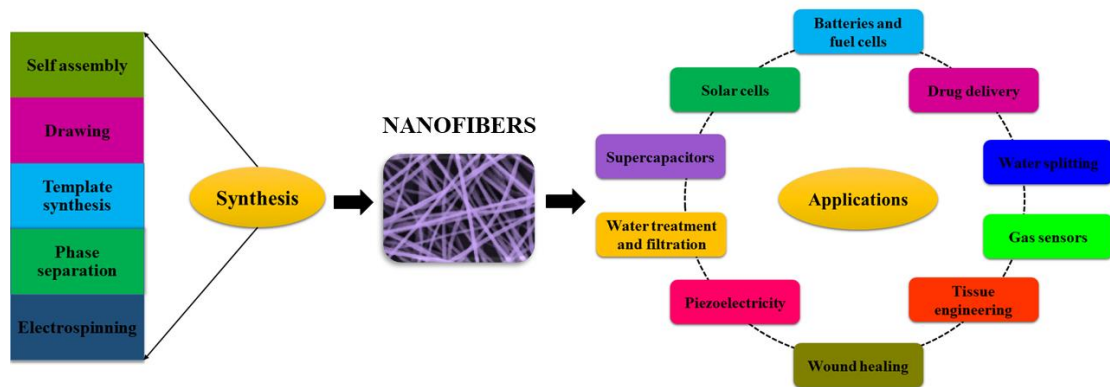
Fig. 1.2 Different synthesis techniques and applications of nanofibers.

Template synthesis: A template or mold of metal oxides with nanometer size pores is used to produce nanofibers of polymers, metals, and semiconductors. In this process, fibers are produced by passing the polymeric solution through the pores of the template by applying pressure on one side of the template (Zhang and Lu 2014). The fibers will be extruded through the nanopores of template when it comes in contact with the solution. The length of the fibers obtained through this method will be in microscale, and the dimension of the fiber mainly depends on the pore size of the template. The main difficulty associated with this process is the replacement of template and limited production.

Phase separation: As the name suggests, the phases will be separated due to physical incompatibility. The process involves polymer dissolution, gelation, phase separation, solution removal, and drying (Ramakrishna et al. 2005). A polymer will be dissolved in a solvent at elevated or room temperature and is maintained at gelation temperature. During gelation, the polymer gel will be formed due to the separation of phase and lead to the formation of nanofibrous matrix. This method involves a simple procedure with minimum equipment requirements. The nanofibers will be formed after the removal of water from the matrix and drying. All polymeric materials cannot undergo phase separation process, which limits the use of this method.

Table 1.1 Advantages and disadvantages of different fiber-forming techniques.

Technique	Advantages	Disadvantages
Drawing	• Single nanofibers can be produced one-by-one. • Simple process with minimal equipment requirement.	• Discontinuous process. • Limited to laboratory scale production.
Template synthesis	• Using different templates fibers of different diameters can be produced.	• Template replacement has to be done frequently. • Large scale production is not possible.
Phase separation	• Minimum equipment requirement. • Nanofiber matrix can be fabricated.	• Not possible to produce long continuous fibers. • Limited to specific polymers.
Self-assembly	• Smaller nanofibers can be produced.	• Complex technique. • Mass production is not possible. • Fiber dimensions cannot be controlled.
Electrospinning	• Cost-effective technique. • Continuous long fibers can be produced. • Simple equipment. • Large scale production of nanofibers from various polymers are possible.	• Several controlling parameters. • A skilled operator is required.

Self-assembly: The method is a bottom-up approach in which the small molecules combine to form patterns of structures through noncovalent forces (Yang and Xu 2007). Fibers of nanoscale dimensions can be produced by this method. The main driving force

in this method is the intermolecular forces that determine the overall dimensions and shape of nanofibers. Only short fibers can be produced by this method and it is a complicated process with a limited production of nanofibers. It is very difficult to control the dimensions of nanofibers.

Electrospinning: Electrospinning has been recognized as an efficient technique for producing nanofibers. The most interesting feature of this technique is that it is possible to produce fibers with diameters less than tens of nanometers, its simple equipment, and ease of handling. However, conventional synthesis techniques are time-consuming and require ultrapure precursors for the fabrication of high aspect ratio nanofibers. The electrospinning technique uses electrostatic force for the production of nanofibers. It is applicable to a variety of materials such as polymers, metals, semiconductors, ceramics, and composites. The electrospun nanofibers are widely used in several applications, including tissue engineering, wound dressing, filtration, and drug delivery.

Compared to other fiber-forming techniques, electrospinning has gained much research interest owing to its advantages such as low cost, large scale production of nanofibers with high aspect ratio. The comparison of electrospinning with various other fiber-forming techniques is presented in Table 1.1.

1.2. Electrospinning- An overview
1.2.1. Introduction

Electrospinning is an efficient technique to produce nanofibers of diameter less than 100 nm and length up to kilometers using an electrostatically driven polymeric solution or melt. The electrospinning process is derived from electrostatic spinning. The first observation on the electrostatic attraction of liquids was reported in the 16th century by William Gilbert. This was the first-ever record on the deformation of the liquid droplet and that was eventually termed as Taylor cone. Later in 1745, G.M. Bose discovered the electrohydrodynamic spraying of liquids (Malakhov et al. 2009). In 1900, J.F. Cooley filed the first patent on electrospinning that can be considered as the starting stage of an industrial process (Cooley 1902). A patent was issued to Formhals during 1934 for the production of cellulose acetate nanofibers (Formhals 1934). During the

succeeding years, he has published a series of patents that have become a topic of interest in the forthcoming years.

During the year of 1960s, Taylor started the study on electrospinning jet forming mechanisms. He observed that due to the interaction with the applied electric field the liquid droplet distorted to form conical shape which is known as Taylor cone (Taylor and Dyke 1969). Formation of continuous fibers from polymer melt such as polyethylene and polypropylene are reported by Larrondo and John Manley in 1981 (Reneker and Chun 1996). In 1996, Ranekar and Chun reported nanofibers from a variety of polymers, including nylon, polyethylene oxide, polyimide, polyaramid, DNA, and polyaniline. (Reneker and Chun 1996). Since then, many publications have been reported on electrospinning, which is increasing exponentially every year. Many advanced research on electrospinning process parameters was reported in the early 1990s. The spinnability of various polymers, polymer blends, copolymers, and polymer composites was explored during the subsequent years.

1.2.2. Electrospinning: Basic set up and mechanisms

The basic electrospinning set up consists of three main components, namely high voltage power supply, spinneret, and a grounded collector (Fig. 1.3). DC power supply ranging from 1-100 kV is used for electrospinning. The polymeric solution is loaded to the syringe with a stainless steel needle and the syringe is connected to the syringe pump. The flow rate of the solution can be adjusted using the syringe pump. When a high voltage is applied, the pendent droplet of the solution will get electrified and the droplet will experience electrostatic forces. Due to the interaction between the surface charge at the droplet and the coulombic force exerted by the external electric field, the droplet will get elongated to form a conical shape, which is known as Taylor cone. The schematic illustration of the Taylor cone formation is shown in Fig. 1.4 (a-b). When the voltage applied reaches the threshold value, the electrostatic force will overcome the surface tension of the droplet, which leads to the ejection of the liquid jet from the nozzle. This electrified liquid jet will undergo continuous stretching and whipping process that leads to the formation of continuous long fibers. During this process, the solvent will get evaporated and fiber diameter will reduce further to form ultrafine

fibers. These fibers are collected at the collector plate. Depending on the nanofiber requirement, the geometry, as well as the base material of collector, can be varied.
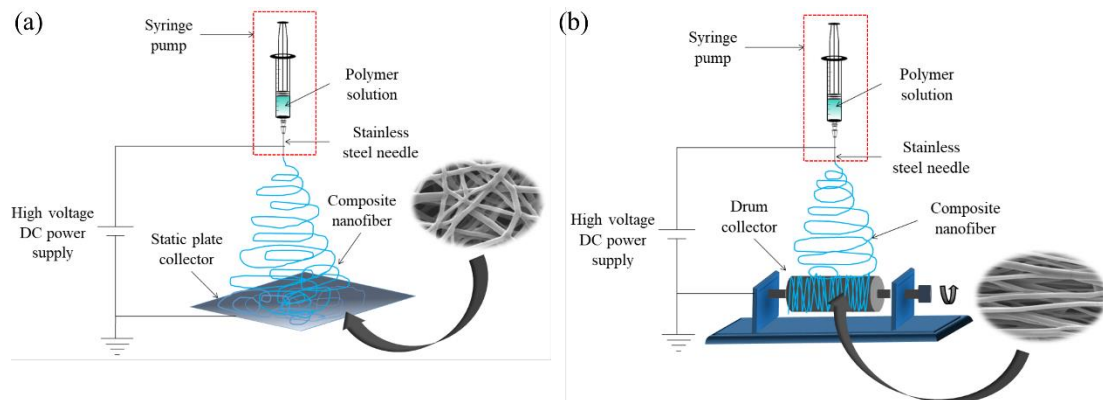
Fig. 1.3. Schematic of basic electrospinning set up with (a) static collector and (b) Rotating drum collector.
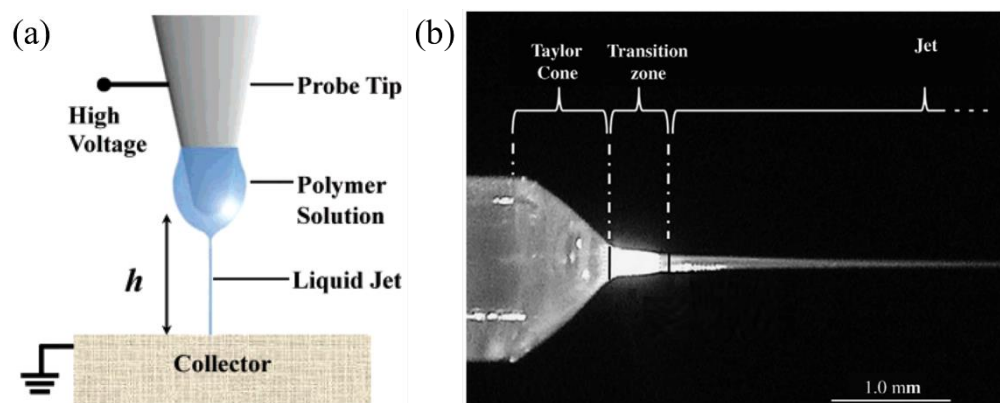
Fig. 1.4. (a-b) Schematic illustration of Taylor cone formation (Sun et al. 2006).

1.2.3. Influence of working parameters on electrospinning

Despite the fact that the electrospinning process gives off the impression of being an easily adaptable method, there are many other factors that have to be taken care of. The characteristic features of electrospun nanofibers mainly depend on the various parameters associated with the electrospinning process. The optimization of these parameters is an important challenge for the production of defect-free nanofibers, which greatly influence the morphology as well as the diameter of the fibers. The parameters that influence the electrospinning process are classified into three categories: solution

parameters, process parameters, and ambient parameters. Table 1.2 presents the various parameters that are influencing the electrospinning process.

Table 1.2 Influence of various parameters on the electrospinning.

Solution parameters:	♦ Polymer type
	♦ Molecular weight of polymer
	♦ Concentration of solution
	♦ Solution viscosity
	♦ Solution surface tension
	♦ Solution conductivity or surface charge density
	♦ Volatility of the solvent
	♦ Additives
Process parameters:	♦ Electric potential
	♦ Flow rate of solution
	♦ Geometry of the collector
	♦ Nozzle to collector distance
	♦ Spinneret diameter
	♦ Speed of rotating drum collector
Atmospheric parameters:	♦ Temperature
	♦ Humidity

Amidst other parameters, the concentration of the polymeric solution and applied voltage plays an important role in the electrospinning process. Deitzel et al. (2001) studied the influence of solution concentration and applied voltage on the electrospinning process. They observed that the applied voltage strongly depends on the formation of bead free fibers. As the voltage increases beyond the range, the formation of bead also increases. The solution concentration also plays an important role in electrospinning. The viscosity of the solution can be adjusted by varying the solution concentration. Also, with the increase in concentration, an increase in fiber diameter was observed. Solution concentration and fiber diameter follows power-law relationship. In addition to this, they have observed that the electrostatic effects also influence the morphological features of nanofibers, which lead to the formation of

heterogeneous structures. Ambient parameters such as temperature and humidity also affect the fiber diameter and morphology. So, the atmospheric conditions have to be considered during the electrospinning process.

1.3. INORGANIC NANOFIBERS

In addition to polymeric nanofibers, inorganic nanofibers also can be obtained by electrospinning. The electrospinning process is widely used for the production of polymeric nanofibers since it is very convenient to prepare nanofibers from the polymeric solution or melt with required morphological features. Whereas the fabrication of inorganic nanofibers requires additional experimental procedures to prepare the spinnable solution. Although it is possible to directly spin inorganic nanofibers from their melt; it requires a high temperature environment. The incorporation of the sol-gel method and electrospinning process is another method in which it is possible to obtain defect-free inorganic nanofibers with excellent morphological and structural features.
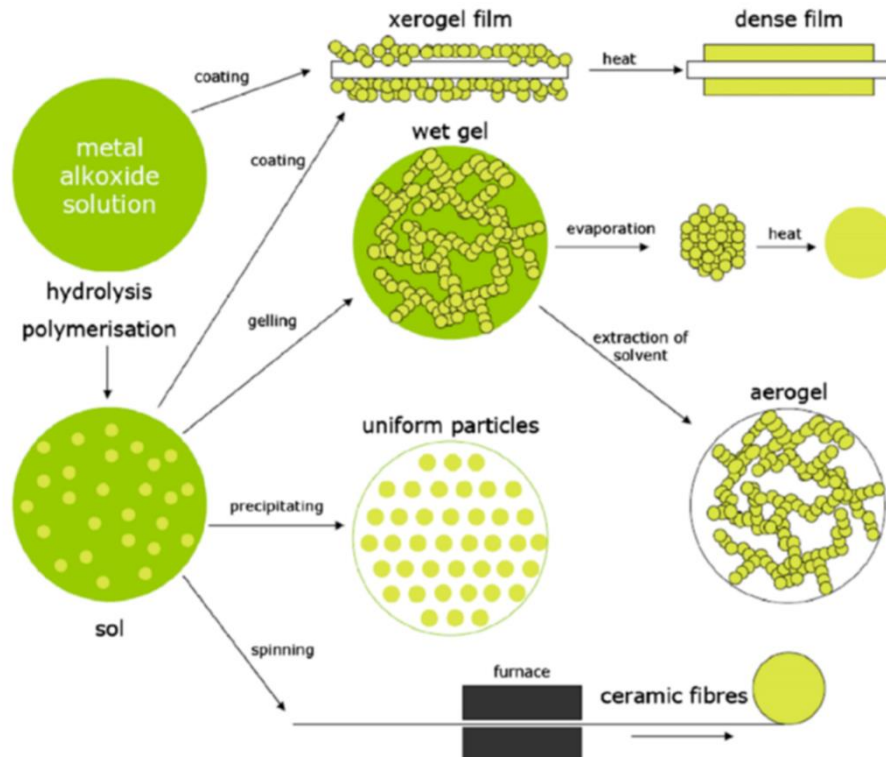
Fig. 1.5. Schematic representation of different steps associated with the sol-gel process (Cannavale et al. 2010).

Sol-gel process is a bottom-up approach in which small molecules are assembled to form solid materials. Sol is a suspension of solid particles in liquid and gel is an interconnected network surrounded by a liquid. This method provides better control of the overall process from molecular precursor to product, which is the special feature of sol-gel process. Metal alkoxides are the generally used precursors for the production of metal oxides by sol-gel process. Along with these metal acetates, nitrates, chlorides, sulfates are also used. The major steps involving in sol-gel process are hydrolysis, condensation, and drying. The metal precursors undergo hydrolysis and condensation process to form a suspension of polymers or fine particles called sol. The solidification of sol leads to the formation of wet gel. Further, the three-dimensional gel will be subjected to drying during which it will form aerogel or xerogel based on the drying method. The schematic representation of different steps associated with the sol-gel process is shown in Fig.1.5.

The sol-gel method is applicable to prepare a variety of materials with different shapes. The dense film can be made by heating the xerogel film obtained by coating. By spin coating or dip coating of viscous sol, coating films can be prepared. Heating of the gel leads to the formation of dense metal oxides. The formation of the final product mainly depends on the colloidal aggregates, so the synthesis conditions greatly affect the final structure and morphology of the product. Low processing temperature, high purity, possibility to fabricate coatings with a variety of shapes are the main advantages of this method (Muresan 2015).

1.3.1. Preparation of inorganic nanofibers through sol-gel electrospinning method

The inorganic nanofibers can be successfully prepared through sol-gel electrospinning method. The electrospinning of inorganic nanofibers depends on the spinnability of the precursor material. The preparation of inorganic nanofibers through sol-gel electrospinning consists of three steps such as, (i) preparation of spinnable sol that contains polymer matrix along with metal precursors, (ii) electrospinning of the solution to obtain composite nanofibers that contains both metal precursors and polymers, and (iii) sintering of composite nanofibers at high temperature to obtain inorganic nanofibers after the elimination of polymer matrix. The preparation of spinnable sol is the key step for the successful production of inorganic nanofibers.

The sintering process is an important step in the preparation of inorganic nanofibers. The morphology of fibers greatly depends on the sintering temperature. Different morphological features such as smooth/broken/short fibers, belt/ribbon type fibers, and hollow/porous fibers were observed depending on the sintering temperature, precursors, and polymer matrix (Esfahani et al. 2017). Apart from the usual fiber morphology, different morphologies such as irregular, flakes, and flower-like microstructures were also observed during the sintering process, an example of which is explained in Fig. 1.6. During this process, the material will undergo three stages; (i) elimination of solvents from the fiber, (ii) elimination of organic moieties that will lead to the shrinkage of fibers, and (iii) depending upon the temperature the inorganic fibers arrive glass transition temperature. In most of the cases, the sintering process ends with the stage (ii). During this process, temperature-driven crystallite growth takes place, in which atoms/ions diffuse to other stable positions about an interatomic distance. During this process, one crystallite grows at the expense of another (Park and Kim 2009).
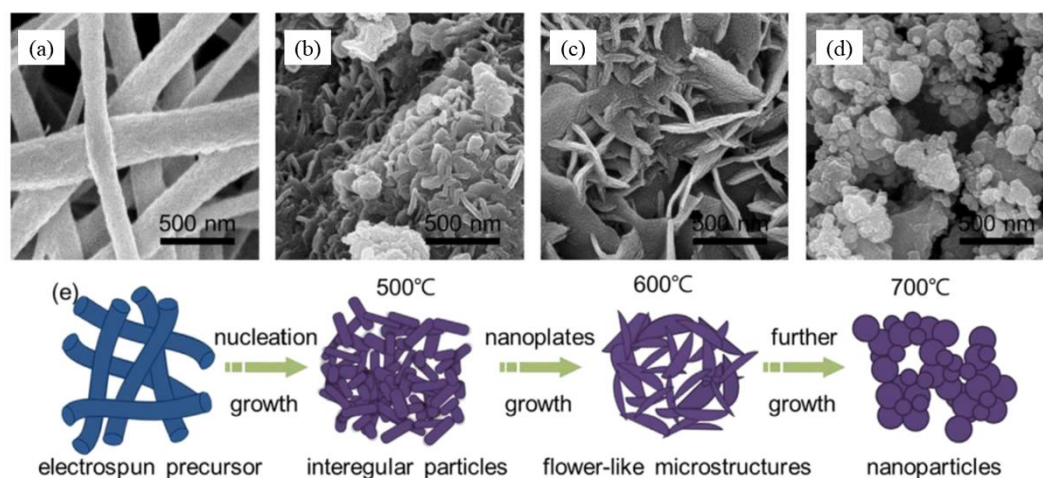
Fig. 1.6. SEM images depicting the schematic representation of the growth mechanism of PVA/$Li_{1.2}Ni_{0.17}Co_{0.17}Mn_{0.5}O_2$ nanofibers after calcination (Min et al. 2014).

Considerable research has been conducted to explore a variety of inorganic nanofibers due to the unique properties and potential applications exhibited by them. Lack of flexibility is the limitation in most of the ceramic materials. A variety of inorganic nanofibers through electrospinning process were reported so far, which is tabulated in Table 1.3. Starting from simple metal oxides to complex metal oxide nanofibers such as ZnO, SnO, NiO, CuO, TiO_2, SiO_2, MoS_2, Al_2O_3, CeO_2, Fe_2O_3,

11

BaTiO$_3$, LiMn$_2$O$_4$, NiTiO$_3$, NaCo$_2$O$_4$, MgTiO$_3$, NiFe$_2$O$_4$, LiCoO$_2$, LaMnO$_3$ were obtained by the electrospinning method. Polymers were used as the sacrificial binder for the preparation of inorganic nanofibers. The polymers should have good solubility in the chosen solvent, and should be also compatible with the precursor salts. A variety of polymers such as PVA, PVP, PVAc, SAN, PMMA was used as the matrix for the fabrication of inorganic nanofibers. Along with oxides, fabrication of non-oxides such as carbides, nitrides, sulfides and silicides were also obtained by the electrospinning technique. During the last decade, many researchers have developed inorganic nanofibers through sol-gel assisted electrospinning technique and used the same in applications such as catalysis, battery electrodes, supercapacitors, solar cells, and sensors.

1.3.2. Zinc manganites

Spinel oxides with the formula AB$_2$O$_4$ have gained much research interests owing to the interesting properties exhibited by them. They have been employed in a variety of applications, including energy storage, catalysis, and sensors (Kim and Ihm 2001; Padmanathan and Selladurai 2014; Rajesh et al. 2017). Transition metal oxides are important candidate materials in spinel-type oxides. Due to the different physical and physicochemical properties exhibited by them, these are appropriate materials for electrocatalysis and also suitable to use as anode and cathode materials for various applications.
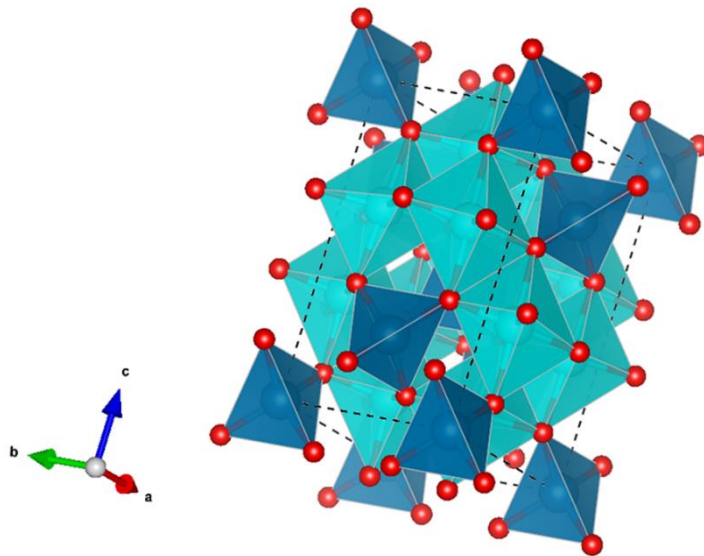
Fig. 1.7. The unit cell of spinel ZMO.

Currently, ZMO has gained attention among the transition metal oxides due to its potential applications, which include lithium-ion batteries, supercapacitors, sensors, and thermistors (Guan et al. 2016; Kim et al. 2013; Peng and Wu 2009; Zhao et al. 2014). It has various advantages compared to other transition metal oxides such as environmental friendliness, abundance, less toxicity, low cost, and low oxidation potential. The unit cell of spinel ZMO is shown in Fig. 1.7, which consists of tetragonally and octahedrally co-ordinated oxygen sublattices with Zn^{2+} and Mn^{3+} ions. Driessens and Rieck (1966) proposed a phase diagram explaining the formation of Zn-Mn-O in an air atmosphere (Fig. 1.8). The formation temperature of four phases, such as cubic, tetragonal, and zincite phases, were proposed. According to this phase diagram, the formation of tetragonal spinel ZMO takes place in the temperature range of 600 to 1000 °C. It has been reported that ZMO can be used as anode material for lithium-ion batteries. Luo et al. (2015) studied the electrochemical performance of ZMO nanofibers obtained by electrospinning for lithium-ion battery applications. They obtained high initial discharge capacity, high specific capacity, and good cyclic performance. Also, it can act as an efficient catalyst for the conversion of NO to N_2. Guillemet-Fritsch et al. (2000) reported that ZMO is a promising material for thermistor applications due to its electrical properties. ZMO nanoparticles are prepared by various synthesis methods such as hydrothermal method, co-precipitation method, solid-state method, flame spray pyrolysis, sol-gel synthesis, and electrospinning (Bessekhouad and Trari 2002; Courtel et al. 2012; Kim et al. 2011; Yang et al. 2014a). Among these methods, electrospinning has been recognized as an efficient technique for producing nanofibers.

The porous nature of nanofibers plays an important role in their performance in various applications. Bhagwan et al. (2018) studied the electrochemical performance of electrospun ZMO nanofibers. These nanofibers exhibited a high surface area of 30 m^2 g^{-1}, and a high specific energy density of 33.3 Wh kg^{-1} was observed at a power density of 500 W kg^{-1}. The high supercapacitive performance was ascribed to the morphological features and interconnected voids present, which gives accessibility to foreign ions. Yang et al. (2014b) developed interwoven nanofibers of ZMO with a porous structure. They studied the electrochemical performance of ZMO nanofibers for applications in LIBs. The nanofibers exhibited a reversible capacity of 658 mAh g^{-1} at

current densities of 400 mA.g^{-1} after 100 cycles. The high performance of ZMO nanofibers is due to their porous structure, which offers ion transport pathways and sufficient space to withstand the volume expansion during the lithiation process.
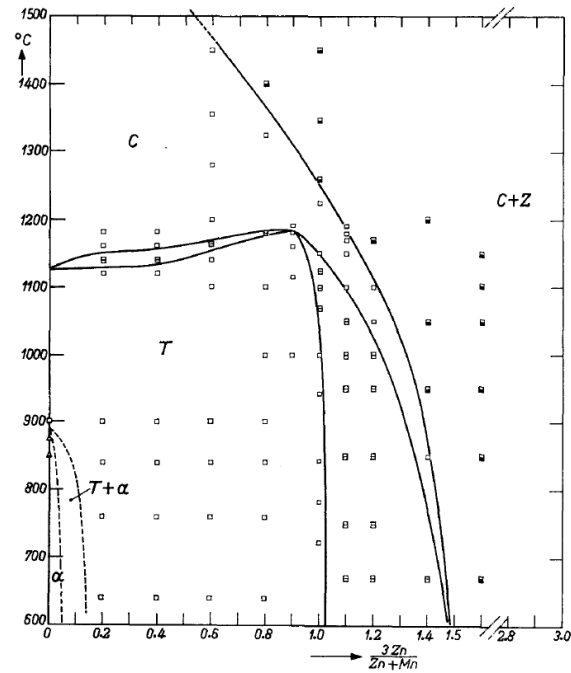
Fig. 1.8. Proposed phase diagram of the Zn-Mn-O system in air atmosphere (Driessens and Rieck 1966).

14

Table 1.3 Inorganic nanofibers obtained through the electrospinning technique.

Inorganic nanofibers	Precursors			Remarks	References
	Metal salts	Polymer	Solvent/Additives		
Al_2O_3	Aluminum 2,4-pentanedionate	PVP	Ethanol, Acetone	Transparent α-Al_2O_3 formed.	(Azad 2006)
Fe_2O_3–Al_2O_3	Iron acetylacetonate, Aluminum oxide hydroxide nanopowder	PVP	Ethanol, Acetone, Acetic acid	Efficient adsorbent for heavy metal ion removal.	(Mahapatra et al. 2013)
Al_2O_3	Aluminum isopropoxide	PVP	Ethanol, Nitric acid	Surface adsorption studies.	(Kim et al. 2014)
ZnO	Zinc acetate dihydrate	PVA	Ethanol, H_2O	Behavior of nanofibers at low AC electric field was studied.	(Ghashghaie et al. 2011)
ZnO	Zinc acetate dihydrate	PVA	H_2O	Biosensor application	(Stafiniak et al. 2011)
ZnO	Zinc nitrate hexahydrate	PVP	DMF, Ethanol	Explosive nitrocompounds detection	(Cao et al. 2016)

ZnO–CuO	Zinc acetate dehydrate, Copper acetate monohydrate	PVA	Ethanol, Acetic acid, H_2O	Dielectric studies	(Vijayakumar et al. 2010)
ZnO–SnO_2	Zinc acetate, Tin chloride dihydrate	PVA	H_2O	Morphological and optical studies.	(Asokan et al. 2010)
SnO_2	Tin chloride	PVA	H_2O	Gas sensor application.	(Zhang et al. 2008)
SnO_2	Tin chloride	PVP	DMF	Toluene sensing studies.	(Qi et al. 2009)
SnO_2	Dimethyldineodecanoate tin,	PEO	Chloroform	Rutile structure.	(Wang et al. 2004)
ZnO	Zinc acetate dihydrate	SAN	DMSO	Sol-gel assisted electrospinning. Ammonia gas sensing.	(Senthil and Anandhan 2014)
ZnO-SnO_2	Zinc chloride, Tin chloride	PVP	DMF	Sol-gel assisted electrospinning. Photocatalytic studies.	(Zhang et al. 2010b)

TiO$_2$	Titanium tetra isopropoxide	PVP	Ethanol	Dye sensitized solar cell application.	(Ilahi et al. 2017)
TiO$_2$	Titanium tetra isopropoxide	PVAc	Ethanol, Acetic acid	Degradation of dye pollutants.	(Doh et al. 2008)
TiO$_2$	Titanium(IV) butoxide	PVP	Methanol, Acetyl acetone	Sol-gel assisted electrospinning. Photocatalytic activity for hydrogen evolution.	(Chuangchote et al. 2009)
TiO$_2$ nanofiber/graphite oxide	Titanium tetraisopropoxide, Potassium chlorate, Graphite powder	PVP	Ethanol, Acetic acid	Electrochemical detection	(Arvand and Ghodsi 2014)
NiO	Nickel acetate	PVAc	DMF, Acetic acid	Anode material for Li-ion batteries	(Aravindan et al. 2013)
NiO	Nickel acetate	PVA	H$_2$O	Sol-gel assisted electrospinning.	(Guan et al. 2003)

NiO–ZnO	Nickel acetate, Zinc acetate	PAN	DMF	Sol-gel assisted electrospinning. Photocatalytic studies.	(Zhang et al. 2010a)
Ag/NiO	Silver nitrate, Nickel nitrate	PVA	H_2O	High electrical conductivity	(Wu et al. 2007)
NiO	Nickel (II) acetate tetrahydrate	SAN	DMF, Acetic acid	Sol-gel assisted electrospinning. Low temperature thermistor applications.	(George and Anandhan 2014)
CeO_2	Cerium nitrate	PVA	H_2O	High surface area.	(Yang et al. 2005)
Co_3O_4	Cobalt(II) acetate tetrahydrate	SAN	DMF	Electrocatalytic studies.	(George et al. 2015)
CeO_2–ZnO	Cerium nitrate, Zinc acetate	PVP	Ethanol, H_2O	Sol-gel assisted electrospinning. High photocatalytic activity.	(Li et al. 2011)
SnO_2–CeO_2	Tin chloride, Cerium nitrate	PVP	DMF, Ethanol	Highly porous. Gas sensor application.	(Qin et al. 2013)

Au/CeO$_2$	Cerous nitrate hexahydrate, Chloroauric acid tetrahydrate	PVP	DMF, Acetonitrile, Benzyl alcohol, Benzaldehyde	Photocatalytic studies.	(Li et al. 2017)
BaTiO$_3$	Barium titanium ethylhexano-isopropoxide,	PVP	Isopropanol, acetoacetone,	Ribbon-like nanofibers. Ferroelectric applications.	(McCann et al. 2006)
BaZrO$_3$	Barium acetate, zirconium 2, 4-pentadionate,	PVP	Glacial acetic acid	Mechanical reinforcement.	(Calleja et al. 2016)
NiFe$_2$O$_4$	Nickel ethylhexanoisopropoxide, Iron(III) ethylhexano-isopropoxide	PVP	Acetic acid, Isopropanol	Magnetic properties.	(Li et al. 2003)
MgTiO$_3$	Magnesium ethoxide, titanium isopropoxide	PVAc	DMF, 2-methoxyethanol	Catalyst	(Dharmaraj et al. 2004)
NaCo$_2$O$_4$	Sodium acetate trihydrate, Cobalt (III) acetate tetrahydrate	PAN	DMF	Polycrystalline nature.	(Maensiri and Nuansing 2006)

Mn_2O_3–Mn_3O_4	Manganese acetate	PVA	H_2O	Modified sol-gel assisted electrospinning.	(Shao et al. 2004)
$LiMn_2O_4$	Lithium nitrate, Manganese(II) acetate tetrahydrate	PVP	Ethanol, H_2O	Cathode material for lithium ion batteries.	(Zhou et al. 2014)
Nickel titanate	Nickel (II) acetate tetrahydrate, Titanium (IV) isopropoxide	SAN	DMF	Sol-gel assisted electrospinning. Presence of ilmenite and spinel phases. Bifunctional electrocatalyst towards HER and OER.	(Sachin Kumar et al. 2019)
$NiCo_2O_4$	Nickel (II) acetate tetrahydrate, Cobalt (II) acetate tetrahydrate	SAN	DMF	Sol-gel assisted electrospinning. Electrocatalyst for glucose sensing and water-splitting applications.	(Kumar et al. 2019)

1.4. POLYMERIC NANOFIBERS

Electrospinning is a highly convenient method for the preparation of polymeric nanofibers. Till now enormous number of polymeric nanofibers such as the ones from PP, PE, PVP, PVA, PVAc, PVC, PAN, CA and PS were prepared through electrospinning process (Gu et al. 2005; Han et al. 2008; Itoh et al. 2016; Li et al. 2016; Ma et al. 2015; Matysiak et al. 2018; Veerabhadraiah et al. 2017; Wang et al. 2010). In this process, the polymers will be dissolved in an appropriate solvent to form a polymeric solution. The spinnability of the polymeric solution is the main challenge associated with the production of polymeric nanofibers. Along with the polymeric solution, polymer melt also can be used for electrospinning. In this case, instead of polymer solution, polymer melt will be introduced into the capillary tube and the required processing temperature has to be maintained accordingly.

Once the spinnability of the polymeric solution is achieved the next target is to obtain continuous long defect-free fibers with controllable fiber diameter. The fiber diameter depends on the solution and the process parameters. So the fiber diameter can be controlled by varying these parameters. Production of defect-free fiber is another challenge. Polymer concentration plays an important role in the formation of beads. It was reported that higher the polymer concentration less will be the bead formation. The optimum concentration has to be selected for the preparation of bead free fibers. The addition of fillers also leads to a reduction in bead formation. The addition of fillers results in high charge density, higher stretching, and whipping process under the influence of the electric field, which leads to the formation of uniform long continuous defect-free fibers with a smaller diameter.

A large number of polymer and polymer composite nanofibers are developed so far. The polymer-based nanofibers are employed and are used in a broad range of applications such as tissue engineering, sensors, water treatment, piezoelectric, battery separators, aerospace, and fuel cells. Among these, energy harvesting applications have gained much research interest owing to the rising interest for convenient electronic gadgets due to the ever-expanding human lifestyle. However, it is incredibly recommended to use sustainable energy sources to minimize the utilization of fossil fuels in order to avoid energy crisis. Gathering mechanical energy from the surrounding

environment has turned into an attractive route to power different electronic devices and self-powered gadgets, because of the abundance of mechanical sources in the form of vibrations, air flow, breathing, blood flow, heart beating, and human body movements. Wang and Song (2006) introduced the possibility of piezoelectric nanogenerator by moving the atomic force microscopy tip over vertically developed ZnO nanowires. The piezoelectric mechanism can be portrayed that, when a mechanical vibration or stress is applied on a piezoelectric material, breaking of center of symmetry in the crystal structure will take place, which leads to the formation of piezoelectric potential (Fan et al. 2016). A wide range of materials with relatively high piezoelectric performance has been studied enormously. Polymer based nanofiber materials have proven to be the best candidate for piezoelectric applications due to their flexibility and environment friendliness.

1.4.1. Poly(vinylidene fluoride)

Poly(vinylidene fluoride) (PVDF) is a renowned polymer that has gained tremendous popularity due to its flexibility, mechanical stability, thermal stability, and chemical inertness. PVDF exhibits excellent piezoelectric, ferroelectric, and pyroelectric properties, and PVDF-based systems have already proven their feasibility in various applications such as battery separators, ion exchange membranes, piezoelectric nanogenerators, sensors, and water purification. PVDF is a semicrystalline polymer, which exhibits five distinct phases α, β, γ, ε, and δ (Martins et al. 2012). Among these phases, the nonpolar α phase is the most stable one, and the polar β phase is the most electroactive one. The chemical structures of α, β, γ phases of PVDF are shown in Fig. 1.9.

The β phase induces spontaneous polarization and piezoelectric performances due to the presence of uniformly oriented molecular chains. Literature reveals that mechanical stretching, electric poling, spin coating, and the addition of suitable nanofillers induce significant enhancement in the β phase of PVDF. Among the various methods to produce nanofibers, electrospinning is the most effective one to produce piezoelectric nanofibers. This is due to the presence of a high stretching force that acts on the electrospinning jet and the in situ poling that leads to the formation of selfpoled piezoelectric nanofibers. The addition of various nanofillers into PVDF is another method to enhance the β phase, which will further improve the piezoelectric

performance. Large number fillers such as $BaTiO_3$, ZnO, TiO_2, SiO_2, Al_2O_3, CNTs, and graphene are incorporated into PVDF to improve its performance in various applications. Table 1.4 shows some of the PVDF based materials reported so far and their applications. Furthermore, there is a large demand for high dielectric constant materials due to the rapid growth in the field of energy storage devices. Compared to ceramic materials, polymeric materials with a high dielectric constant are preferred because of their flexibility, ease of fabrication, low cost, and lightweight. The enhancement of piezoelectric, as well as dielectric performance by the addition of suitable nanofillers into PVDF, is still an ongoing challenge to researchers.
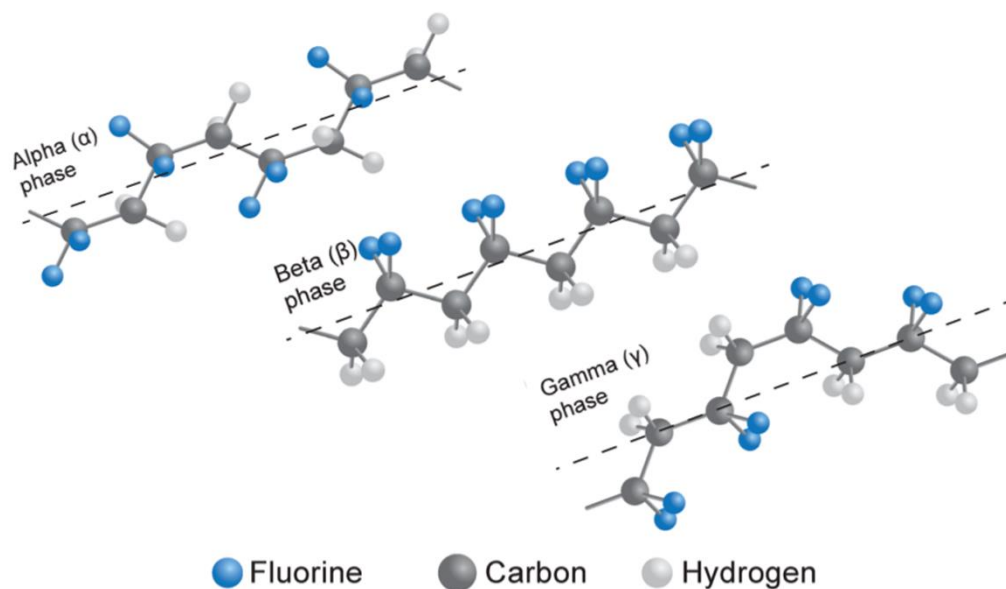
Fig. 1.9. Chemical structure of α, β, and γ phases of PVDF (Shepelin et al. 2019).

Table 1.4. Various PVDF based materials and their applications.

Material	Method of preparation	Precursors	Potential applications	Remarks	References
PVDF/MWCNT	Solution cast	PVDF, MWCNT, DMF	Memory devices	β phase formation after the addition of CNT. Exhibited memory effect in both positive and negative bias conditions.	(Manna and Nandi 2007)
PVDF	Electrospinning	PVDF, DMF, Acetone	Piezoelectric force sensor	Flexible force sensor without poling treatment. Excellent sensitivity and response to mechanical forces.	(Wang et al. 2011)
PVDF/TiO$_2$	Hot pressed technique	PVDF, TiO$_2$, DMAc	Organic pollutant decomposition from wastewater	Exhibited good morphological, structure and physical properties. highest photocatalytic activity in the degradation of BPA under UV irradiation.	(Nor et al. 2016)
PVDF/ZnO	Electrospinning	PVDF, ZnO, DMF, THF	Piezoelectric nanogenerator	Uniform morphological features. Maximum output power of 32 nW/cm^2	(Mansouri et al. 2019)

PVDF/BaTiO$_3$/ Graphene	Electrospinning	PVDF, BaTiO$_3$, Graphene, DMF	Piezoelectric nanogenerator	β phase enhancement. Maximum output power of ~ 4.1 μW at the resistance of 6.9 MΩ. In finger press-release mode maximum output voltage of 112 V.	(Shi et al. 2018)
PVDF/TiO$_2$	Spin coating	PVDF, TiO$_2$, DMF, Acetone	Humidity sensor	Surface roughness is achieved through acetone etching. Response and recovery times are 45 s and 11 s.	(Mallick et al. 2019)
PVDF/Al$_2$O$_3$	Phase-inversion method	PVDF, Al$_2$O$_3$, DMAc, PVP, sodium hexaphosphate	wastewater treatment and its antifouling research	Improved antifouling performance. Higher flux recovery and less contaminants adsorption.	(Yan et al. 2009)
PVDF/SiO$_2$	Diffusion induced phase separation	PVDF, TEOS, Ethanol, ammonium solution, DMF	salty oil emulsion separation	Pore size, porosity and surface roughness of PVDF increased after SiO$_2$ addition. Enhancement in hydrophilicity	(Ngang et al. 2017)

PVDF/PAN	Thermally induced phase separation	PVDF, PAN, DMSO	LIB separator	Enhanced tensile strength and thermal stability. Good reversible charge/discharge cycle stability.	(Wu et al. 2016)
PVDF/halloysite	Electrospinning	PVDF, Halloysite, DMSO,	Gel polymer electrolyte for LIB	β phase enhancement. High ionic conductivity, tensile strength and low thermal shrinkage. High capacity of 138.01 mAhg^{-1} with 97% coulombic efficiency for the initial cycle.	(Khalifa et al. 2019a)
PVDF/Iron oxide	Solution cast	PVDF, Iron acetylacetonate, Phenyl ether, Oleic acid, DMF, THF	Piezoelectric application	Enhancement in piezoelectric response and thermal stability.	(Ouyang et al. 2015)
PVDF/CNCs	Electrospinning	PVDF, CNCs, DMF, Acetone, Sulfuric acid	Piezoelectric application	Maximum piezo-voltage of 60 V is obtained.	(Fu et al. 2017)

PVDF/Zn:Al LDH	Spin coating	PVDF, Zn:Al LDH, DMF, THF	Piezoelectric nanogenerator	Output voltage of 4.9 V and current density of 0.47 μA cm^{-2}. After poling output voltage of 6.24 V and current density of 0.655 μA cm^{-2} obtained.	(Nguyen et al. 2018)
PVDF/g-C$_3$N$_4$	Electrospinning	PVDF, Thiourea, DMF, Acetone	Piezoelectric nanogenerator	Improved the spinnability and β-phase content. Maximum piezoelectric voltage of ~7.5 V and a current output of 0.23 μA.	(Khalifa et al. 2019b)
PVDF/Ni-Co LDH	Electrospinning	PVDF, Ni-Co LDH, DMF, Acetone	Piezoelectric nanogenerator	β phase enhancement. Maximum output voltage of 6.9 V and power density of 0.91 $\mu W/cm^2$.	(Shetty et al. 2019)
PVDF/MWCNT	Electrospinning	PVDF, MWCNT, DMAc, Acetone	Piezoelectric nanogenerator	High β-phase content. Enhancement of the ferroelectric and piezoelectric properties observed.	(Ahn et al. 2013)

1.5. PROBLEM IDENTIFICATION

Due to the inadequacy of fossil fuels and ever-expanding human life style there is a huge demand for energy. Currently, researchers are working on renewable and cleaner energy generation. In this way, nanomaterials play an important role in energy-related applications. Among the various nanomaterials, 1-D nanofibers have gained much research interest due to their unique properties such as high surface to volume ratio, porosity, and morphological features. Various methods are available to produce nanofibers; among them, electrospinning has been recognized as an efficient technique for producing nanofibers. The most interesting feature of this technique is that it is possible to produce fibers with diameters less than tens of nanometers, its simple equipment, and ease of handling. However, conventional synthesis techniques are time-consuming and require ultrapure precursors for the fabrication of high aspect ratio nanofibers.

Until now there is no study reported in literature on ZMO nanofibers obtained by sol-gel assisted electrospinning technique using poly(styrene-*co*-acrylonitrile) (SAN) as sacrificial polymeric binder. George and Anandhan (2015) studied the influence of polymeric binder on structural and morphological properties of sol-gel electrospun Co_3O_4 nanofibers. They observed that the morphological features of those fibers were improved when SAN was used as a binder compared with a water soluble binder. This is due to the ability of SAN to withstand high temperature, and the presence of styrene groups that acts as a structural unit for the morphological transformation during calcination of the polymer/ceramic precursor nanofibers. So, selection of polymeric binder plays a crucial role in the processing of ceramic nanofibers. So in this work ZMO nanofibers were synthesized by sol-gel assisted electrospinning technique using SAN as sacrificial polymeric binder and studied their structural, morphological and optical properties.

Among the polymeric nanofibers PVDF based systems possess tremendous popularity due to their flexibility, mechanical stability, thermal stability, and chemical inertness. Moreover, they exhibit high piezoelectric coefficient compared to other polymers. Literature reveals that mechanical stretching, electric poling, spin coating and the addition of suitable nanofillers induce significant enhancement in the β-phase

of PVDF. A group of materials including layered double hydroxide (LDH) also known as hydrotalcite-like compounds were proposed as fillers in polymer composites to improve the mechanical, and electrical properties. The presence of hydroxyl groups at the surface of LDH makes it a major hydrogen bond donor that is beneficial for piezoelectric and dielectric performance. So in this work, LDH was employed as a filler material to PVDF and their possible applications in sustainable energy were explored.

1.6. SCOPE AND OBJECTIVES OF THE PRESENT WORK
1.6.1. Scope

Electrospinning has been recognized as an efficient, cost-effective technique for producing nanofibers. Inorganic nanofibers have attracted attention of researchers due to the unique properties and potential applications exhibited by them. Due to the different physicochemical properties exhibited by them, these are appropriate materials for electrocatalysis and also electrode materials for various applications. ZMO is one of the promising spinel-type transition metal oxides. Among polymeric nanofibers, PVDF based materials have proven to be the best candidate for energy harvesting applications due to their flexibility, mechanical stability, thermal stability, and chemical inertness. This work aims at the production of ZMO and PVDF based nanofibers by electrospinning technique and study their suitability in energy related applications.

1.6.2. Objectives

- Production of ceramic nanofibers by calcination of the composite nanofibers (ZMO).
- Production of PVDF/Ca-Al layered double hydroxide composite nanofibers through electrospining.
- Evaluation of structural, morphological and spectral properties of nanofibers using X-ray diffraction (XRD), Scanning electron microscopy (SEM), Fourier transform infrared (FTIR) spectroscopy, Energy dispersive X-ray spectroscopy (EDS), Ultraviolet-visible (UV) spectroscopy and Transmission electron microscopy (TEM).
- To study the suitability of
    - ZMO nanofibers for water splitting applications.

- PVDF/Ca-Al LDH nanofibers for piezoelectric nanogenerator and battery separator applications.

CHAPTER 2

CHAPTER 2

MATERIALS AND METHODS

This chapter discusses the materials used for the fabrication of ZMO and PCAL nanofibers through electrospinning technique and studies their suitability in various energy related applications. Part-I consists of the synthesis procedure for ZMO nanofibers using SAN as a sacrificial polymeric binder followed by calcination at different temperatures. Part-II comprises the details of the fabrication of PCAL nanofibers.

PART-I

2.1. MATERIALS

SAN (Grade: Santron IMS 1000, acrylonitrile content: 30%, specific gravity: 1.07, viscosity average molecular weight $(\overline{M_V})$: 2.46×10⁶) was purchased from Bhansali Engineering Polymers, Rajasthan, India. Zinc(II) acetate dihydrate (ZnAc, minimum assay 99.5%) and manganese (III) acetate tetrahydrate (MnAc, minimum assay 99.5%) were obtained from Otto Chemie Pvt. Ltd, Mumbai, Maharashtra, India. N,N-dimethylformamide (DMF) of purity >99.5% was procured from Sisco Research Laboratories Pvt. Ltd, Mumbai, India. Potassium hydroxide (KOH) pellets (assay>99%) was procured from Nice Chemicals Pvt. Ltd, Mumbai, India. PVDF with molecular weight $(\overline{M_W})$ of 5.75×10⁵ (Solef® 1015, Solvay, Belgium) was obtained from Prakash Chemicals Pvt. Ltd, Gujarat, India. Commercial platinum on graphitized carbon (Pt/C) (20 wt% loading) and ruthenium (IV) oxide (RuO₂) (99.9% assay) were procured from Sigma-Aldrich, India. The graphite rods (10 mm diameter) for preparing the electrode were purchased from Specialty Graphites, Karnataka, India. All these chemicals were used without further purification.

2.2. METHODS

2.2.1. Electrospinning of SAN/ZnAc/MnAc composite nanofiber mats

In a typical synthesis, 2.4 g of SAN was added to 10 mL of DMF in a closed vial and was continuously stirred for 4 h. Subsequently, stoichiometric amounts of the metal

acetates were added to the polymer solution and the mixture was vigorously stirred to obtain a homogeneous solution. Polymer to metal salt ratio was kept at 1:1. The spinnable sol obtained was then loaded to a 10 mL hypodermic needle (inner diameter: 0.5 mm) with a beveled tip. The syringe was then loaded to the vertical electrospinning unit (E-Spin Nano, Physics Equipments Co., Chennai, India). SAN/ZnAc/MnAc composite nanofiber (CNF) mats were electrospun from the prepared sol under the following optimized conditions: applied electric voltage- 25 kV; feed rate of sol- 0.4 mL.h^{-1}; relative humidity- 50%; working distance- 17 cm; and rotating drum speed- 1050 rpm. The electrospinning led to the formation of long and uniform fibers in the form of thin mats on the collector plate, which was covered with aluminum foil. The fiber mats were then peeled off the aluminum foil.

2.2.2. Synthesis of ZMO nanofibers

The CNF mats obtained were calcined at three different temperatures (773, 873, and 973 K) in a programmable high temperature furnace (Indfur, Chennai, India). The heating rate used was 2 K.min^{-1} and the dwell time was 2 h. The calcination temperatures were carefully chosen based on the thermogravimetric analysis (TGA) carried out on the CNF mats.

PART-II

2.3. MATERIALS

Calcium nitrate tetrahydrate (minimum assay 99.5%) and aluminum foil (purity 99.9%, 0.14$\pm$0.01 mm thickness and 76$\pm$1 mm width) were obtained from Molychem, Mumbai, India. Sodium hydroxide pellets (NaOH, minimum assay 98%) and PVDF of $\overline{M_W}$= 5.75$\times$10^5 (Solef® 1015, Solvay, Belgium) were purchased from Central Drug House (P) Ltd., New Delhi, India, and Prakash Chemicals (P) Ltd., Vadodara, Gujarat, India, respectively. DMF (99% pure) was purchased from Molychem, Mumbai, India. EC, DEC and n-butanol of purity > 99% were purchased from Sigma Aldrich (Bengaluru, India). The commercial LiCoO$_2$ electrode was procured from MTI Corporation (Richmond, USA). Celgard® 2400 separator membrane was purchased from Hohsen Corporation, Japan. All these chemicals were used as received without further purification.

2.4. METHODS

2.4.1. Synthesis of CAL Nanosheets

The Ca-Al LDH nanosheets were synthesized by co-precipitation method under room temperature. A new approach has been introduced for the synthesis procedure, which is schematically illustrated in Fig. 2.1. In this synthesis technique, small pieces of Al sheets were added to an aqueous solution of $Ca(NO_3)_2.4H_2O$ (0.315 M). The molar ratio of Ca^{2+} and Al^{3+} was maintained at 1:2. An aqueous solution of NaOH (0.75 M) was added dropwise to this solution until the final pH reached *ca.* 11-12, the region of coprecipitation. The white precipitate formed was then aged for 24 h under vigorous magnetic stirring. All these processes were carried out in N_2 atmosphere in order to avoid contamination due to atmospheric CO_2. The resulting white precipitate was centrifuged several times with milli-Q water (ultrapure) and finally dried in vacuum at 50 °C.
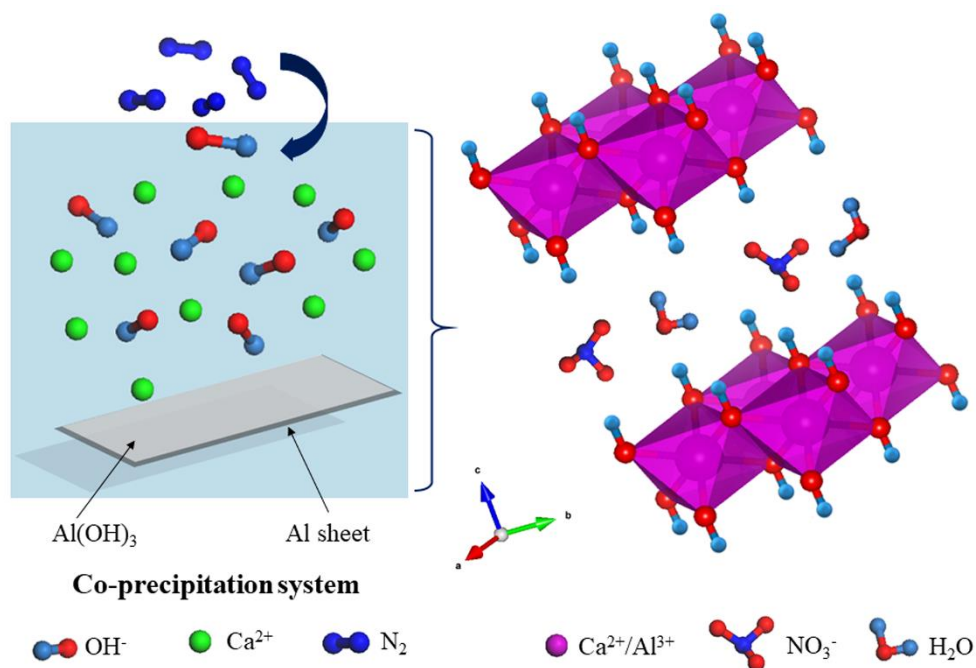
Fig. 2.1. Schematic illustration of the co-precipitation method for the synthesis of Ca-Al LDH nanosheets.

2.4.2. Electrospinning of PCAL Composite Nanofibers

PVDF solutions were prepared by dissolving PVDF powder (13.5 wt/v%) in a mixed solvent of DMF and acetone (volume ratio 9:1) via continuous magnetic stirring under

room temperature. The desired amount of synthesized CAL powder (2.5, 5, 7.5, 10, and 12.5 wt%) was added to the solution after dissolving the PVDF completely. Before the addition, CAL powder was dried in vacuum at 60 °C for 2 h and dispersed in DMF using an ultrasonic bath for 2 h at room temperature. In order to ensure homogeneous dispersion, the resulting solution was vigorously stirred for 5 h. The spinnable solution obtained was then transferred to a 10 mL syringe with a hypodermic needle (22-gauge, 0.5 mm inner diameter), and the syringe was then loaded to a vertical electrospinning unit (procured from E-spin nano, Physics Equipments Co., India). The optimal process parameters for electrospinning are applied voltage 20 kV, feed rate 0.8 mL.h^{-1}, spinneret tip to collector distance 16 cm, rotating drum collector speed 1050 rpm, and relative humidity 50%, respectively. The electrospun nanofibers were collected on an aluminum foil, which was wrapped on the collector plate. The electrospun fabric was peeled off to carry out further characterization.

2.4.3. Preparation of GPEs

The activated GPE of PVDF and PCAL was prepared by impregnating the respective nanofiber mat in 1 M LiPF$_6$ electrolyte in EC: DEC (1:1 v%) for 2 h and used for electrochemical studies. The excess electrolyte was wiped off by tissue paper without disturbing the membrane for further use.

2.5. MEASUREMENT AND CHARACTERIZATION

The morphological features of the electrospun nanofibers were studied using, an SEM (JEOL JSM-6380LA, Japan) equipped with an EDS at accelerating voltage of 20 kV. A fine layer of gold was sputtered (JFC 1600 auto fine coater, JEOL Ltd., Japan) on the samples prior to SEM imaging. The fiber diameters of 50 fibers were measured at three different points of each fiber using ImageJ 1.51n software (National Institute of Health, USA). Further, HRTEM (JEOL/JEM 2100, Japan) and FESEM (JSM-7500F, JEOL, Japan) was used to image the ZMO nanofibers obtained at different calcination temperatures. Prior to HRTEM imaging, the nanofibers were dispersed in ethanol using ultrasonication; a drop of the dispersion was placed on a copper grid and was dried thoroughly. The TEM (JEM 2100, JEOL Ltd., Japan) imaging of CAL was carried out by drop casting the suspension of LDH powder on carbon-coated 200 mesh copper grid. Prior to that, the LDH powder was dispersed in ethanol by ultrasonication. A drop of

dispersion was placed on the copper grid and was vacuum dried at 30 °C for 5 h. Alternatively, PCAL composite nanofibers were directly electrospun on the copper grid for 10 s followed by vacuum drying at 30 °C for 12 h.

FTIR (Jasco FTIR-4200, Japan) in transmission mode was obtained to ascertain the complete degradation of the organics during the calcination of the composite fibers and crystalline phase identification for an average of 32 scans and resolution of 2 cm^{-1} in the wavenumber range of 400-4000 cm^{-1}.

The thermal behavior of nanofibers was examined using DSC (Mettler Toledo, USA) and TGA (Q5000 V3.10 Build 258, TA Instruments) analysis. The DSC measurements were carried out in a nitrogen atmosphere at a thermal ramp of 10 °C.min^{-1} in a temperature range of 25-250 °C, and TGA was carried out in a temperature range of 25-900 °C at a heating rate of 10 °C.min^{-1}.

XRD (Rigaku Miniflex 600, Japan) was used to identify the phase formation in nanofibers. In PCAL composite nanofibers, XRD was used to examine the formation of CAL and the crystalline modification occurring in PVDF nanofibers after the incorporation of CAL.

To study the optical properties of ZMO nanofibers, UV-Vis NIR spectra (Cary 5000 UV-Vis-NIR, USA) were obtained in DRS (diffuse reflectance) mode in the wavelength range of 215-2400 nm. Raman spectroscopy (Labram HR800 Evolution, Japan) was used to study the vibrational modes of ZnMn2O4 nanofibers in the wavenumber range of 400-4000 cm^{-1} using Nd: YAG laser at a wavelength of 532 nm.

For the speciation of the elements in ZMO nanofibers, XPS was used and the spectra (Thermo Fisher Scientific ESCALAB250Xi, USA) were acquired using monochromatic AlKα radiation (15 kV, 6 mA). Specific surface area and porosity of ZMO nanofibers were measured using BET and BJH methods (NOVA-1000, USA).

The piezoelectric voltage measurements were carried out using an oscilloscope (Analog discovery 2 USB, Digilent Inc.). The piezoelectric response by mechanical vibration mode was done using a function generator (Agilent 33220A), power amplifier (CEDRAT Technologies, CA45, France), and piezoelectric stack actuator (CEDRAT Technologies, PPA80L, France). The dielectric measurements were carried out in an impedance analyzer (Agilent 4294A) over a frequency range of 1000 Hz-1 MHz.

The AFM imaging of nanofibers was carried out using an atomic force microscope (AFM, Agilent 5500, USA) with silicon tip in tapping mode to study the morphological features and apparent roughness of GPE. The ionic conductivity of GPE was studied using AC impedance spectroscopy (Hioki 3532-50 LCR tester) by sandwiching the GPE in between two stainless steel electrodes (SS) and assembled into a CR2032 coin cell in an Ar filled high purity glove box. Linear sweep voltammetry was performed to evaluate the electrochemical stability of SS/GPE/Li cell using an electrochemical workstation. The tensile properties of nanofibers were measured using a UTM (Shimadzu, AG-X plus 100, Japan) based on the ASTM D882-12 standard. The charge-discharge behavior of Li/GPE/ $LiCoO_2$ coin cell was performed in a potential window of 2- 4.2 V at a C-rate of 0.1C using battery tester (Arbin instruments, BT 2000, USA).

2.5.1. Setups and methodology used for electrocatalytic water-splitting studies of ZMO nanofibers

The electrocatalytic behavior of ZMO nanofibers prepared at different calcination temperatures was studied using potentiostat/galvanostat (VersaSTAT 3, AMETEK scientific instruments, USA) with a three-electrode tubular glass set up (Fig. 2.2). The cell consists of a modified graphite electrode (effective surface area-1 cm^2) as working electrode (WE), platinum foil as a counter electrode (CE) and saturated calomel electrode (SCE) as a reference electrode (RE). The SCE was coupled through Luggin's capillary with Agar-KCl salt bridge to avoid the Ohmic polarization effect.

The electrodes to study the HER and OER were prepared by modifying the graphite rods. One end of the electrode was glassy polished and the other end was soldered with insulated copper wire. The sidewalls of the electrode were sealed with Teflon tape to avoid leakage of electrolyte. The polished end of the graphite electrode was then subjected to ultra-sonication in ethanol for 1 h and then air-dried. ZMO nanofiber suspension (10 mg.ml^{-1}) was prepared by dispersing the nanofibers in ethanol by ultra-sonication for an hour. 1ml of this suspension was pipetted on the polished surface of the graphite electrode and kept for drying. After drying, 10 µL of 0.5% PVDF (in DMF) solution was loaded on the ZMO nanofibrous layer to keep the deposit in position. The electrodes were prepared from ZMO nanofibers obtained at different

calcination temperatures 773, 873, and 973 K, respectively. In order to obtain equilibrium, the electrodes were immersed in a 1M KOH solution (N_2-saturated) for 30 min.
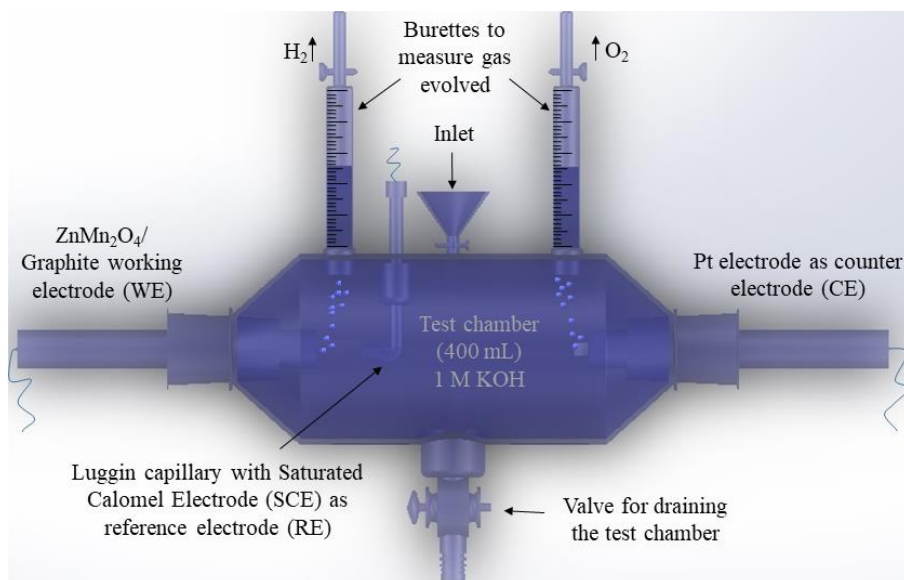
Fig. 2.2. Schematic representation of test set up used for electrochemical studies of ZMO nanofibers (drawn using Catia® software).

The electrocatalytic behavior of ZMO nanofibers obtained at different calcination temperatures was evaluated using CP, CV, and LSV techniques in an alkaline medium (1M KOH) at room temperature. The electrocatalytic test set up has the facility to collect the liberated H_2 and O_2 gases during electrolysis. The amount of gas liberated at a particular time can be correlated to the characteristic features of ZMO nanofibers obtained at different calcination temperatures.

2.5.2. Setups and methodology used for piezoelectric performance evaluation of PCAL nanofibers

The piezoelectric response of PCAL nanofiber was studied using an in-house developed experimental setup. The piezoelectric response was studied using two modes, namely, hand slapping mode and frequency-dependent mechanical vibration mode. In hand slapping mode, the PCAL nanofiber mat (4.6 cm^2 area) was sandwiched between two interdigitated copper electrodes, which were covered by an insulating film, as shown in Fig. 2.3. The PCAL nanogenerator was imparted repeatedly by hand

slapping to investigate the piezoelectric performance, and the output voltage was measured by an oscilloscope.
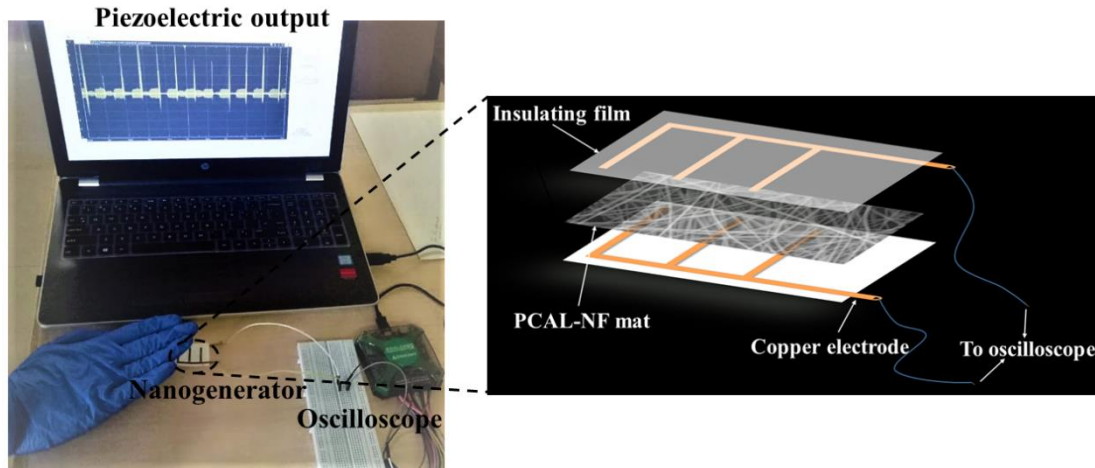
Fig. 2.3. Schematic representation of the setup used for piezoelectric performance of PCAL nanofibers by hand slapping mode.
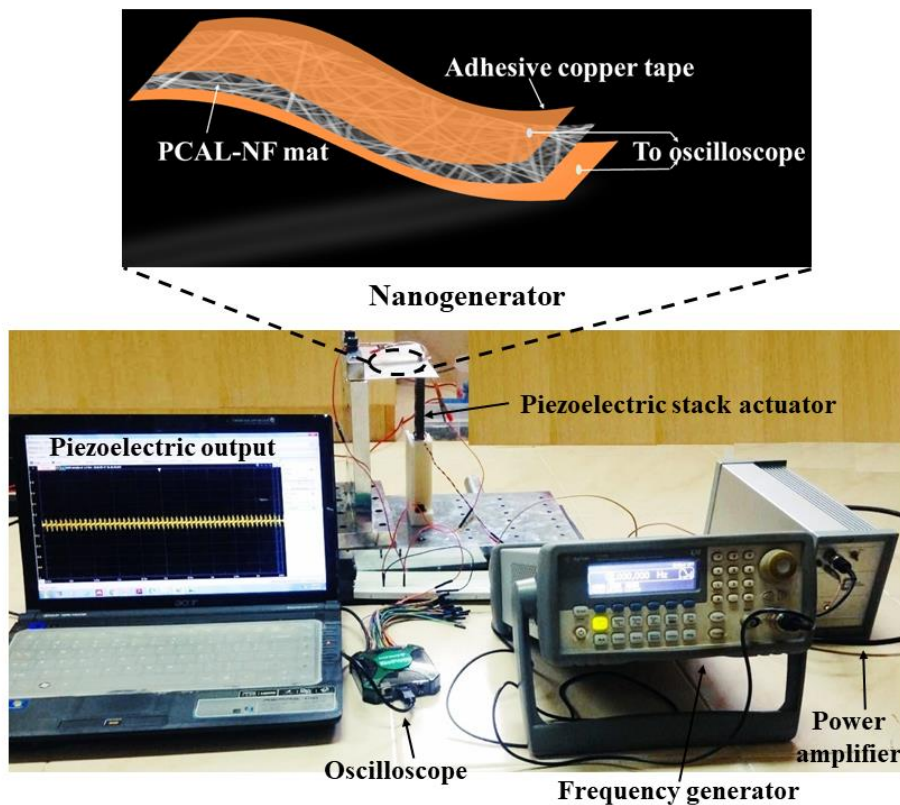
Fig. 2.4. Schematic representation of the setup used for piezoelectric performance of PCAL nanofibers by mechanical vibration mode.

The piezoelectric set up used for frequency-dependent mechanical vibration mode is shown in Fig. 2.4. The PCAL nanogenerator was excited by a piezo stack actuator system using the amplified sinusoidal signal generated from the signal generator (3 V_{PP}, frequency ranges between 10 and 150 Hz). The piezo stack actuator was placed between the base and the sample handle. The nanogenerator consists of a PCAL nanofiber mat (9.6 cm^2 area) sandwiched between adhesive copper tapes. The output voltage generated was measured by using an oscilloscope attached to the nanogenerator.

2.5.3. CR2032 coin cell assembly fabrication for Li/GPE/LiCoO₂
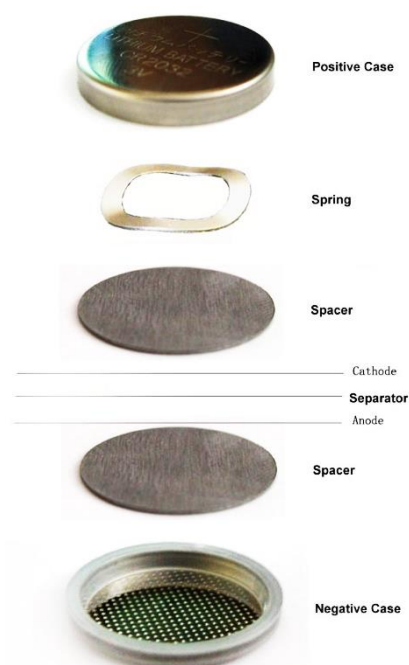
Fig. 2.5. Schematic representation of the CR2032 coin cell assembly (Kalluri 2016).

In order to study the cycle performance, CR2032 coin cell (20 mm diameter and 3.2 mm thickness) was used with $LiCoO_2$ as cathode and Li metal as reference and counter electrode. The coin cell fabrication was carried out in a glove box and the schematic representation of the coin cell assembly is shown in Fig. 2.5. The coin cell assembly was made using the following components; coin cell casings (cathode and anode), stainless steel spacers, stainless steel springs, precut discs of anode, cathode, and separator. Prior to cell fabrication, the separator membrane was punched to a disc of 15 mm diameter using a compact precision disc cutter. Firstly, the stainless steel spacer

was placed inside the negative case of the cell followed by an anode, separator (Celgard® 2400, PVDF, and PCAL) and cathode discs. The discs were saturated with liquid electrolyte (1M LiPF$_6$ in EC: DEC (1:1 v%)) while placing inside the case. Then, stainless spacer was placed above the cathode disc followed by spring. Lightly tap the components to seat them inside the anode casing properly. Finally, enclose everything with the cathode casing. The enclosed cell was then sealed by a crimper to finalize the coin cell assembly. Further, the charge-discharge behavior of this CR2032 coin cell was performed using battery tester.

PART - I

CHAPTER 3

CHAPTER 3

SOL-GEL ELECTROSPUN MESOPOROUS ZnMn$_2$O$_4$ NANOFIBERS WITH SUPERIOR SPECIFIC SURFACE AREA

This chapter discusses the fabrication of mesoporous spinel ZMO nanofibers by sol-gel assisted electrospinning combined with calcination, using poly(styrene-co-acrylonitrile) as the sacrificial polymeric binder. The structural, morphological and optical properties of these ceramic nanofibers were characterized. X-ray diffraction and X-ray photoelectron spectroscopy results revealed the presence of hexagonal ZnMnO$_3$ and MnO phases in the ZMO nanofibers produced. Based on these observations, we propose a plausible mechanism of formation of ZMO nanofibers. The nanofibers calcined at 773 K exhibit a specific surface area of 79.5 m^2.g^{-1}, which is higher than that of the zinc manganite nanofibers synthesized hitherto by sol-gel electrospinning. Moreover, this material exhibits four bandgaps, which is believed to be the first observation in ZMO nanofibers.

3.1. RESULTS AND DISCUSSION

3.1.1. Characterization of CNF mats

Fig. 3.1 shows the optical images of CNF mat before and after calcinations. Fig. 3.2 shows the SEM image of CNF mats and the corresponding fiber diameter histogram and the inset in Fig. 3.2 shows the image of the CNF mats at a higher magnification. Using ImageJ software fiber diameters of 50 fibers were measured at three different points of each fiber. Bead-free fibers of AFD ~281 nm were obtained by electrospinning.
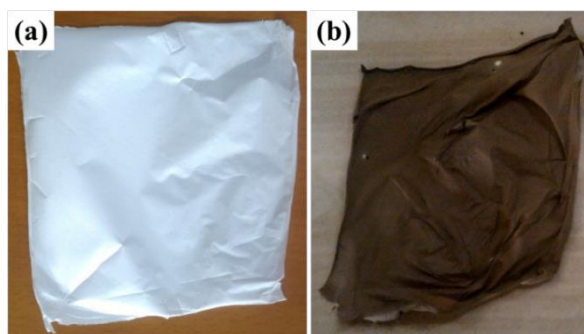
Fig. 3.1 Optical images of (a) precursor mat and (b) ZMO nanofiber mat.
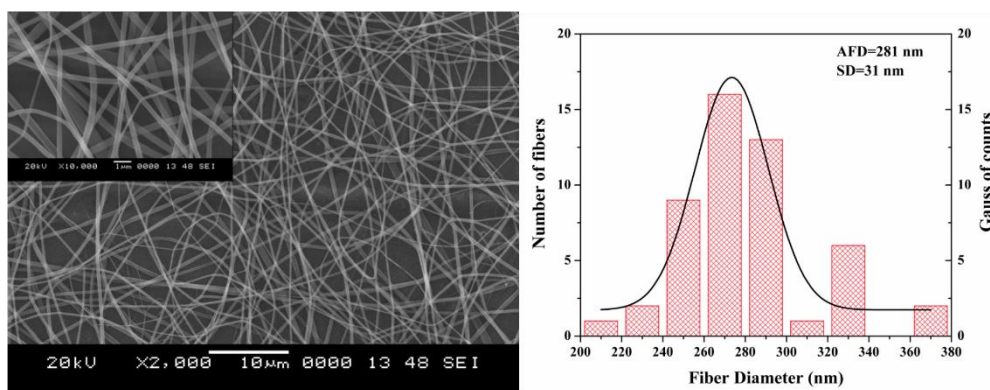
Fig. 3.2 SEM image of the CNF mats and the corresponding histogram depicting diameter distribution.

3.1.1.1. TGA Analysis
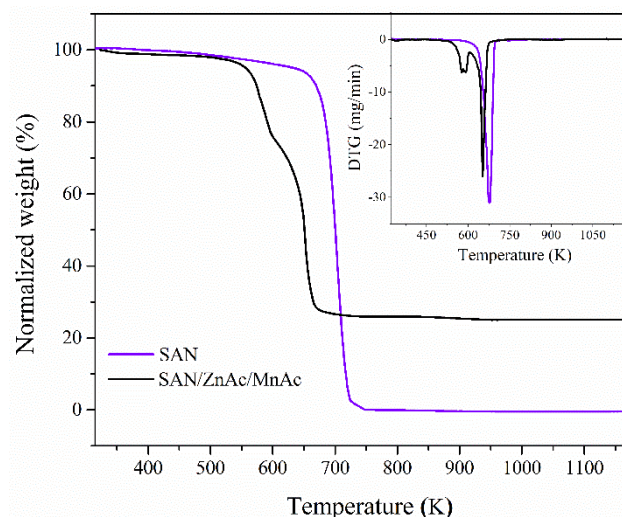
Fig. 3.3 TG plots (inset DTG plot) of SAN and CNF mats.

TGA analysis of the CNF mats was carried out to obtain the appropriate calcination temperature for the complete pyrolysis of SAN and conversion of metallic precursors to the corresponding oxides. Fig. 3.3 shows the TG and DTG curves of SAN and CNF mats. SAN exhibits single step degradation, whereas CNF displays a three-step degradation. 667 K is the onset of degradation for SAN and the degradation completed at 773 K. In the case of CNF mats, the decomposition starts from 558 K, which corresponds to the decomposition of the metallic precursors ZnAc and MnAc. The prominent decay observed at 639 K is attributed to the decomposition of SAN. This is due to the catalytic effect of the acetic acid liberated by the decomposition of metal

acetates on the degradation of SAN (George et al. 2015). There is no further weight change beyond 753 K indicating the completion of the thermal degradation reactions.

3.1.2. Characterization of ZMO nanofiber mats

3.1.2.1. SEM, FESEM and HRTEM results
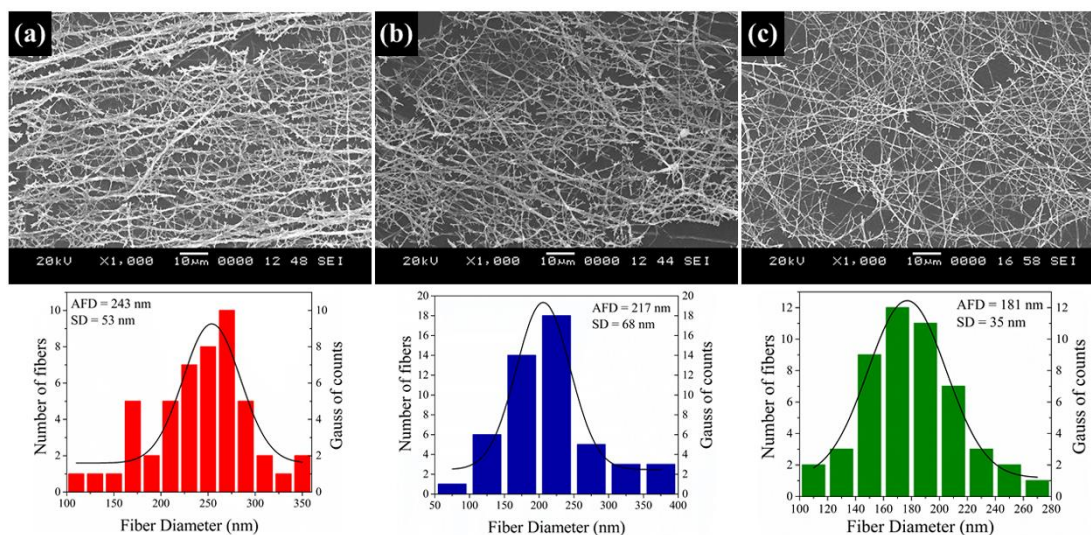
Fig. 3.4 SEM images of ZMO nanofibers obtained by calcination at (a) 773 K (b) 873 K and (c) 973 K.

Fig. 3.4 (a-c) shows the SEM images of ZMO nanofibers obtained by calcination of the CNF mats at 773, 873 and 973 K, respectively. The AFD of ceramic nanofibers are less than that of composite fibers. This can be attributed to the elimination of the organic phases. The AFD of the ceramic nanofibers decreased as a function of the calcination temperature, which can be attributed to the crystallite growth as well as densification. Fig. 3.5 (a-b) shows the FESEM images of ZMO nanofibers obtained at a calcination temperature of 773 K, at different magnifications. After calcination the fiber surface became rough, which is due to the formation of ZMO grains upon elimination of the organics.

Fig. 3.6 shows HRTEM images of single ZMO fibers obtained at different calcination temperatures (773, 873 and 973 K). Lattice fringes with d-spacing of 0.288, 0.247 and 0.153 nm were observed, which closely match with that of the (200), (211) and (224) planes of tetragonal spinel structured ZMO. SAED patterns confirm the formation of ZMO nanofibers and the diffraction patterns were indexed to the corresponding planes of spinel ZMO. The dot patterns confirm the polycrystalline

nature of ZMO nanofibers. Moreover, the SAED patterns reveal that the crystallinity of ZMO nanofibers got enhanced as a function of the calcination temperature.
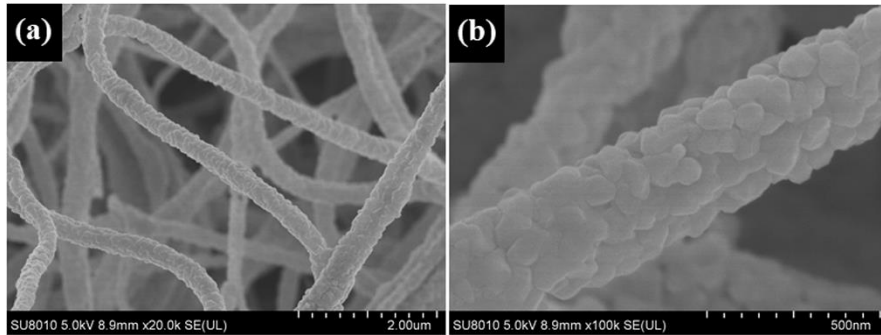
Fig. 3.5 (a) and (b) FESEM images of ZMO nanofibers obtained by calcination at 773 K.
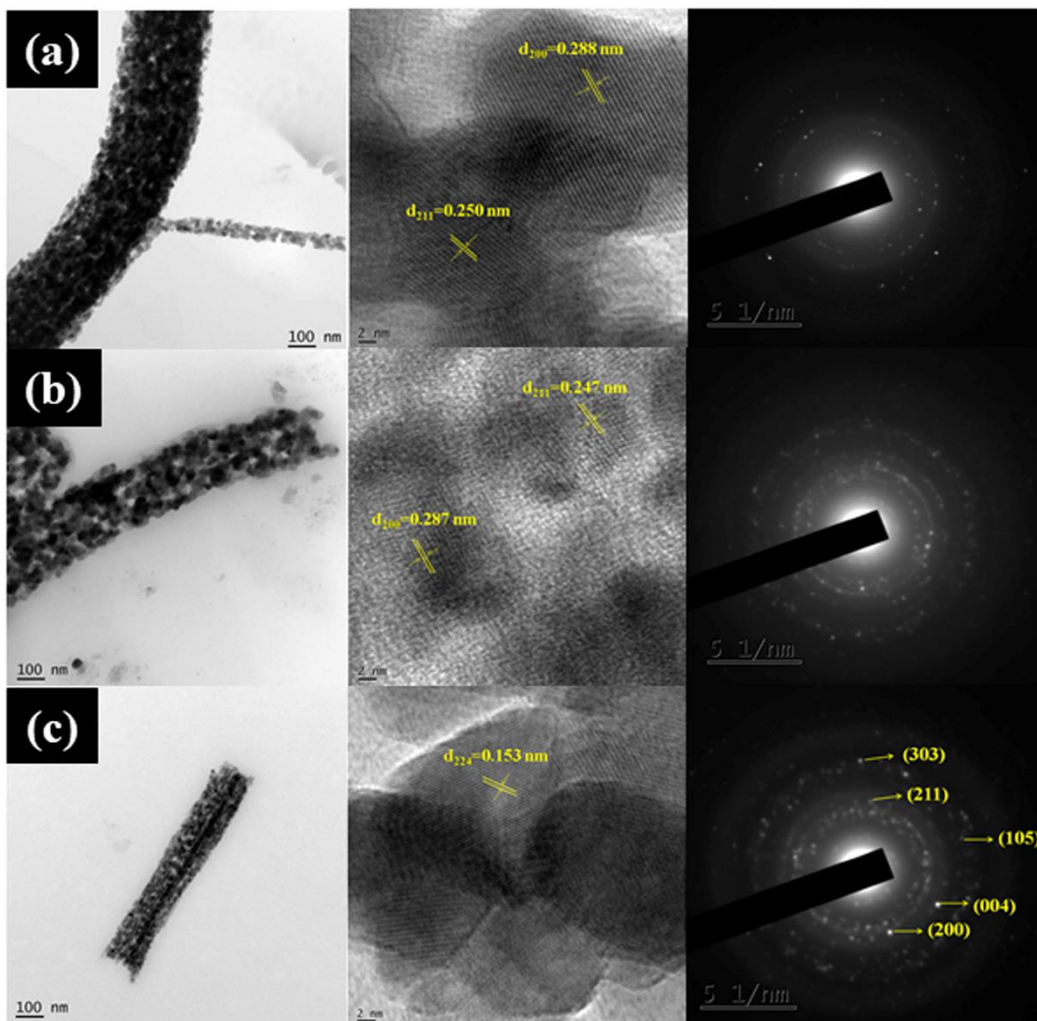
Fig. 3.6 HRTEM images together with SAED patterns of ZMO nanofibers obtained by calcination at (a) 773 K (b) 873 K and (c) 973 K.

3.1.2.2 FTIR spectroscopy results

Fig. 3.7 shows the FTIR spectra of the CNF mats and ZMO nanofiber mats. A broad peak at 3418 cm^{-1} in the spectrum of the CNF corresponds to the O-H stretching of physisorbed water. The peaks at 3030, 2927 and 2237 cm^{-1} correspond to C–H stretching in styrene aromatic ring, CH$_2$ asymmetric stretching and stretching C≡N group, respectively. The peaks at 1574 and 1423 cm^{-1} represent the C=O bending and C-H deformation, respectively of the acetate. The peaks 763 and 693 cm^{-1} correspond to out of plane deformation of C-H group in styrene ring (Mistry 1991). After calcination, the peaks corresponding to the organic groups of the composite fibers disappeared. The new peaks at 526 and 647 cm^{-1} indicate the presence of metal-oxygen vibrations i.e. Zn-O and Mn-O bonds of spinel ZMO (Lobo and Kumar 2016). Upon increasing the calcination temperature these two peaks became more intense, which could be due to enhanced crystallinity of the nanofibers.
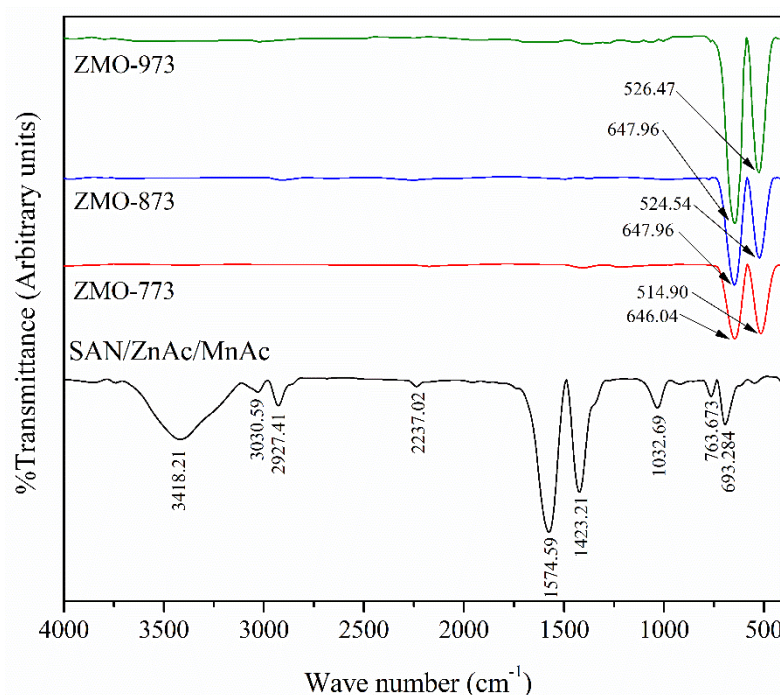
Fig. 3.7 FTIR spectra of CNF mats and ZMO nanofiber mats obtained at various temperatures (ZMO-773, ZMO-873 and ZMO-973).

3.1.2.3. XRD Results

Fig. 3.8 shows the X-ray diffraction patterns of ZMO nanofibers obtained at different calcination temperatures, and that of standard ICDD 24-1133 line diffraction pattern of

ZMO along with the crystal structure of tetragonal spinel ZMO. The diffraction peaks correspond to the standard ICDD card no. 24-1133 with $I4_1/amd$ space group. The ZMO nanofibers are crystalline in nature and the sharp peaks in the XRD patterns indicate the complete elimination of the organic phases. As the calcination temperature increases the intensity of the peaks also increased, which is due to the temperature-induced crystallite growth. Presence of a minor shoulder was observed in the peak of the (211) plane, which probably indicates the crystallization of a secondary phase. From the deconvoluted peak (see the appendix, Fig. I.2) it is inferred that this peak may well be due to the crystallization of $ZnMnO_3$ phase (indexed using ICDD card no. 28-1468 line diffraction pattern of hexagonal $ZnMnO_3$) upon increasing the calcination temperature. The $ZnMnO_3$ phase peak is initially broad, indicating less crystallinity; the intensity of this peak decreases with increase in temperature during ZMO formation. This observation is in line with the past observations on the phase evolution of $ZnMnO_3$ in the Zn–Mn–O system in the temperature range of 400–800 °C, even at low manganese additions (Peiteado et al. 2007).
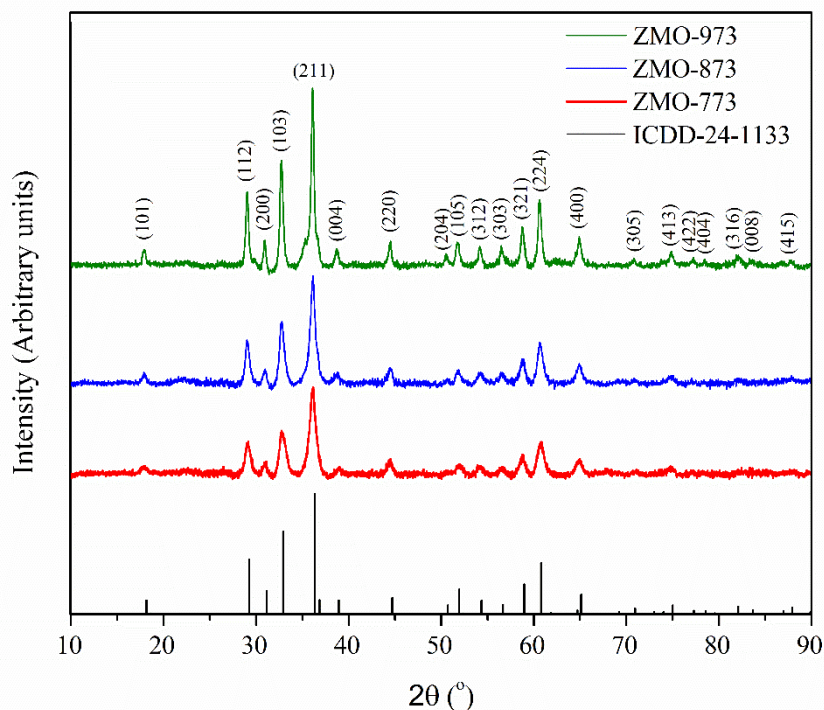
Fig. 3.8 (a) XRD patterns of ZMO nanofibers obtained at different calcination temperatures (ZMO-773, ZMO-873 and ZMO-973).

Using the following expression the lattice parameters of the ZMO nanofibers were calculated:

$$\frac{1}{d^2} = \frac{h^2+k^2}{a^2} + \frac{l^2}{c^2} \tag{3.1}$$

The average crystallite size (D) of ZMO nanofibers was calculated using Scherrer formula:

$$D = \frac{K\lambda}{\beta cos\theta} \tag{3.2}$$

Where K is a constant, whose value is 0.9, λ is the wavelength of CuKα radiation (1.5418 Å), β indicates full width at half maximum (FWHM) of the peak in radians and θ is the diffraction angle.

Crystallite sizes of the ZMO nanofibers calculated using Williamson-Hall (W-H) method were compared with that calculated by Scherrer's equation. W-H method uses the following equation:

$$\beta_{hkl}cos\theta = \frac{k\lambda}{D} + 4\varepsilon sin\theta \tag{3.3}$$

Fig. 3.9 (a-c) shows the linear plots of $\beta_{hkl}cos\theta$ against $4sin\theta$ for the ZMO nanofibers calcined at 773, 873 and 973 K, respectively. The lattice strain (ε) and crystallite size were obtained from the slope and y-intercepts of the linear fits and their values are shown in Table 3.1-3.3 along with those obtained using Scherrer formula.

From these results, it can be seen that the crystallite size increases with the calcination temperature. This is because as the temperature increases the atoms or ions diffuse around the interatomic distance to more stable positions. During this process, one crystallite grows at the expense of another (Park and Kim 2009). It is noticed that with the increase in calcination temperature from 773 to 973 K the lattice strain decreases with a gradual increase in crystallite size, which is in line with previous reports (Parra and Haque 2014).

Table 3.1 Lattice parameters of ZMO-773.

(hkl)	Position (2θ°)	d-spacing (Å)	FWHM (2θ°)	a (Å)	c (Å)	D (nm)		ε (W-H)
						(W-H)	(D-S)	
101	17.82	4.9734	0.23709					
112	29.08	3.0682	0.66669					
200	30.9	2.8915	0.57202					
103	32.76	2.7315	0.8184					
211	36.18	2.4807	0.77851	5.7375	9.2396	13.28	10.74	0.0012
004	38.96	2.3099	0.53815					
220	44.5	2.0343	0.75048					
321	58.8	1.5691	0.75752					
224	60.78	1.5227	0.83533					
400	64.98	1.4340	0.80134					

Table 3.2 Lattice parameters of ZMO-873.

(hkl)	Position (2θ°)	d-spacing (Å)	FWHM (2θ°)	a (Å)	c (Å)	D (nm)		ε (W-H)
						(W-H)	(D-S)	
101	17.88	4.9569	0.32075	5.7594	9.2762	17.78	13.54	0.0010
112	29.02	3.0744	0.50146					
200	30.94	2.8879	0.39808					
103	32.74	2.7331	0.63489					
211	36.12	2.4847	0.61776					
004	38.8	2.3191	0.14937					
220	44.44	2.0369	0.46099					
321	58.78	1.5696	0.34341					
224	60.64	1.5259	0.63076					
400	64.92	1.4352	0.48232					

Table 3.3 Lattice parameters of ZMO-973.

(hkl)	Position (2θ°)	d-spacing (Å)	FWHM (2θ°)	a (Å)	c (Å)	D (nm)		ε (W-H)
						(W-H)	(D-S)	
101	17.88	4.9569	0.38864	5.7544	9.2946	25.92	22.92	0.0006
112	29.04	3.0724	0.34283					
200	30.94	2.8879	0.33493					
103	32.72	2.7347	0.39177					
211	36.10	2.4861	0.36483					
004	38.72	2.3237	0.38498					
220	44.56	2.0317	0.23255					
321	58.8	1.5691	0.4135					
224	60.64	1.5123	0.43065					
400	64.92	1.4352	0.45163					
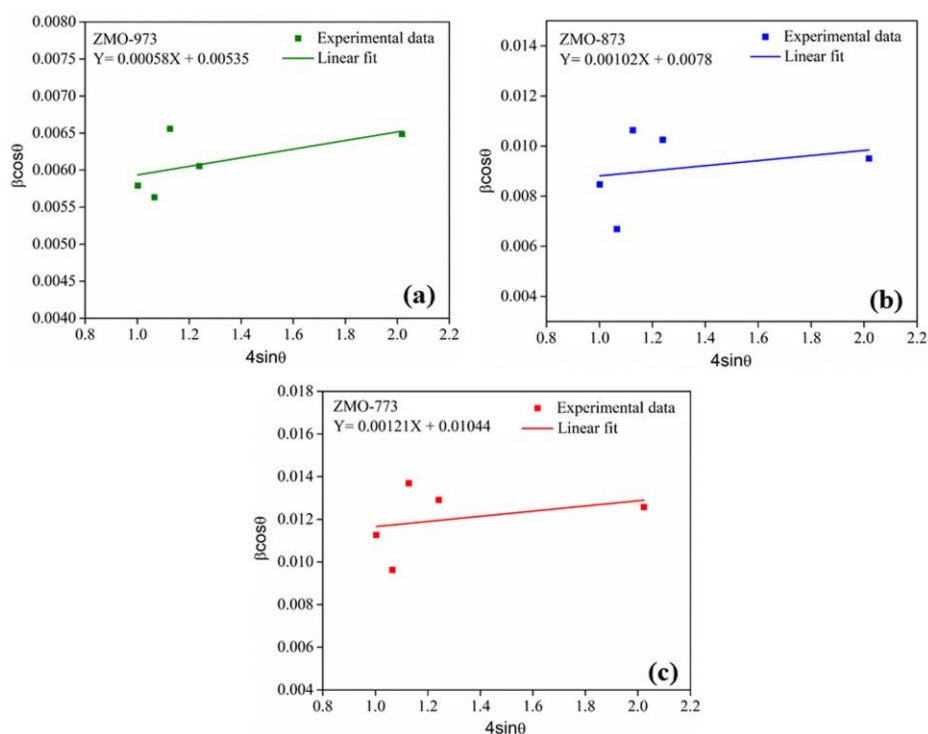
Fig. 3.9 (a-c) Williamson-Hall plots of ZMO nanofibers obtained at different calcination temperatures.

3.1.2.4. UV-vis NIR spectroscopy Results

UV-visible-NIR diffuse reflectance spectra of ZMO nanofibers are shown in Fig. 3.10. All the samples exhibit absorptions in the λ ranges of 260–350 nm and 700–850 nm. This may be due to the charge transfer between lattice oxygen and cations. The bandgap energies (E_g) of these nanofibers were obtained using the following equation:

$$(\alpha h\upsilon)^n = B(h\upsilon - E_g) \tag{3.4}$$

where, α is the optical absorption coefficient, $h\upsilon$ is the photon energy, B is a constant, E_g is the bandgap and n is an index which depends on the type of electronic transition. For a direct transition n is 2, and n for an indirect transition is ½. Here, n is taken as 2 since ZMO allows direct transition. The bandgap energy was calculated from the linear intercept of $(\alpha h\upsilon)^2$ vs. $h\upsilon$ plot (i.e. Tauc plot) (Tauc 1970) and is shown in Fig. 3.10.

It was observed that ZMO exhibits more than one bandgap and the corresponding band gap values are shown in Table 3.4. The band gap energies

corresponding to *Eg1* are in good agreement with that reported previously for ZMO (Zhang et al. 2011). The band gap energy values *Eg2* and *Eg4* decreased with increase in calcination temperature. The narrowing of these band gap energies can be attributed to the increase in crystallite size with calcination temperature, which is in line with the XRD results (see section 3.2.3.). Joseph et al. (2011) reported a band gap value of 3.42 eV for substitutionally-doped Mn at Zn^{2+} site of ZnO. This suggests that the band gap energies *Eg2* and *Eg4* may be due to $ZnMnO_3$ secondary phase. The band gap *Eg3* may be due to MnO phase. Also, it was observed that *Eg3* increased with increase in temperature suggesting a decrease in the amount of MnO. This is in good agreement with the XRD results that amorphous MnO is being used for the formation of ZMO (discussed in section 3.1.2.8.).
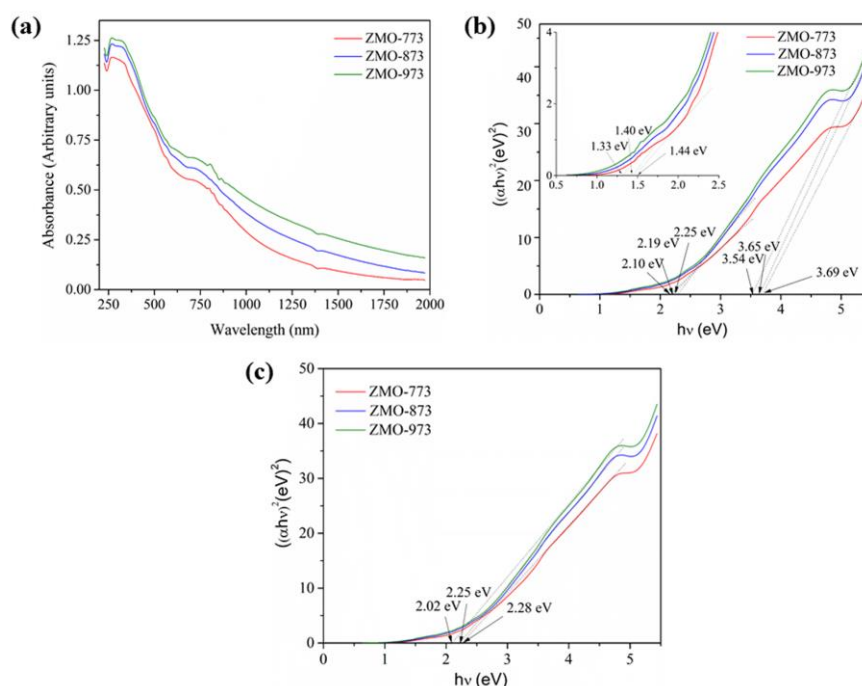
Fig. 3.10 UV-vis-NIR diffuse reflectance spectra of ZMO nanofibers calcined at different temperatures.

3.1.2.5. Raman Spectroscopy

Raman spectra of ZMO nanofibers acquired at 25°C in the wavenumber range of 100–1000 cm^{-1} are shown in Fig. 3.11. In this study three Raman modes were observed at 660.16, 310.3 and 349.6 cm^{-1} which can be assigned to the A_{1g}, T_{2g} and E_g modes of

spinel ZMO (Samanta et al. 2007). In spinel oxides, the modes above 600 cm^{-1} (i.e. A$_{1g}$ mode) correspond to the symmetric breathing mode of AO$_4$ (ZnO$_4$) tetrahedron, where motion of only oxygen atoms takes place. The lowest frequency mode ~310 cm^{-1} (T$_{2g}$) is the characteristic peak corresponding to the BO$_6$ (MnO$_6$) octahedron. The E$_g$ mode is due to the symmetric bending motion of oxygen atoms within the AO$_4$ (ZnO$_4$) unit (Zhang et al. 2015). Also, a slight shift in peaks towards higher wavenumbers was observed as the calcination temperature was increased. This may be due to the difference in crystallite size and the phonon confinement associated with it (Arora et al. 2007).
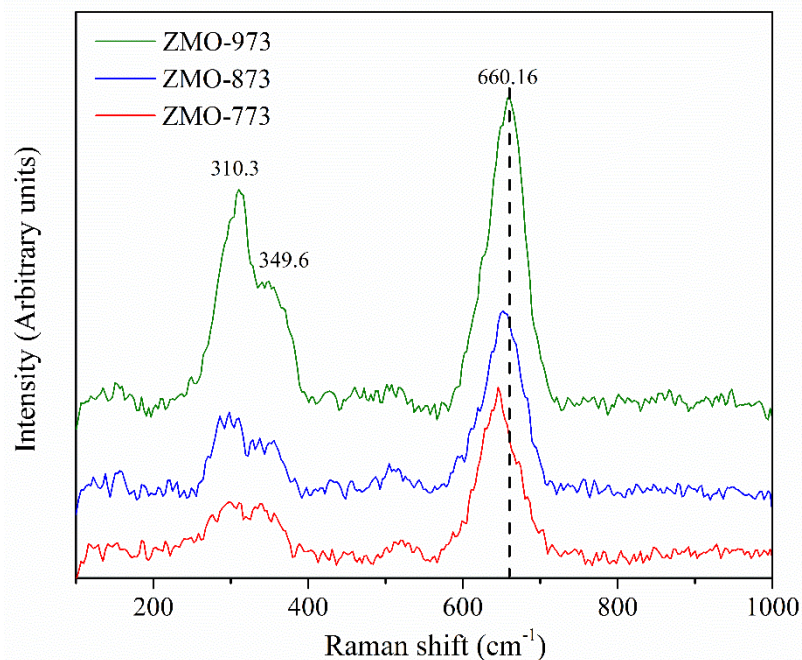
Fig. 3.11 Raman spectra of ZMO nanofibers calcined at different temperatures.

Table 3.4 Band gap energies of ZMO nanofibers calcined at 773, 873 and 973 K.

Calcination temperature	Band gap energy (eV)			
(K)	*Eg1*	*Eg2*	*Eg3*	*Eg4*
773	1.44	3.69	2.10	2.28
873	1.40	3.65	2.19	2.25
973	1.33	3.54	2.25	2.02

3.1.2.6. XPS Study
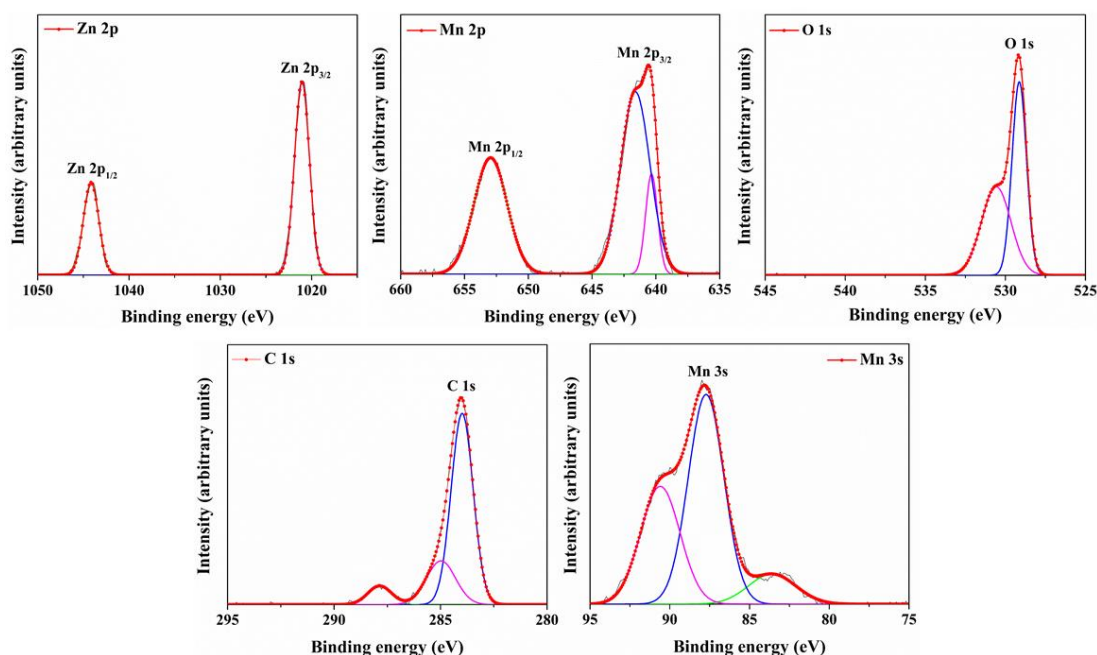
Fig. 3.12 High resolution XPS spectra of ZMO nanofibers obtained by calcination at 773 K.

XPS was performed for the ZMO nanofibers to examine the chemical states of Zn, Mn and O. The high resolution spectra of Zn 2p, Mn 2p, O 1s, C 1s and Mn 3s are shown in Fig. 3.12 and Table 3.5. The Zn 2p spectrum contains two peaks at ~1044 eV and ~1021 eV, which can be attributed to Zn $2p_{1/2}$ and Zn $2p_{3/2}$, respectively. The energy difference between the two lines is 23.1 eV which is in agreement with the standard value for ZnO that can be assigned to the Zn–O bond in ZMO crystal (Moulder 1992). This reveals that the oxidation state of Zn is +2 and Mn is +3 in the ZMO phase.

The peaks at ~640 eV and ~650 eV correspond to Mn $2p_{1/2}$ and Mn $2p_{3/2}$, respectively. The deconvolution of Mn $2p_{3/2}$ peak shows a doublet at ~640 eV and ~641 eV indicating the +2 and +3 oxidation states of Mn ions (Tang et al. 2014). It can be seen from the Mn $2p_{3/2}$ peaks that Mn^{3+} predominates, which is in agreement with the XPS peaks of Zn 2p. The binding energies of Mn $2p_{1/2}$ and Mn $2p_{3/2}$ are summarized in Table 3.5. In the deconvoluted O 1s spectrum, the main peak located at ~529 eV corresponds to lattice O^{2-} anions bound to the metal cations. The second peak located at ~530.57, 531.16 and 531.09 eV can be attributed to adsorbed oxygen molecules on the surfaces of the nanofibers. Deconvoluted C 1s spectrum shows three binding

energies at ~284, 285 and 288 eV corresponding to sp^2 and sp^3 hybridized carbon and C–O functional group (Abouali et al. 2015). Mn 3s spectrum shows multiplet splitting, which is due to the coupling of non-ionized 3s electron with 3d valence band electrons (Meng et al. 2014).

3.1.2.7. Surface area and Porosity Measurements

The nitrogen adsorption-desorption isotherms and the corresponding BJH pore size distribution curve of ZMO nanofibers are shown in Fig. 3.13 and Fig. I.4 (see the Appendix). The nitrogen adsorption-desorption isotherms exhibit the characteristic features of type IV isotherm according to International Union of Pure and Applied Chemistry (IUPAC) classification, which indicates the mesoporous nature of ZMO nanofibers (Sing 2009). The main reason for the mesoporous structure of ZMO nanofibers is the elimination of polymeric binder SAN and the decomposition of metal acetates during calcinations. Due to the high temperature stability of SAN, the organic volatiles are removed gradually creating sufficient mesopores in between the fibers during the degradation process. The values of pore volume and specific surface area of ZMO nanofibers calcined at different calcination temperatures are presented in Table 6. The highest specific surface area value 79.51 m^2.g^{-1} was obtained for the nanofibers calcined at 773 K. It is noteworthy that the specific surface area of the ZMO nanofibers synthesized in this study is higher than that reported elsewhere till date by other researchers (Yang et al. 2014). It was observed that the specific surface area decreases with increase in calcination temperature, which is in line with the average crystallite sizes obtained from XRD. As the calcination temperature increases the average crystallite size increases. So, the number of grains per unit mass decreases, leading to a reduction in the specific surface area. An increase in the calcination temperature enhances crystallite growth and further densification of these fibers, which subsequently results in reduced porosity and specific surface area. The superior surface area suggests that these ZMO nanofiber mats could be a promising electrode material for lithium ion batteries. This is due to their high contact area with the electrolyte that would lead to high lithium-ion flux across the electrode/electrolyte interface (Goriparti et al. 2014).

Table 3.5. XPS results of ZMO nanofibers calcined at different temperatures

Sample Name	Zn 2p BE (eV)		Mn 2p BE (eV)			O 1s BE (eV)		C 1s BE (eV)			Mn 3s BE (eV)		
	$2p_{3/2}$	$2p_{1/2}$	$2p_{3/2}$		$2p_{1/2}$								
ZMO-773	1021.05	1044.15	640.34	641.62	652.95	529.13	530.57	283.97	284.98	287.86	83.58	87.72	90.59
ZMO-873	1021.13	1044.24	640.69	641.96	653.19	529.48	531.16	284.32	285.76	288.21	83.86	87.84	90.71
ZMO-973	1021.13	1044.23	640.65	641.93	653.17	529.44	531.09	284.21	285.56	288.21	83.71	87.90	90.75

Table 3.6. Surface area and porosity parameters of ZMO nanofibers calcined at 773, 873 and 973 K.

Calcination temperature (K)	Specific surface area (m^2/g)	Total pore volume (cc/g)	Average pore diameter (nm)	Mesopore volume (BJH method) (cc/g)
773	79.5	0.1769	8.9	0.1531
873	53.8	0.1433	10.6	0.1257
973	37.8	0.0522	5.5	0.0345
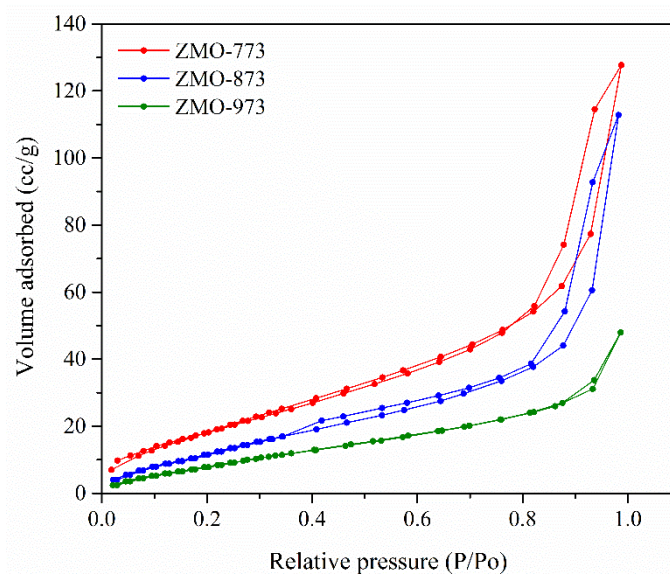
Fig. 3.13 Nitrogen adsorption–desorption isotherms of ZMO nanofibers obtained at different calcination temperatures.

3.1.2.8. Proposed mechanism of tetragonal spinel ZMO nanofibers formation

The presence of tetragonal spinel structure of ZMO nanofibers as well as the phase evolution of hexagonal $ZnMnO_3$ was confirmed by the XRD results. However, there was no +4 oxidation state of Mn observed in the XPS results. This may due to the ability of manganese oxides (MnO_x) to undergo *carbothermal reduction* to MnO in the presence of carbon and carbon monoxide, the byproducts of degradation of the organic moieties (see equations 3.5 a-f) (Alonso et al. 2013; Kumar et al. 2017; Li et al. 2012). Even though there is no evidence for the formation of MnO from XRD results, the +2 oxidation state of Mn obtained from XPS study confirmed the presence of MnO. Also, the band gap energies obtained from the UV-vis-NIR results confirmed the presence of MnO. Further, the formation of $ZnMnO_3$ may be presumed to be due to substitutional doping of ZnO (Zn in +2 oxidation state) and MnO (Mn in +2 oxidation state) (Jiang et al. 2011; Jing et al. 2010; Joseph and Venkateswaran 2011). This could be the probable reason for absence of +4 oxidation state of Mn in the XPS peaks of Mn. However, XRD confirms the formation of crystalline $ZnMnO_3$ and this phase may be defective due to the presence of Mn^{2+}, whose band gap energies were seen to vary with calcination temperature (Sambandam et al. 2015).

$$MnCO_3 \rightarrow MnO + CO_2 \tag{3.5a}$$

$$Mn_3O_4 + CO \rightarrow 3MnO + CO_2 \tag{3.5b}$$

$$Mn_2O_3 + CO \rightarrow 2MnO + CO_2 \tag{3.5c}$$

$$MnO_2 + CO \rightarrow MnO + CO_2 \tag{3.5d}$$

$$2ZnO + 2MnO + O_2 \rightarrow 2ZnMnO_3 \tag{3.5e}$$

$$ZnMnO_3 + MnO \rightarrow ZnMn_2O_4 \tag{3.5f}$$

The rapid decomposition of zinc acetate compared with manganese acetate, and the formation of MnO might possibly be the reason for the formation of defective $ZnMnO_3$. Further decomposition of manganese acetate gives rise to more MnO phase, which will solutionize with $ZnMnO_3$ to form tetragonal ZMO. This tetragonal form of spinel structure is also called the low temperature spinel ZMO that forms below 1373K, with a low concentration of Mn atoms (Driessens and Rieck 1966; Nádherný et al. 2015). The schematic of the formation of mesoporous ZMO nanofibers from CNF is shown in Fig. 3.14.
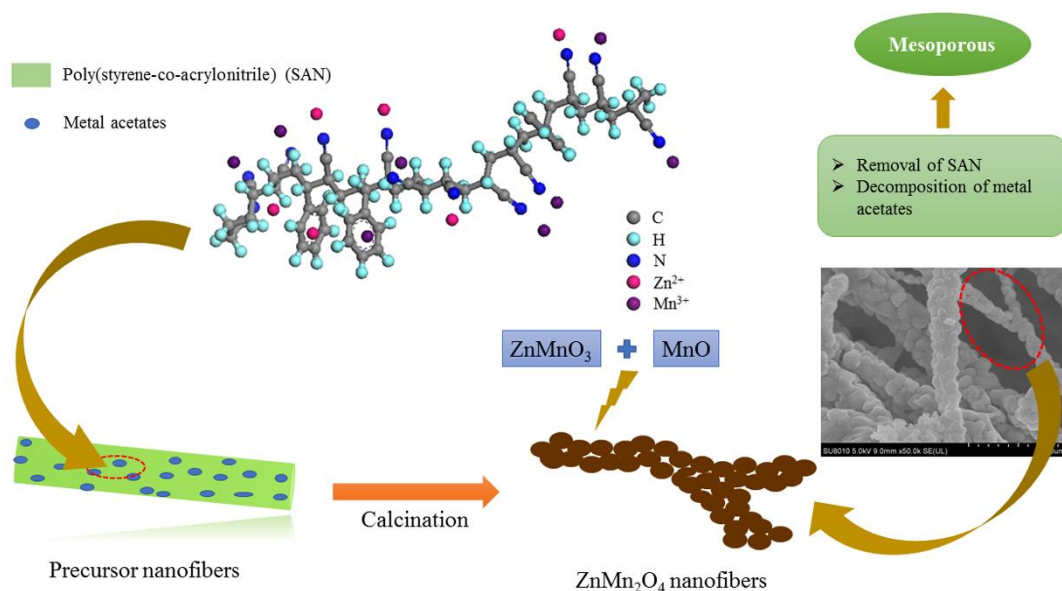
Fig. 3.14 Schematic showing the formation of mesoporous spinel ZMO nanofibers.

3.2. SUMMARY AND CONCLUSIONS

Herein, mesoporous spinel ZMO nanofibers were synthesized by sol-gel assisted electrospinning technique combined with calcinations. Due supposedly to the improved

59

thermal stability and unique thermal degradation behavior of the binder, poly(styrene-*co*-acrylonitrile), ZMO nanofibers with improved morphological features were obtained. The presence of cubic $ZnMnO_3$ phase was observed in ZMO nanofibers. Based on the results obtained from XRD, XPS and UV-Vis NIR spectra it can be concluded that the combination of $ZnMnO_3$ with MnO could have led to the formation of ZMO nanofibers. The superior specific surface area 79.51 m^2g^{-1} was obtained for the fibers calcined at 773 K and the surface area values of these ceramic nanofibers decrease when the calcination temperature was increased. The superior surface area suggests the ZMO nanofibers could be a better electrode material for lithium ion batteries.

CHAPTER 4

CHAPTER 4

ZnMn₂O₄ NANOFIBERS AS BIFUNCTIONAL ELECTROCATALYSTS FOR HYDROGEN AND OXYGEN EVOLUTION REACTIONS

Herein, we report the electrocatalytic behavior of ZMO nanofibers by sol-gel assisted electrospinning technique using SAN as the polymeric binder. SAN plays an essential role in the morphological transformation of composite fibers into ceramic fibers. The interaction of nitrile and carbonyl group present in SAN and zinc acetate ensures uniform dispersion of polymer metal salt solutions. The electrocatalytic behavior of ZMO nanofibers in alkaline media has not been reported so far. The electrocatalytic studies were carried out in both HER and OER in alkaline media. The presence of open space and high surface area in 1-D nanostructures empowers quick mass transport and accessibility of electrolyte atoms into the profound part of the electrode-catalyst interface.

4.1. RESULTS AND DISCUSSION

4.1.1. XRD analysis

The crystalline phases of ZMO nanofibers at different calcination temperatures were studied using XRD patterns. Fig. 3.8 showed the XRD patterns of ZMO nanofibers obtained by calcination at three different temperatures (ZMO-773, ZMO-873, and ZMO-973) along with the standard ICDD 00-024-1133 diffraction pattern corresponding to the tetragonal spinel ZMO. The peak corresponding to (2 1 1) plane is sharp at higher calcination temperature, which indicates the well-defined crystallinity of the sample. The minor shoulder peak at (2 1 1) plane indicates the presence of hexagonal $ZnMn_2O_3$ phase (ICDD database 00-028-1468). The intensity of this shoulder peak decreases with high calcination temperature during the formation of ZMO. The formation mechanism of ZMO nanofibers was reported in our previous study (Shamitha et al. 2017). The XRD pattern corresponding to SAN/ZnAc/MnAc precursor nanofibers is shown in Fig. I.1. The amorphous nature of precursor nanofibers is due to the presence of SAN. Traces of ZnAc and MnAc were also confirmed from

the XRD pattern. No traces of impurities and other crystalline phases were observed in XRD pattern of ZMO nanofibers, indicating the complete elimination of organic moieties from SAN after calcination process. The average crystallite size of ZMO nanofibers was calculated using the *Scherrer* equation, and the obtained values were listed in the Table 4.1. An increase in crystallite size with calcination temperature was observed, which can be attributed to the temperature driven crystallite growth, as the temperature increases the crystallites grow at the expense of the other ones.

4.1.2. SEM and FESEM results

SEM images of the precursor nanofibers and ZMO nanofibers obtained at different temperatures are shown in Fig. 3.2. When the calcination temperature was increased from 773 to 973 K the crystallite size got increased. This can be attributed to the temperature induced crystallite growth. Similar to Ostwald ripening in an aqueous medium in the case of nanofibers, the larger crystallites grow at the expense of the smaller ones. The average fiber diameters of ZMO nanofibers were calculated from SEM micrographs and the values were presented in Table 4.1. The AFD of ZMO nanofibers decreased compared to that of composite nanofibers, which is due to the elimination of organic phases during calcination. FESEM images of ZMO nanofibers at different calcination temperatures are shown in Fig. 3.5 (a-b). After calcination, the surface morphology of nanofibers became rough compared to that of the precursor nanofibers. This is mainly due to the removal of organic fragments and the formation of ZMO crystallites.

4.1.3. BET analysis

The specific surface area of ZMO nanofibers was measured by BET method, and the obtained values are listed in the Table 4.1. ZMO-773 exhibited highest specific surface area of 79.5 $m^2.g^{-1}$. As the calcination temperature increases the surface area decreases. An increase in crystallite size with calcination temperature was observed from XRD results. Consequently, the number of crystallites per unit mass gets diminished, which will further prompt a decrease in specific surface area.

Table 4.1 Crystallite size and specific surface area values of ZMO nanofibers obtained at different calcination temperatures.

Calcination temperature (K)	Average fiber diameter (nm)	Crystallite size (nm)	Specific surface area ($m^2.g^{-1}$)
773	243±53	10.74	79.5
873	217±68	13.54	53.8
973	181±35	22.92	37.8

4.1.4. Hydrogen evolution reaction

HER is the most effectively studied mechanism in electrochemistry due to its ease in producing gaseous hydrogen. In this reaction the H^+ ions from the electrolyte combine with the electrons at the cathode surface to form adsorbed H atoms, which later evolve as H_2 gas. The electrocatalytic HER of ZMO nanofiber-modified graphite electrode (ZMO/GE) in KOH medium was studied by CP, CV, LSV techniques and Tafel slope measurements. CV is a well-established technique to study the kinetics of electron transfer reactions and thermodynamics of redox reactions associated with the system. In CP technique, a constant current is applied between the counter and working electrode and the potential at the WE is examined with respect to time at the reference electrode. The purpose of this current controlled technique is that the electron transfer reactions take place at the active site of the WE to maintain the applied current.

Fig. 4.1 (a) shows the CV curves obtained for HER of ZMO nanofibers at different calcination temperatures. The studies were carried out at a potential window of 0 to -1.6 V at a scan rate of 100 $mV.s^{-1}$ for 50 cycles under 1 M KOH. During initial cycles, it was observed that the cathodic peak current at -1.6 V decreased eventually with successive cycles and became constant. This variation in current during the initial cycles of CV can be ascribed to the resistance offered by the hydrogen bubbles at the electrocatalyst surface (ZMO/GE) (Nagai et al. 2003). The peak current showed stable value after reaching an equilibrium state in H_2 formation and separation from the electrode surface. The values of cathodic peak current and the onset potential for HER

obtained from CV curves were listed in Table 4.2. It was observed that ZMO-773 exhibited the highest cathodic peak current and least onset potential for HER. Interestingly, the onset potentials of ZMO nanofibers are less than that of commercial Pt/C/GE (-0.935 V) shown in Fig. I.5, which will be beneficial for HER performance. Along with this, the highest electrocatalytic activity of ZMO-773 towards HER can be attributed to the high specific surface area and the unique morphological features associated with them. High surface area may favor the carrier adsorption at the active site of the catalyst and enhance the water-splitting performance (Sachin Kumar et al. 2019). Further to evaluate the HER, LSV studies were carried out at a negative potential range of 0 to -1.6 V followed by a scan rate of 100 mV.s^{-1}. The LSV curves correspond to HER of ZMO nanofibers are shown in Fig. 4.2 (a). ZMO-773 exhibited maximum electrocatalytic performance towards HER with high cathodic peak current and least onset potential which are in agreement with the CV results.

Fig. 4.1 (a-b) CV curves and CP stability response for HER of ZMO nanofibers at different calcination temperatures and (c) respective evolution of H$_2$ after 300 s.

Table 4.2 HER parameters for ZMO nanofibers at different calcination temperatures.

T (K)	Cathodic peak current at -1.6 V (mA)	Onset potential of H_2 evolution (E_{WE} vs. SCE)	Volume of H_2 evolved in 300 s (cm^3)	Tafel slope (β_C) (mV.dec^{-1})
773	-39.14	-0.73	11.11	40.51
873	-30.02	-0.84	10.34	67.45
973	-21.84	-0.87	9.09	71.47
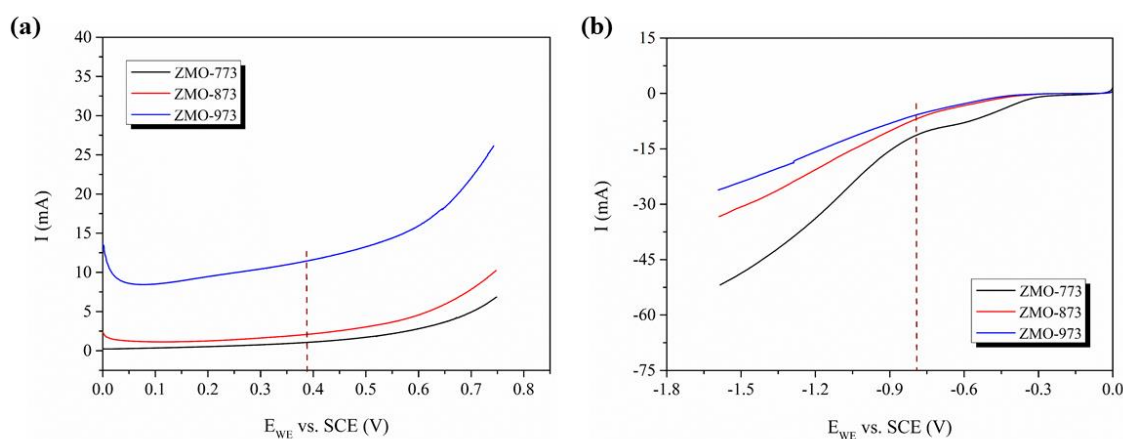
Fig. 4.2 (a-b) LSV curves for HER and OER of ZMO nanofibers at different calcination temperatures.

The electrochemical stability is considered to be an important property of electrocatalysts for real time applications. In this regard, the stability of ZMO nanofibers were evaluated by CP technique (Fig. 4.1 (b)). The constant current applied across the WE and CE causes the reduction of H^+ ions at the WE surface and continuous liberation of H_2 gas. The potential developed at the WE with respect to RE depends on the stability and efficiency of the electrode material and the redox couples available within the medium during the reaction (Elias and Hegde 2016). The CP study for HER was carried out at a constant current of -300 mA for a time period of 3600 s. The optimal current was selected based on the amount of H_2 gas liberated at different currents in ZMO-773. The hydrogen gas liberated from the ZMO/GE electrodes at different calcination temperatures were measured for the initial time duration of 300 s (Fig. 4.1

(c)). The maximum H_2 gas evolution was obtained for ZMO-773, which is in line with CV results. There is no substantial change in potential with the evolution of H_2 gas, suggesting the better stability of this electrocatalyst towards HER.

4.1.5. Oxygen evolution reaction

The electrocatalytic activity in OER of ZMO nanofibers obtained at different calcination temperatures was studied in the same manner as HER.

The CV analysis was carried out at a potential range of 0 to 0.75 V at an optimal scan rate of 100 mV.s^{-1} for 50 cycles in 1 M KOH (Fig. 4.3 (a)). The electrocatalytic activity towards OER was assessed from the anodic peak current, and the onset potential obtained from the CV plots and are presented in table 3. The onset potential is the minimum potential at which the formation of oxygen takes place at the electrode surface under the given conditions. It was observed that ZMO-973 exhibited the maximum electrocatalytic activity towards O_2 evolution reaction with the lowest onset potential of 0.39 V, which is lesser than that of the commercial RuO_2/GE (0.405 V) shown in Fig. I.6, suggesting its better elctrocatalytic activity towards OER. The electrocatalytic activity towards OER was further studied using LSV. The LSV measurements were carried out at a positive potential range of 0 to 0.75 V at a scan rate of 100 mV.s^{-1}. The LSV curves correspond to OER of ZMO nanofibers are shown in Fig. 4.2 (b). The results are in line with the CV results in which maximum electrocatalytic performance towards OER was obtained for ZMO-973.

The stability and efficiency of ZMO/GE towards OER was studied using CP method. The oxygen evolution was measured similarly as HER was carried out, and the corresponding chronopotentiogram is shown in Fig. 4.3 (b). A positive current pulse of +300 mA was applied, and the O_2 evolved was measured over a time duration of 3600 s. Initially, there was a drastic increase in potential until an equilibrium was reached at which OH$^-$ oxidizes to O_2. At this equilibrium condition, the oxygen gas bubbles start forming as well as escaping from the ZMO/GE surface, keeping the potential stable throughout the reaction with the continuous evolution of O_2 gas. The amounts of oxygen liberated from ZMO/GE electrodes at different calcination temperatures were measured at the initial 300 s and are shown in Fig. 4.2 (c). The maximum O_2 evolution was observed for the sample ZMO-973. The highest OER performance may be due to

the affinity of active sites at the surface of the WE towards the OH⁻ adsorption, especially cations that are present at the octahedral sites of the spinel oxide. The cations present at the tetrahedral site of spinel oxides are difficult to oxidize or reduce than that of the octahedral site cations (Lee et al. 2013; Lu et al. 2011).
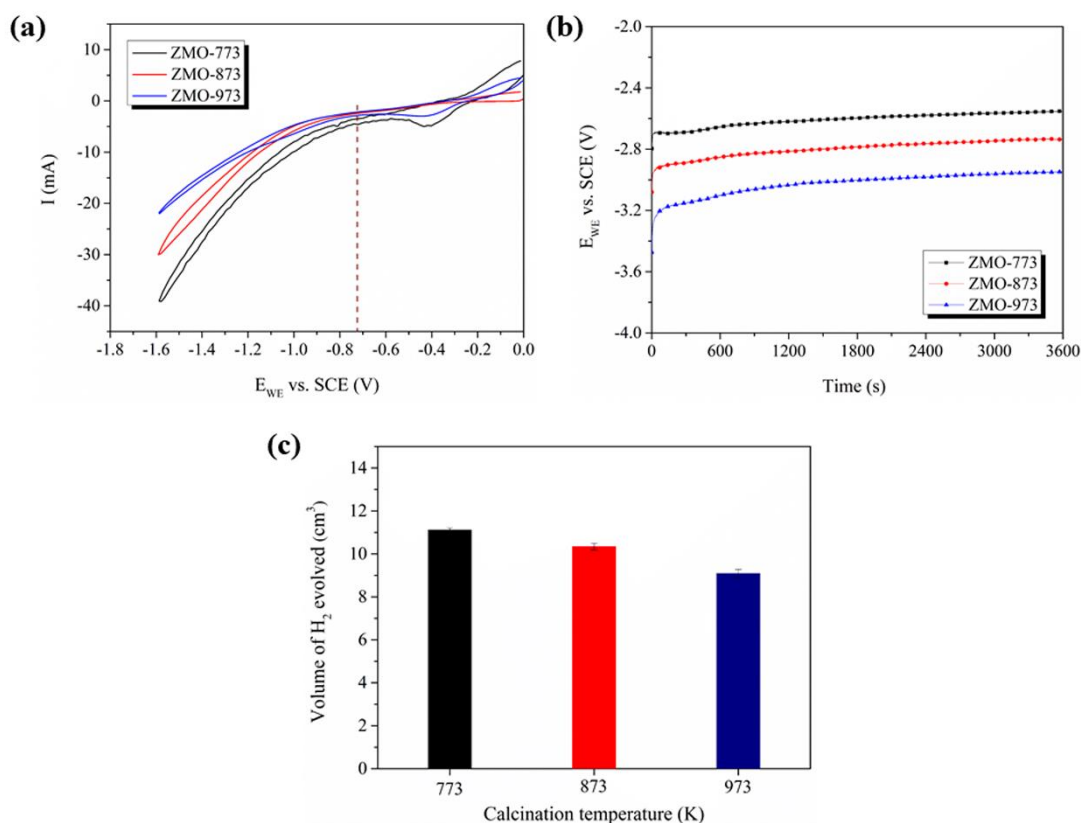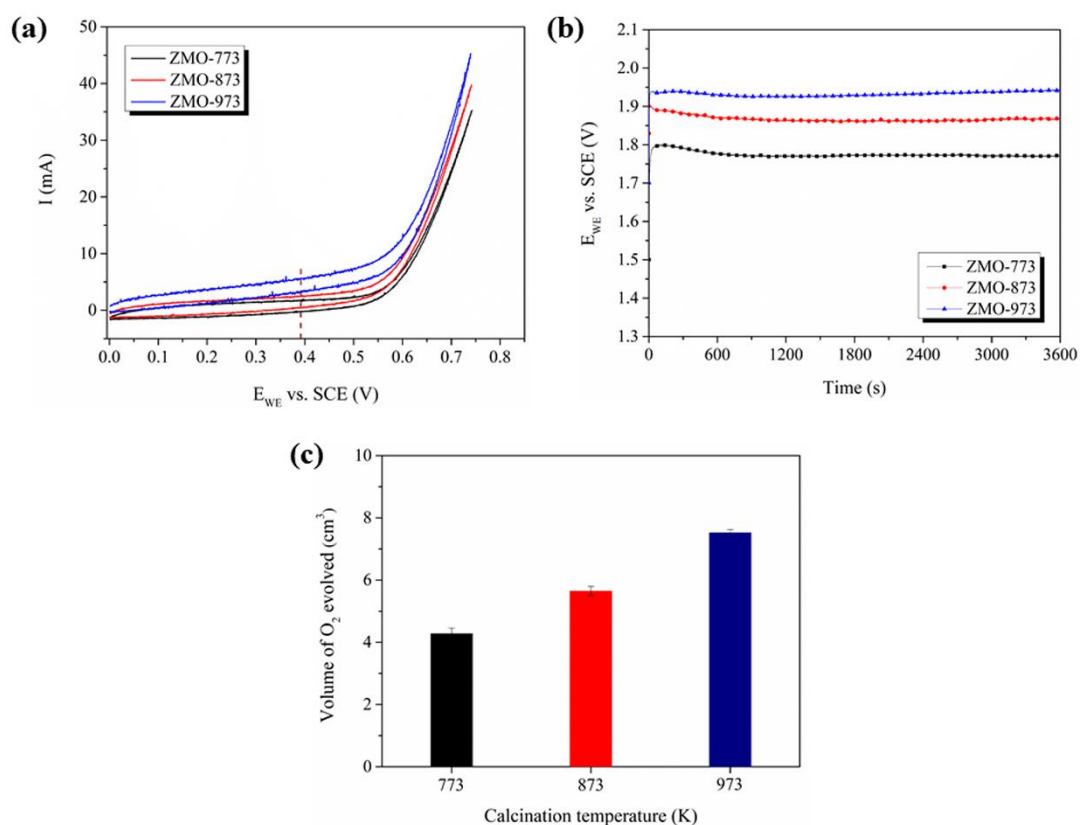

Fig. 4.3 (a-b) CV curves and CP stability response for OER of ZMO nanofibers at different calcination temperatures and (c) respective evolution of O_2 after 300 s.

Table 4.3 OER parameters for ZMO nanofibers at different calcination temperatures

T (K)	Anodic peak current at 0.75 V (mA)	Onset potential of O_2 evolution (E_{WE} vs. SCE)	Volume of O_2 evolved in 300 s (cm^3)	Tafel slope (β_a) (mV.dec⁻¹)
773	35.20	0.45	4.28	74.52
873	39.77	0.42	5.65	50.94
973	45.27	0.39	7.52	48.08

4.1.6. Tafel polarization plot
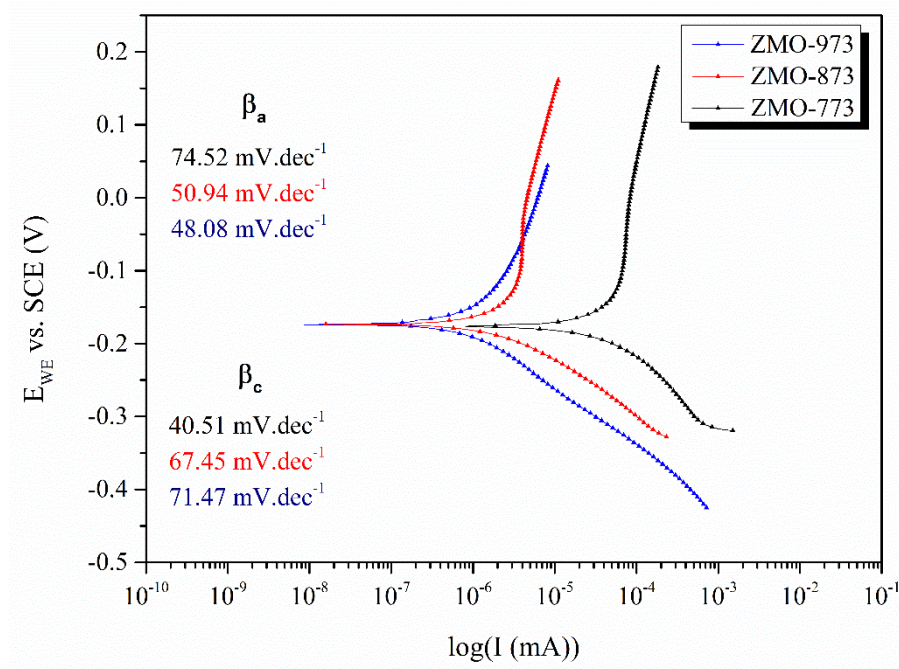
Fig. 4.4 Tafel polarization plots for HER and OER of ZMO nanofibers at different calcination temperatures.

The Tafel polarization plot provides insight into the probable mechanisms that occur at the active sites of the electrode, and the Tafel slope signifies the key nature of electrocatalyst on OER and HER. The Tafel polarization study was carried out at a potential ramp of ±250 mV from an open circuit potential with a scan rate of 1 mV.s^{-1}. The Tafel plots corresponding to ZMO/GE obtained at different calcination temperatures are shown in Fig. 4.4.

In alkaline media, HER occur in two ways either by Volmer-Heyrovsky ((4.1) and (4.2)) or Volmer-Tafel ((4.1) and (4.3)) mechanisms, based on the Tafel slope obtained from the Tafel curves (Li et al. 2016). The HER proceeds in alkaline medium, according to the following reactions.

$$M + H_2O + e^- \rightarrow MH_{ad} + OH^- \tag{4.1}$$

$$MH_{ad} + H_2O + e^- \rightarrow MH_{ad} + OH^- + H_2 \uparrow \tag{4.2}$$

$$MH_{ad} + MH_{ad} \rightarrow H_2 + 2M + H_2 \uparrow \tag{4.3}$$
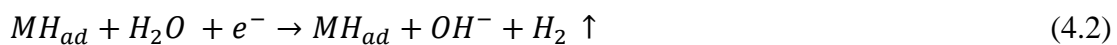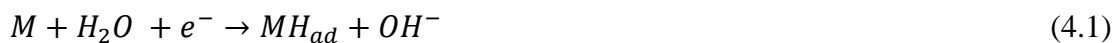
where M is the active adsorption site and MH_{ad} is the H atom adsorbed at the site. The Tafel slope is considered to be a characteristic property of electrocatalytic materials and it is a rate limiting step for electron transfer reactions. The Tafel slopes (β_C and β_a) obtained from both HER and OER are listed in Table 4.2 and Table 4.3. The HER is initiated with adsorption and discharge of proton (Volmer step) in which the molecular H_2O combines with the electrons to form adsorbed H atom and OH^- ion at the active site of the electrode. This step is followed by two pathways either electrodesorption step (Heyrovsky step) or proton recombination step (Tafel step). If the Tafel slope value $\beta_c > 100$ mV.dec^{-1} then the rate determining step is considered to be Volmer. If $\beta_c \sim 30$ or 40 mV.dec^{-1} then the rate determining step will be Tafel or Heyrovsky step (Choquette et al. 2016). ZMO-773 exhibited better electrocatalytic behavior towards HER and the rate limiting reactions follow Volmer-Heyrovsky mechanism ($\beta_c \sim 40$ mV.dec^{-1}). The β_c for commercial Pt/C/GE is found to be ~ 116.4 mV.dec^{-1}, which is higher than that of ZMO/C/GE suggesting its better performance in HER compared to Pt/C/GE.

The least Tafel slope was obtained for ZMO-973 (48.08 mV.dec^{-1}) and it exhibited high OER compared to ZMO-773 and ZMO-873. In alkaline medium the OER proceeds with the following reactions, which involves adsorption of OH and O ions at the active site and subsequent formation of O_2. The β_a for commercial RuO$_2$/GE is found to be ~ 68.2 mV.dec^{-1}, which is comparable with that of ZMO/C/GE suggesting its better performance in OER.

$$M + OH^-(aq) \rightarrow M - OH + e^- \tag{4.4}$$

$$M - OH + OH^-(aq) \rightarrow M - O + H_2O + e^- \tag{4.5}$$

$$2(M - O) \rightarrow 2M + O_2 \uparrow \tag{4.6}$$
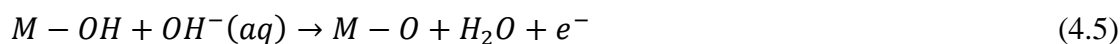
4.2. SUMMARY AND CONCLUSIONS

Sol-gel assisted electrospinning technique was used to prepare ZMO nanofibers. The unique features associated with the polymeric binder SAN, lead to the improved morphological and structural properties of ZMO nanofibers. Among the ZMO nanofibers obtained at different calcination temperatures ZMO-773, which is having the highest surface area exhibited maximum electrocatalytic behavior towards the HER.

It is a favorable cathode material for water-splitting in alkaline media. Besides, it exhibited weak electrocatalytic performance in OER due to its low affinity towards OH⁻ adsorption. The maximum efficiency towards OER was observed for ZMO-973 due to the affinity of active sites at the WE towards the OH⁻ adsorption. In summary, it follows that ZMO-773 and ZMO-973 exhibited the highest electrocatalytic behavior towards HER and OER, respectively. The results prove that ZMO nanofibers are promising candidates as bifunctional electrocatalyst towards water-splitting.

PART - II

CHAPTER 5

CHAPTER 5

EFFECT OF POLARIZATION SWITCHING ON PIEZOELECTRIC AND DIELECTRIC PERFORMANCE OF ELECTROSPUN NANOFIBERS OF PVDF/Ca-Al LDH NANOCOMPOSITE

The present study reports a new synthetic route for CAL nanosheets and incorporation of these 2D nanosheets as filler material into PVDF to produce composite nanofibers by electrospinning. The polymorphism, crystallinity, and the interaction between PVDF and LDH were studied by FTIR, XRD, and DSC. The synergetic effect of PVDF-LDH interaction and in situ stretching due to electrospinning facilitates the nucleation of electroactive β-phase up to 82.79%, which make it a suitable material for piezoelectric based nanogenerators. The piezoelectric performance of PCAL composite nanofibers was demonstrated by hand slapping and frequency dependent mechanical vibration mode which delivers a maximum open circuit output voltage of 4.1 V and 5.72 V respectively. Moreover, the composite nanofibers exhibited a high dielectric constant and low dielectric loss due to superior interfacial polarization at low-frequency region with LDH loading, promising its potential applications in electronic devices.

5.1. RESULTS AND DISCUSSION

5.1.1. Characterization of CAL

The XRD patterns corresponding to CAL are shown in Fig. 5.1. All the reflections were indexed to the hexagonal phase of calcium aluminum oxide nitrate hydroxide hydrate clay minerals with layered structure (ICDD (International Centre for Diffraction Data) database (00-050-0652)). No other impurity peaks were seen in the XRD results. The interlayer space was calculated from the (003) diffraction plane using Bragg's equation and is found to be 8.9 Å.

Further confirmation of CAL formation was carried out by FTIR. The FTIR spectrum of as-prepared CAL was shown in Fig. 5.2. The bands at 3641 and 3491 cm^{-1} are attributed to the O-H stretching vibration of interlayer water molecules and that

of corresponding metal hydroxides. The band at 1621 cm^{-1} is associated with bending vibration of interlayer water molecules. The strong band centered at 1382 cm^{-1} relates to the stretching vibrations of NO$_3^-$ ions intercalated at the interlayer space of LDH. The bands at 789, 576, 532 and 424 cm^{-1} are ascribed to the metal-oxygen (Ca^{2+}/Al^{3+}) lattice vibrations (M−O, M−O−M and O−M−O) (Abdolmohammad-Zadeh and Kohansal 2012; De Sá et al. 2013).
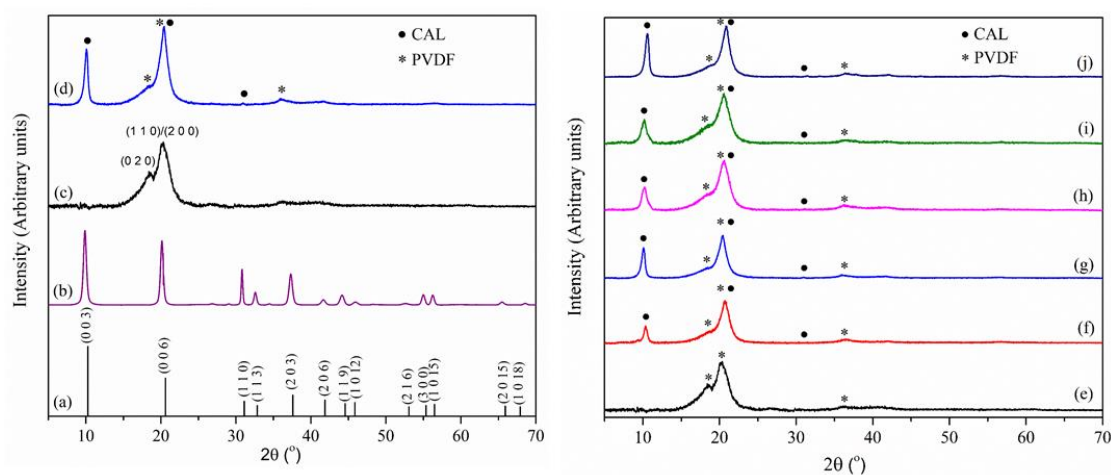
Fig. 5.1 X-ray diffractograms corresponding to (a) ICDD (00-050-0652) (b) CAL (c) PVDF (d) PCAL-5 and PVDF nanofibers with LDH loading of (e) 0% (f) 2.5% (g) 5% (h) 7.5% (i) 10% (j) 12.5%, respectively.
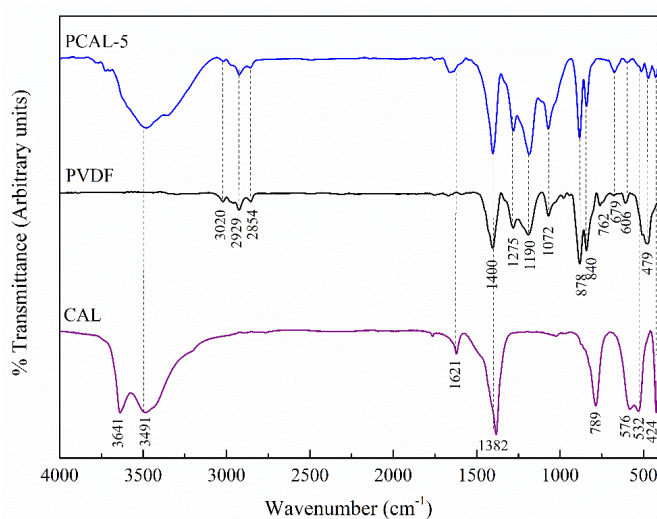
Fig. 5.2 Fourier transform infrared spectra of Ca-Al LDH nanosheets, PVDF, and PCAL-5 composite nanofibers.

The morphological features of CAL were examined by SEM and TEM. Fig. 5.3 shows the SEM images of CAL at different magnifications. The crystallites exhibit plate-like morphology with a thickness of a few nm and a lateral distance of a few μm, which is the characteristic feature of layered materials. The elemental analysis of CAL was carried out using EDS shown in Fig. 5.3. The presence of Ca, Al, N, and O was confirmed from the analysis. Layered morphology of CAL was further confirmed from TEM analysis (Fig. 5. 4(a-b)). Along with layered structures, hexagonal platy structures were also observed. The interplanar space of 0.1356 and 0.1736 nm obtained from the TEM image was in good agreement with the lattice planes (1 0 18) and (2 1 6) of hexagonal CAL. Alike, from the SAED pattern the planes (1 1 0), (2 0 6), (1 0 12) and (3 0 0) were matched to that of hexagonal CAL. SAED pattern revealed the polycrystalline nature of CAL.
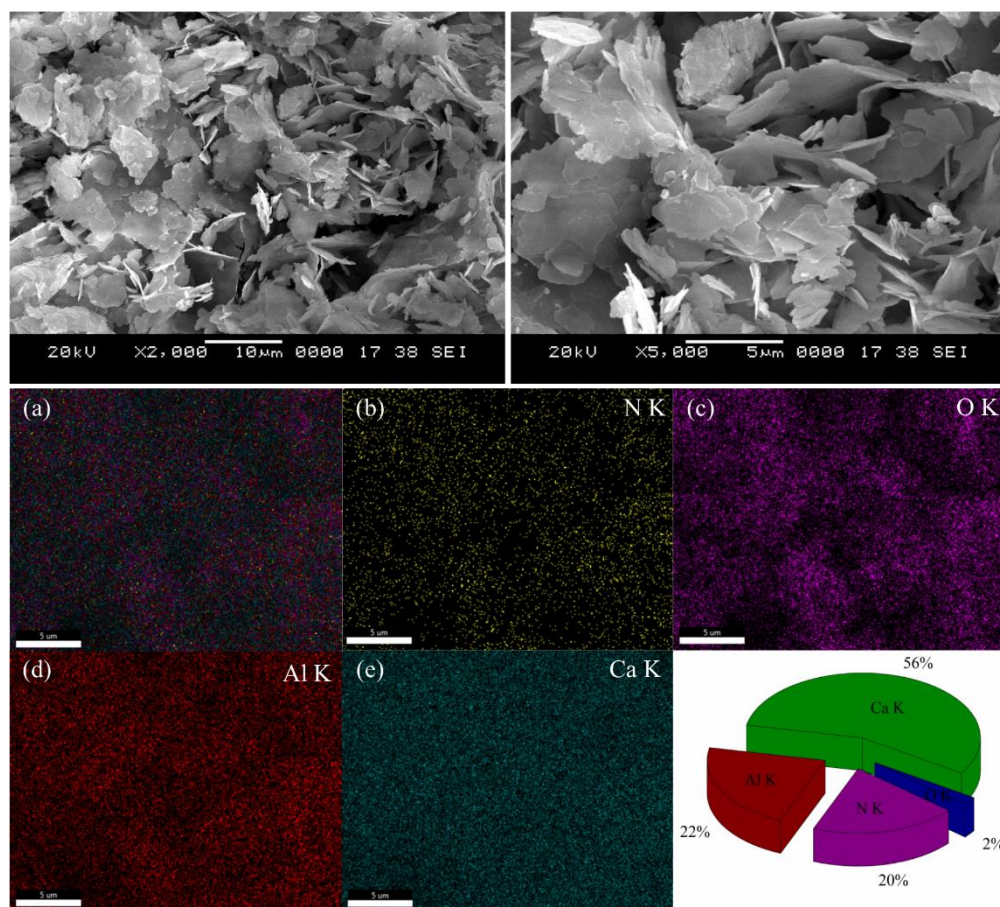
Fig. 5.3 SEM images of CAL at different magnifications and (b-e) elemental distribution of Ca-Al LDH ((a) overall distribution).

The thermal stability of CAL was assessed by TG-DTG analysis (Fig. 5.5). The percentage mass loss of 9.94% up to 160 °C was due to physically adsorbed water. The second mass loss from 240 to 330 °C was attributed to the partial dehydroxylation of metal hydroxide layers. This step was followed by a mass loss of 13.99% on heating up to 630 °C, which corresponds to the decomposition of interlayer nitrate anions. The final step from 620 °C onwards was due to the further decomposition of hydroxide layers and interlayer species, which further leads to the formation of a final product of corresponding metal oxides (Chakraborty et al. 2017; Dutta and Pramanik 2013).
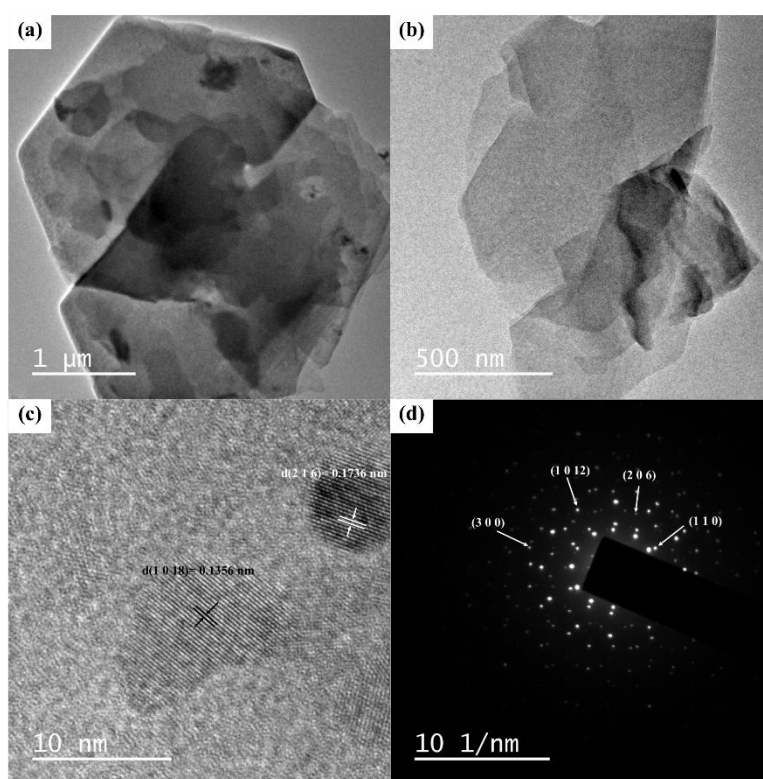
Fig. 5.4 TEM micrographs (a-b), high resolution image showing d-value (c) and SAED pattern (d) of CAL nanosheets.

5.1.1.1. Mechanism of formation of CAL

$$2Al + 6H_2O \rightarrow 2Al(OH)_3 + 3H_2 \tag{5a}$$

$$Ca(NO_3)_2.4H_2O \rightarrow Ca^{2+} + 2NO_3^- + 4OH^- + 4H^+ \tag{5b}$$

$$(1-x)Ca^{2+} + xAl(OH)_3 + {}^x/_2 NO_3^- + (2-3x)OH^- + mH_2O \rightarrow$$

$$Ca_{1-x}Al_x(OH)_2(NO_3)_{x/_2}.mH_2O \tag{5c}$$
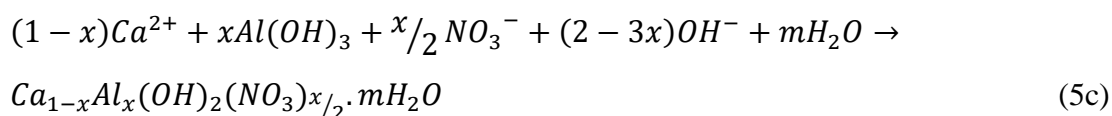
The proposed mechanism of formation of CAL is shown in equations (5 a-c). During the reaction, the $Al(OH)_3$ was released from the Al sheet. The formation of $Al(OH)_3$ was confirmed by XRD analysis of partially reacted Al sheet, which was taken amidst the experiment (Fig. II.1). This will further react with Ca^{2+}, NO_3^- and OH^- and lead to the formation of CAL. An almost similar mechanism of formation of Mg-Al LDH was proposed by wang et al. (Wang et al. 2014). However, herein the reaction was carried out in an N_2 atmosphere in order to avoid the formation of $CaCO_3$. As the reaction time proceeds, the LDH crystals assembled to form uniform flake-like structure.
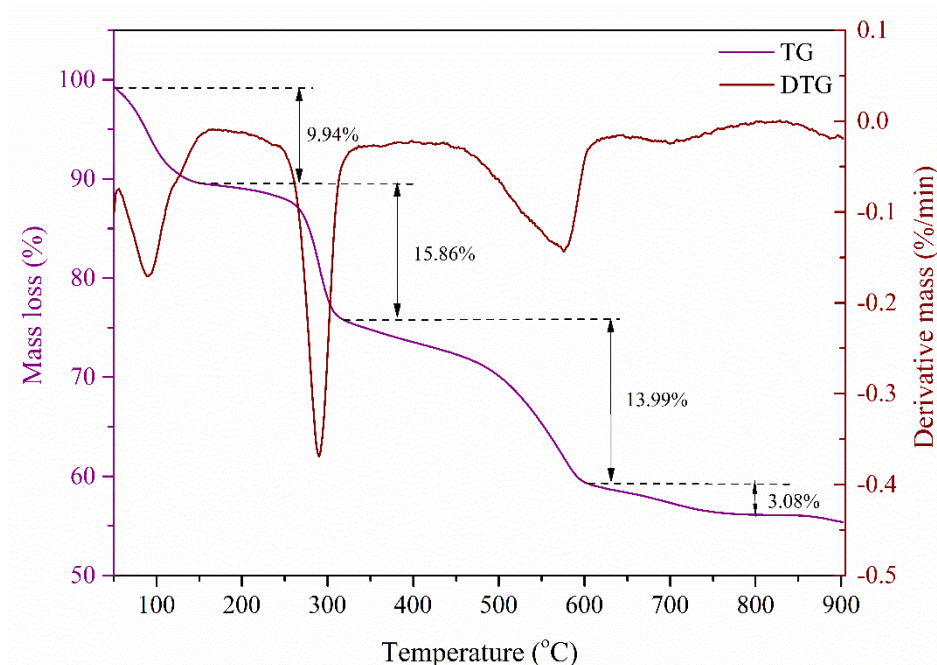
Fig. 5.5 TG-DTG plots of CAL nanosheets.

5.1.2. Characterization of PCAL composite nanofibers

5.1.2.1. Morphological studies

The morphological studies of as prepared PVDF and PCAL composite nanofibers were carried out using SEM and TEM. The SEM images of PVDF and PCAL composite nanofibers were shown in Fig. 5.6. It is worth mentioning that the obtained fibers were extremely smooth and uniform. After the addition of filler, the fiber diameter was found
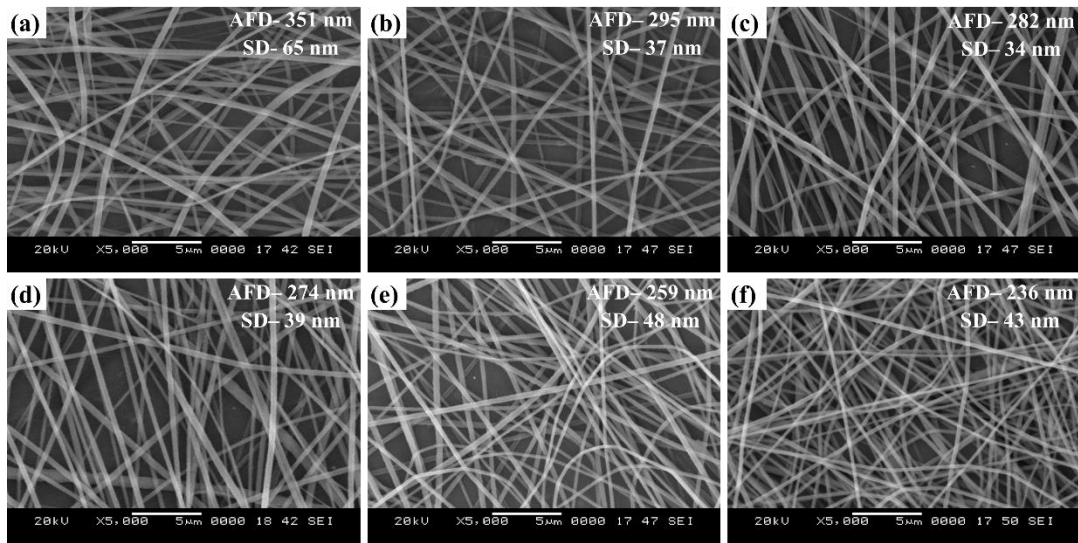
Fig. 5.6 SEM images of electrospun nanofibers (a) PVDF (b) PCAL-2.5 (c) PCAL-5 (d) PCAL-7.5 (e) PCAL-10 (f) PCAL-12.5. Average Fiber Diameter (AFD) and Standard Deviation (SD) are presented in figure.
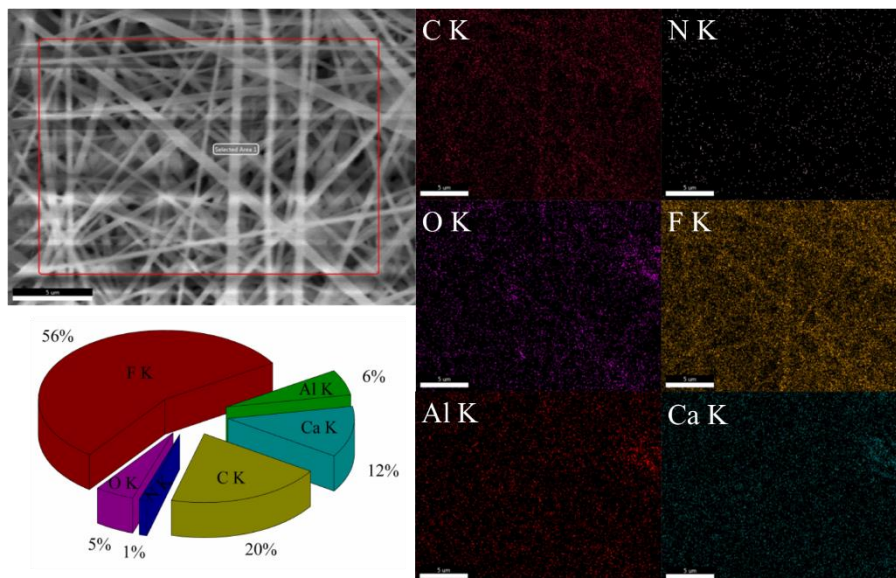
Fig. 5.7 Elemental mapping of PVDF nanofibers with 7.5% LDH loading.

to be decreased compared to that of the pristine PVDF nanofibers. This is due to the presence of divalent/trivalent cations and interlayer anions present in the LDH that facilitates the surface charge density of the polymeric solution. This electrospinning jet with excess charge undergoes higher stretching and whipping process under the influence of electric field, which leads to the formation of uniform long continuous

defect-free fibers with a smaller diameter (Haider et al. 2018; Zong et al. 2002). Elemental mapping carried out for PCAL-7.5 was shown in Fig. 5. 7, which revealed a uniform distribution of elements C, N, O, F, Al and Ca throughout the fiber surface that confirms the homogeneous dispersion of LDH in the PVDF matrix.

The TEM image of PCAL composite nanofibers was shown in Fig. 5.8. It is observed that the LDH sheets are well dispersed in the PVDF matrix. The well dispersed LDH sheets ensure good interaction between the F atoms of the PVDF and OH groups of the LDH sheets, which may be favorable to obtain good piezoelectric response (Tian et al. 2017).
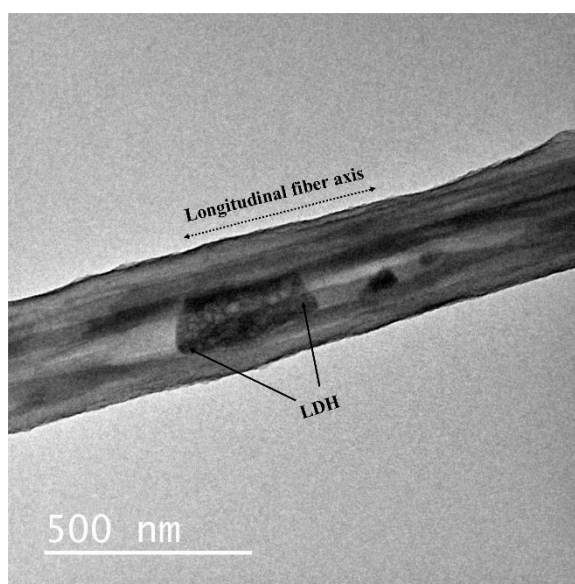
Fig. 5.8 TEM image of PVDF nanofibers with 5% LDH loading.

5.1.2.2. FTIR analysis

The crystalline phase identification of PVDF and PVDF composite nanofibers is of great interest, so further studies were carried out using FTIR spectroscopy. Fig. 5.9 shows the FTIR spectra of PVDF and PCAL composite nanofibers. The existence of α and β-phases was confirmed from the analysis. The characteristic absorption bands observed at 762 and 795 cm^{-1} exclusively correspond to α-phase of PVDF and the bands at 1430, 1400, 1275, 1178, 1072, 878 and 840 cm^{-1} were assigned to the β-phase of PVDF (Ahn et al. 2013). Still, there is confusion regarding the assignment of the band at 840 cm^{-1} because it attributes to both β and γ-phase respectively. However, in the

present study, this band can be assigned to the β-phase since there is no band at 1234 cm^{-1}, which is the characteristic band corresponding to the γ-phase (Cai et al. 2017). With the percentage of LDH loading, there was a predominant increase in the β-phase whereas the α-phase diminishes. The β-phase content was calculated using the following equation (5.1) and are summarized in Table I.

$$F(\beta) = \frac{A_\beta}{\left(\frac{K_\beta}{K_\alpha}\right)A_\alpha + A_\beta} \tag{5.1}$$

where A_α and A_β represent the absorbance at wavenumbers 763 and 840 cm^{-1}, and K_β $(7.7 \times 10^4\ cm^2\ mol^{-1})$ and K_α $(6.1 \times 10^4\ cm^2\ mol^{-1})$ represent the absorption coefficients corresponding to the respective wavenumbers. A drastic improvement in the β-phase content was observed in the PVDF nanofibers with the LDH loading, which is mainly due to the cooperative effect of PVDF-filler interaction and *in situ* stretching due to electrospinning. The maximum β-phase was noted in PCAL-5 beyond which there was a decrement in the β-phase content. This may be due to the excess addition of LDH that may lead to the hindering of chain mobility that further led to poorer interaction between PVDF-LDH. The possible interaction mechanism between PVDF and CAL nanosheets was explained briefly in forthcoming section.
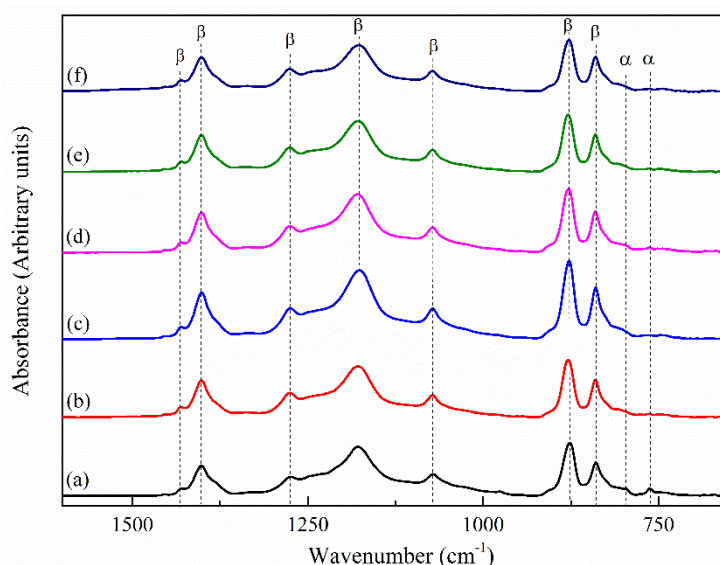
Fig. 5.9 FTIR spectra of electrospun nanofibers (a) PVDF (b) PCAL-2.5 (c) PCAL-5 (d) PCAL-7.5 (e) PCAL-10 (f) PCAL-12.5.

5.1.2.3. XRD analysis

XRD patterns corresponding to the PVDF, and PCAL-5 are shown in Fig. 5.1 and the deconvoluted diffraction pattern of respective samples was shown in Fig. 5.10 and Fig. II.2. The peaks at 18.3° and 26.7° correspond to the α-phase of PVDF. The peak at 20.37° is attributed to the sum of diffraction patterns of (110) and (200) planes of the electroactive β-phase of PVDF nanofibers. In Fig. 5.10 (b) the deconvoluted peaks at 19.9° and 20.51° correspond to the α and β-phases of PCAL-5 and the peak at 20.9° is attributed to the (006) plane of CAL. It was observed that one of the characteristic peaks corresponds to the α-phase had disappeared in PCAL-5, and the intensity of the peak corresponding to the β-phase has increased, which is in good agreement with the FTIR results. The small shift in the peaks with the addition of CAL may be due to the interaction between the LDH and the PVDF matrix in the nanocomposite (Jahan et al. 2017). The degree of crystallinity was calculated from the following equation,

$$\chi_{C=} \frac{\sum A_c}{\sum A_c + \sum A_a} \times 100\% \qquad (5.2)$$

where $\sum A_c$ and $\sum A_a$ denote the summation of integrated areas of crystalline peaks and amorphous halos, respectively. It has been observed that in PCAL composite nanofibers there was a slight decrease in the crystallinity up to PCAL-5 and with the further addition of CAL the crystallinity increased up to 51.51%. This may be due to the excess addition of filler, which will hinder the polymer chain mobility.
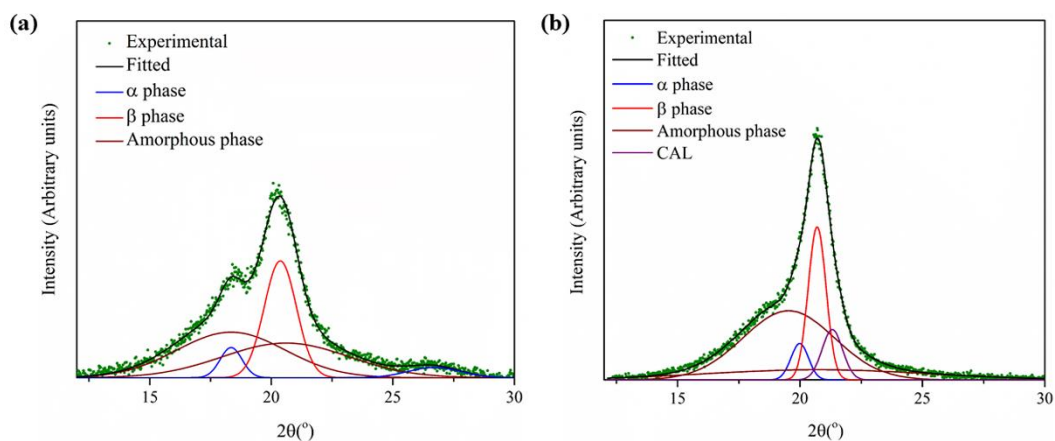
Fig. 5.10 Deconvoluted XRD patterns of (a) PVDF (b) PCAL-5.

5.1.2.4. DSC and TGA analysis
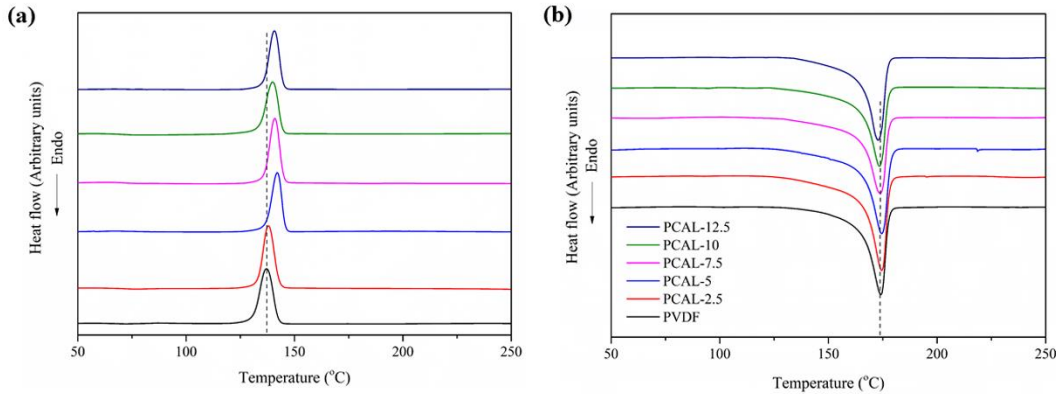
Fig. 5.11 DSC traces of PVDF and PCAL composite nanofibers during (a) first cooling cycle (preceded by first heating cycle) and (b) second heating cycle.

The thermal behavior of PVDF and PVDF composite nanofibers were examined by DSC and TGA techniques. DSC cooling and heating curves of PVDF and PVDF composite nanofibers are shown in Fig. 5.11. It was observed that with the addition of CAL the crystallization temperature (T_c) of the nanofibers shifted to higher values up to PCAL-5 and then there was a slight decrease in it. This can be attributed to the presence of CAL filler, which accelerates the crystallization of β-PVDF. The high T_c refers to the uniform dispersion of CAL in the PVDF matrix and interfacial adhesion of aforementioned filler and polymer matrix, respectively. The presence of hydroxyl functional groups present at the surface of the LDH is beneficial for the crystallization of β-PVDF. The endothermic peak present in Fig. 5.11(b) corresponds to the melting temperature (T_m) of the crystalline phases present in the nanocomposite. In this case, it is the superposition of melting temperatures correspond to all the crystalline phases present, such as α and β. T_m also exhibits a similar trend as T_c which may be due to the presence of β-phase (Priya and Jog 2003).

The degree of crystallinity was calculated using the equation,

$$\chi_{C=}\ \frac{\Delta H_f}{\Delta H_f^0} \times 100\%$$ (5.3)

where, ΔH_f and ΔH_f^0 represents the enthalpy of fusion for the sample (Jg^{-1}) and 100% crystalline PVDF (104.7 Jg^{-1}), respectively. The crystallinity is found to be decreased up to PCAL-5 and then increased for further loading which is in agreement with the

XRD results. Overall the filler CAL is acting as nucleating agent for the crystallization of PVDF.

The TGA plots of PVDF and PVDF composite nanofibers are shown in Fig. 5.12. In PVDF the decomposition takes place by chain depropagation mechanism in which the C-H and C-F scission occurs and leads to the formation of HF in the presence of hydrogen and fluorine radicals (Sebastian et al. 2016). It was observed that the decomposition of composite nanofibers started at low temperature compared to that of PVDF. This may be because CAL accelerates the chain scission process due to the presence of OH groups (Khalifa et al. 2016).
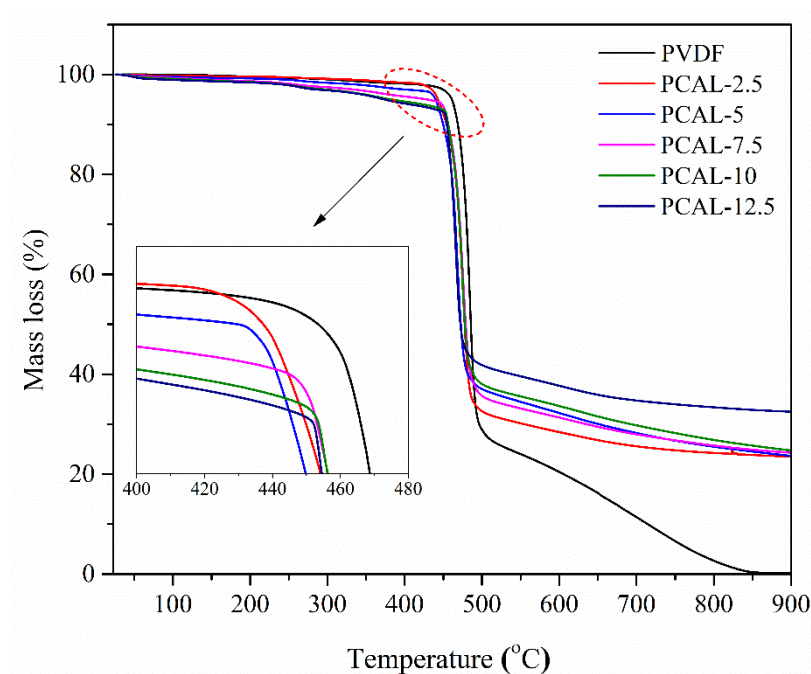
Fig. 5.12 TGA plots of PCAL composite nanofibers.

5.1.2.5. *Mechanism of interaction between LDH layers and PVDF in PCAL nanofibers*

Based on FTIR results, the possible interactions between LDH and PVDF in PCAL composite nanofibers were shown in Fig. 5.13. After LDH loading a new vibrational peak appeared in IR-spectrum of PCAL at 3100-3700 cm^{-1} range, which corresponds to the stretching vibration of OH groups present in LDH. Moreover, this peak exhibited peak broadening as well as slight shift compared to that of LDH peak. This confirms the strong affinity of OH groups present in the LDH to the electronegative F atoms in

the -CF$_2$- dipoles of PVDF and leads to H bond formation, which is illustrated in Fig. 5.13 (Tian et al. 2017). This interaction further leads to the all trans (TTTT) *in situ* orientation of PVDF chains leading to the formation of β-PVDF. Along with the effective polymer-filler interaction, high stretching ratio of solution jet in electrospinning will lead to the crystallization of the β-phase in PVDF. Therefore, PCAL composite nanofibers were expected to exhibit better piezoelectric and dielectric performance.
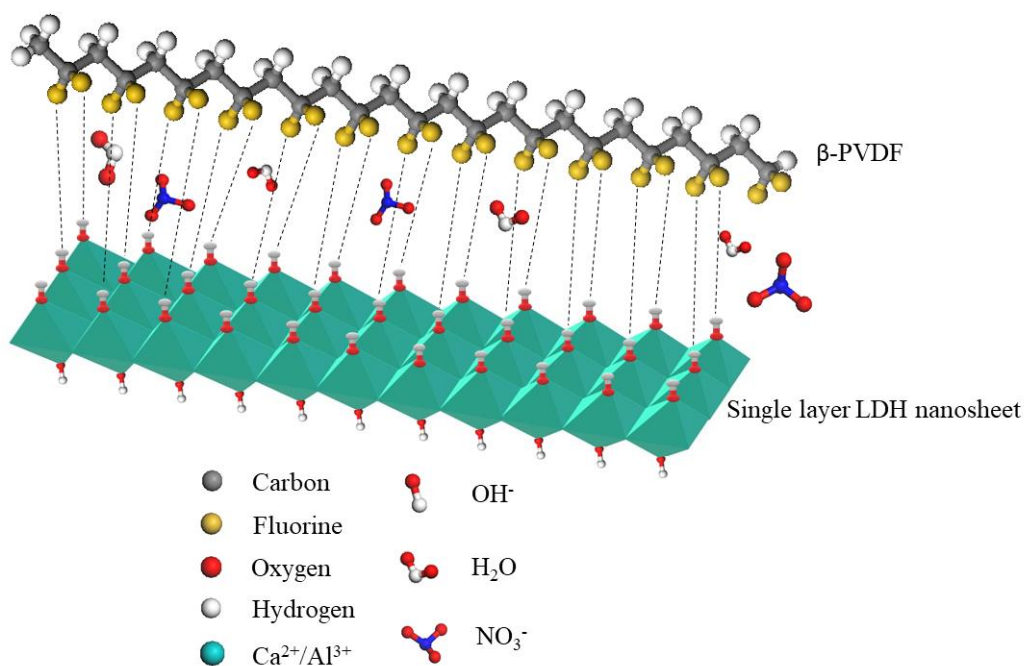
Fig. 5.13 Schematic representation of the interaction between PVDF and CAL nanosheets.

5.1.2.6. Piezoelectric studies

The piezoelectric response of PCAL nanofibers was studied using an in-house developed experimental set up. The piezoelectric response was studied using two modes, namely hand slapping mode and frequency dependent mechanical vibration mode. In hand slapping mode, the PCAL nanofiber mat (4.6 cm^2 area) was sandwiched between two interdigitated copper electrodes which was covered by an insulating film as shown in Fig. 2.3. The PCAL nanogenerator was imparted repeatedly by hand slapping to investigate the piezoelectric performance, and the output voltage was measured by an oscilloscope. The obtained output voltage for different loadings of CAL
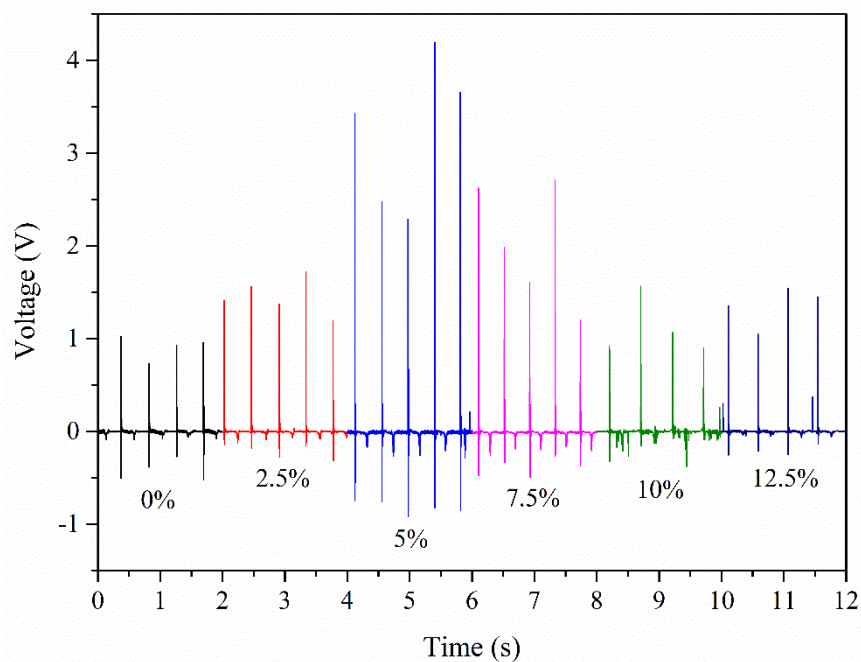
Fig. 5.14 Piezoelectric response of PCAL composite nanofibers under hand slapping mode.
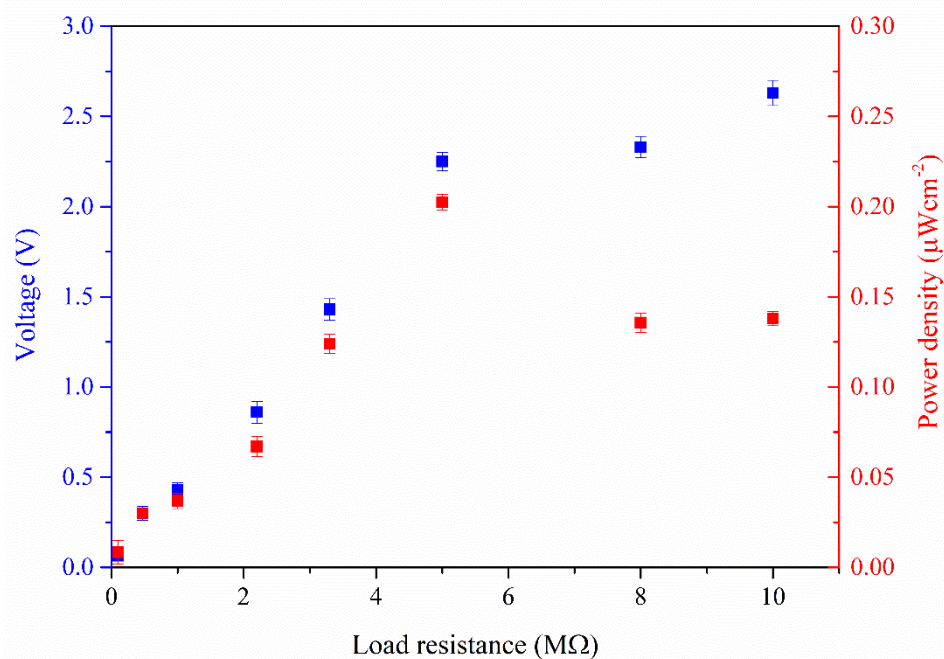
Fig. 5.15 Output voltage and power density plot of PCAL-5 nanofibers under hand slapping mode.

is shown in Fig. 5.14. The maximum output voltage of 4.1 V was obtained for the PVDF nanofibers with 5% LDH loading, and it gets abridged for further loading. These results

are proportional with the β-phase content of PCAL nanofibers reported in the Table I. The power density of nanogenerator under hand slapping mode was calculated using the equation,

$$P = \frac{V^2}{R_L.A} \tag{5.4}$$

Where, V is the output voltage, R_L is the load resistance and A is the effective area of the nanogenerator (4.6 cm^2). The power density, voltage and current of PCAL-5 composite nanofibers were calculated at different load resistance and were plotted in Fig. 5.15. The optimum power density of 0.2 µWcm^{-2} was obtained at a load resistance of 5 MΩ beyond which it decreased.

The piezoelectric response obtained by frequency dependent mechanical vibration for PCAL-5 is shown in Fig. 5.16. The PCAL nanogenerator was excited by a piezo stack actuator system using the amplified sinusoidal signal generated from the signal generator (3 V$_{PP}$, frequency ranges between 10 Hz- 150 Hz). The piezo stack actuator was placed between the base and the sample handle. The nanogenerator consists of PCAL nanofibers (9.6 cm^2 area) sandwiched between the adhesive copper
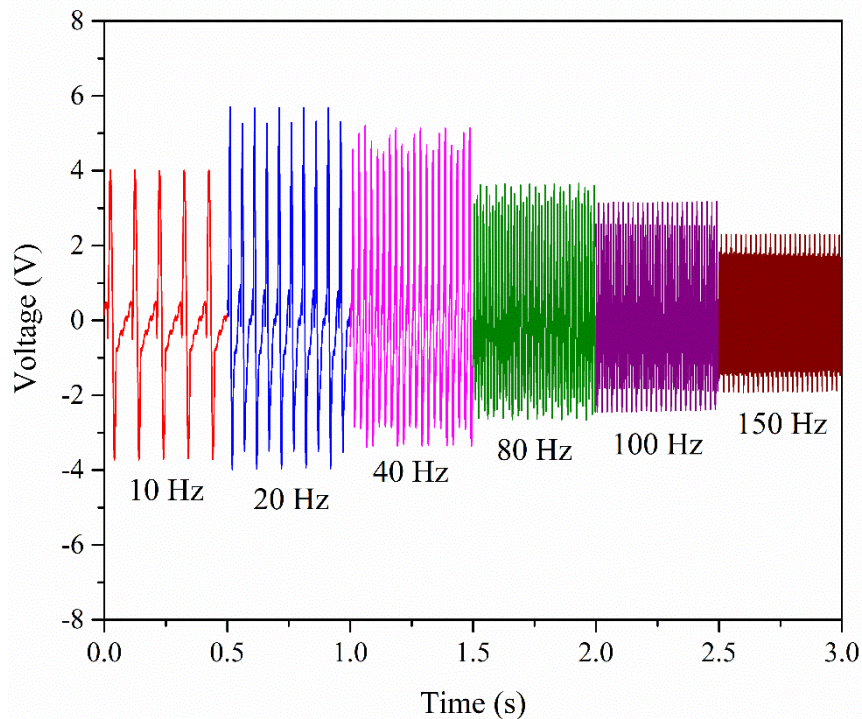
Fig. 5.16 Piezoelectric response of PCAL-5 nanofibers under mechanical vibration mode.

tapes (Fig. 2.4). The output voltage generated was measured by using an oscilloscope attached to the nanogenerator. Fig. 5.16 shows the output voltages generated for the PCAL-5 nanofibers at different frequency ranges. The substantial output voltage of 5.72 V was obtained at a frequency of 25 Hz beyond which there was a tremendous decrease in output voltage. This is because at lower frequency range the dipoles will get aligned in the direction of mechanical vibration and will get enough time for relaxation, but at higher frequency range the dipoles will not get sufficient time to reorient themselves. Compared to most of the nanogenerators reported, the PCAL nanogenerator showed improved piezoelectric performance, which is summarized in Table II.1.

Table 5.1 Degree of crystallinity, β-phase content and melting temperature of electrospun PCAL composite nanofibers.

Sample ID	χ_c (%)		β-phase content (%)	T_m (°C)
	XRD	DSC	FTIR	DSC
PVDF	34.7	30.81	45.45	174
PCAL-2.5	40.79	31.89	78.87	174.4
PCAL-5	39.91	31.48	82.79	174.6
PCAL-7.5	45.03	32.26	80.41	173.6
PCAL-10	49.30	32.60	78.69	173.2
PCAL-12.5	51.51	33.37	77.77	172.7

5.1.2.7. Dielectric performance

Materials having a high dielectric constant and low dielectric loss are of utmost importance in energy storage applications. To investigate these parameters, dielectric studies were performed. Fig. 5.17 depicts the frequency dependent dielectric properties measured at room temperature over a frequency range of 1000-1 MHz. A tremendous increase in dielectric constant (ε') was observed in PVDF nanofibers after LDH loading
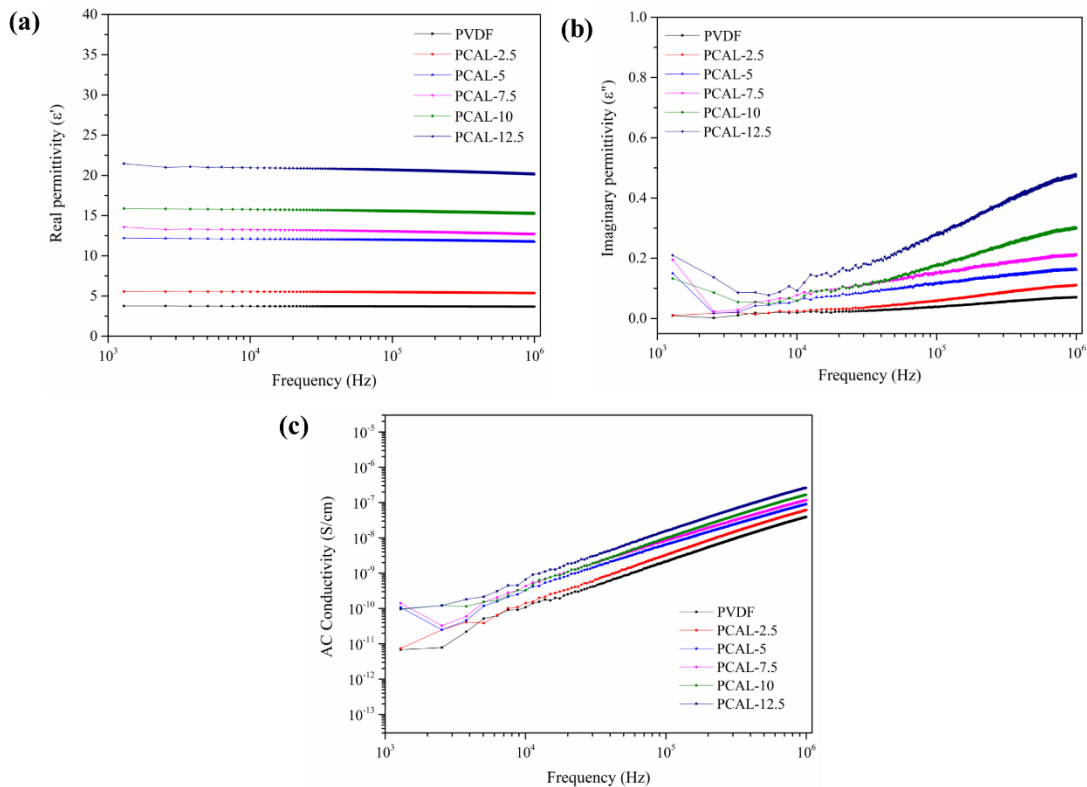
Fig. 5.17 Frequency dependence of (a) Real permittivity (ε') (b) Imaginary permittivity (ε″) and (c) AC conductivity of PVDF and PCAL composite nanofibers.

over the frequency region (1000-1 MHz). The high dielectric constant at low-frequency region is due to Maxwell-Wagner-Sillars interfacial polarization that occurs in between the interfaces of PVDF matrix and LDH at low frequency region (Chen et al. 2018; Ponnamma et al. 2018). The increase in dielectric constant is attributed to the significant polarization resulting due to the movement of space charges at the polymer-filler interface under an electric field. At low frequency, the dipoles will get sufficient time to orient themselves in the direction of applied electric field whereas at high frequency the dipoles will not get enough time to reorient themselves in the direction of applied electric field (Karan et al. 2016). Moreover, the dielectric loss showed a minimum value at low-frequency region followed by an increment at a high-frequency region, which is the essential criteria for energy storage applications. The dielectric loss increased with LDH addition. A similar trend was observed in dielectric constant with different LDH loading. The AC conductivity of PVDF nanofibers showed a linear relationship with a frequency which is the characteristic behavior of insulating polymeric materials. There

was a slight increase in conductivity values with the increase of LDH loading as shown in Fig. 5.17.

5.2. SUMMARY AND CONCLUSIONS

In summary, CAL nanosheets were synthesized by modified co-precipitation method. These nanosheets were used as the filler material in PVDF, and the nanocomposites were successfully electrospun using electrospinning equipment. The polymorphism, crystallinity and the interaction between PVDF and LDH nanosheets in the nanofibers were studied by FTIR, XRD, and DSC techniques. The FTIR measurements revealed maximum β-phase content of 82.79% for PCAL-5 composite nanofibers. The co-operative effect of LDH nanosheets and the *in situ* stretching due to electrospinning facilitates the nucleation of β-phase, which makes it a reasonable material for piezoelectric based nanogenerators. The piezoelectric performance of PCAL composite nanofibers was demonstrated by hand slapping and frequency dependent mechanical vibration mode, which generated a maximum open circuit output voltage of 4.1 V and 5.72 V, respectively. The dielectric constant increased with the increase of LDH loading which is mainly due to Maxwell-Wagner-Sillars interfacial polarization that occurs in between the interfaces of PVDF matrix and LDH. The hydroxyl groups present at the surface of LDH nanosheets make it a major hydrogen bond donor that will help in enhancing the piezoelectric and dielectric performance of PCAL composite nanofibers.

CHAPTER 6

CHAPTER 6

PVDF/Ca-Al LAYERED DOUBLE HYDROXIDE COMPOSITE GEL POLYMER ELECTROLYTE FOR HIGH-PERFORMANCE Li-ION BATTERIES

This chapter discusses the fabrication of PVDF/Ca-Al layered double hydroxide (PCAL) based GPE and its suitability as a LIB separator. The PCAL nanofibers exhibited a high β-phase content of 82.79% after the addition of CAL (which was synthesized by co-precipitation method). The synergetic effect of in situ stretching in electrospinning and interaction between PVDF and CAL plays an important role in β-phase formation in PVDF. Structural, morphological and thermal properties of nanofibers were studied using XRD, FTIR, SEM and DSC. Li/GPE/ LiCoO₂ coin cell was fabricated to study the charge-discharge behavior. The electrochemical characteristics of PCAL composite nanofibers based GPEs were studied and compared with that of PVDF and commercial Celgard® 2400 separator membrane.

6.1. RESULTS AND DISCUSSION

6.1.1. XRD Results

The XRD results corresponding to CAL, PVDF, and PCAL are shown in Fig. 6.1 (a). The diffraction peaks present in CAL are well matched with that of ICDD database 00-050-0652 of calcium aluminum layered double hydroxide that belongs to the hexagonal crystal system. The peaks at 18.3° and 26.7° correspond to the (0 2 0) and (0 2 1) reflections of α-phase and the peak at 20.3° is associated with the (1 1 0)/(2 0 0) reflections of β-phase present in PVDF. Deconvoluted XRD pattern corresponding to PCAL nanofibers is shown in Fig. 6.1 (b). The slight shift in peak position in PCAL nanofibers can be due to the interaction between PVDF and CAL. The sharp peak at 20.6° indicates the presence of high β-phase content in PCAL. The high phase content in PCAL nanofibers can be ascribed to the PVDF-LDH interaction and *in situ* stretching induced by electrospinning.
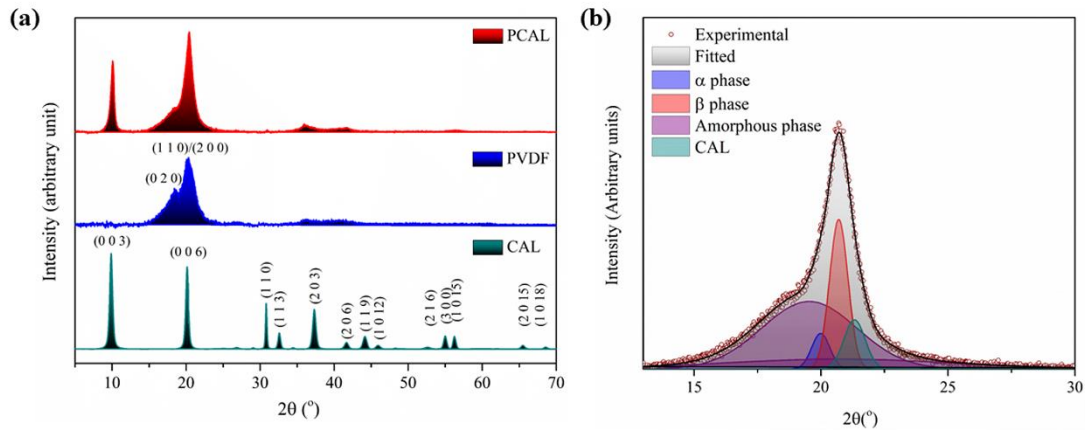
Fig. 6.1 (a) XRD patterns of CAL, PVDF, and PCAL nanofibers (b) Deconvoluted XRD pattern corresponding to PCAL nanofibers.

6.1.2. FTIR spectroscopy

FTIR spectral characterization was carried out to further investigate the phase formation in PCAL nanofibers. The FTIR absorbance spectra of CAL, PVDF, and PCAL are shown in Fig. 6.2. The bands arising at 3491 and 3641 cm^{-1} in CAL spectra correspond to the OH stretching vibration mainly due to the presence of water molecules in the interlayer space. Bands at 1382 and 1621 cm^{-1} relate to the stretching vibrations of intercalated NO_3^- ions and bending vibrations of interlayer water molecules. The bands at 424, 532, 576, and 789 cm^{-1} are attributed to the metal-oxygen lattice vibrations in Ca-Al LDH (De Sá et al. 2013).

The vibrational band at 762 cm^{-1} corresponds to the non-polar α phase of PVDF, and the characteristic peaks at 840, 1072, 1178, 1275, and 1400 cm^{-1} were assigned to the β-phase of PVDF. The absence of band at 1234 cm^{-1}, which is the characteristic band for the γ-phase in PVDF, indicates that PCAL nanofibers are composed of both α and β-phases. The bands corresponding to the α-phase diminished in PCAL nanofibers compared to that of PVDF nanofibers. The relative fraction of β-phase content was calculated using the equation (1) with the assumption that the infrared transmittance follows the Lambert-Beer law (Gregorio, and Cestari 1994).

$$F(\beta) = \frac{A_\beta}{(1.26)A_\alpha + A_\beta}$$
(6.1)

where, A_α and A_β denotes the absorbance at wavenumbers 762 and 840 cm^{-1}, respectively. The β-phase content increased from 45.45% to 82.79% in PCAL compared to that of pristine PVDF nanofibers. In LDH the divalent/trivalent metal cations are octahedrally coordinated by hydroxyl groups. In this case, CAL acts as the nucleating agent for the formation of the β-phase. The presence of hydroxyl groups leads to hydrogen bonding with the electronegative F-atoms in the -CF$_2$- dipoles of PVDF and leads to the uniform orientation of PVDF chains. The appearance of OH band at ~3500 cm^{-1} in the spectrum of PCAL nanofibers as well as a slight shift in the -CF$_2$- band present at 1275 and 1190 cm^{-1} confirms the H-bond formation in PCAL nanofibers. Along with this, the high electric field accelerated stretching force of electrospinning jet favors the formation of all trans (TTTT) conformation of PVDF. Thus the synergetic effect of electrospinning and LDH facilitates the formation of highly polar β-phase content in PVDF. PVDF with high β-phase content exhibits a high binding affinity towards Li$^+$ ions and thus promotes the Li$^+$ ion access towards the vicinity of the electrode surface, which facilitates the overall battery performance (Kundu et al. 2017; Song et al. 2017).
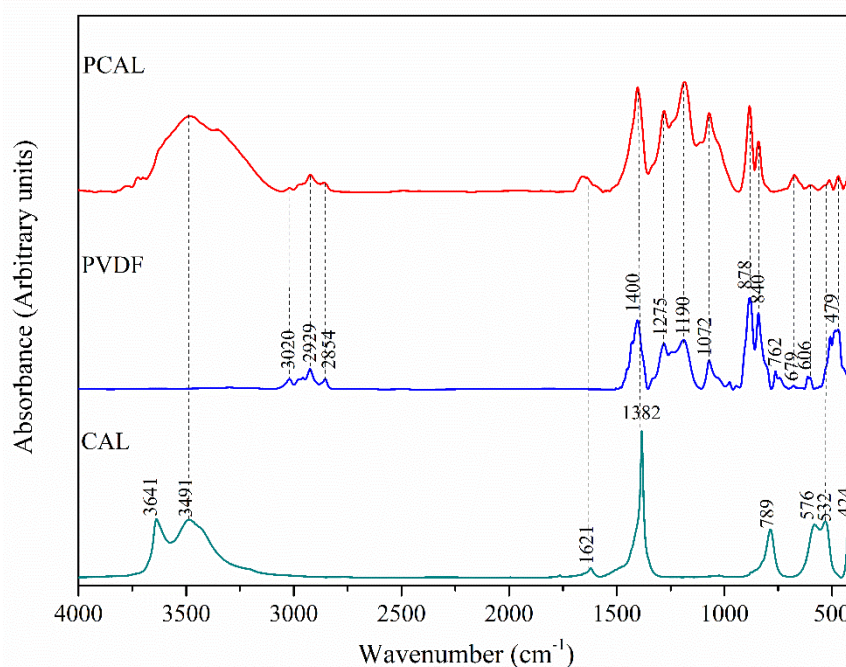
Fig. 6.2 FTIR spectra of CAL, PVDF, and PCAL nanofibers.

6.1.3. Morphological studies

The morphological studies of nanofibers were carried out using TEM, SEM, and AFM. Fig. 6.3 shows the TEM micrographs of CAL and PCAL nanofibers. The layered structure of CAL was confirmed from the TEM analysis. The orientation of CAL nanosheets along the fiber axis was observed from Fig. 6.3 (b). Fig. 6.4 (a-b) shows the SEM micrographs of PVDF and PCAL nanofibers. The average fiber diameter (AFD) decreased from 351 to 282 nm in PCAL compared to PVDF nanofibers. This is due to the high surface charge density induced by the addition of CAL, which further enhances the stretching and whipping process of electrospinning jet that leads to defect-free uniform fibers of smaller diameter. The SEM micrographs corresponding to activated GPE of PVDF and PCAL nanofibers are shown in Fig. 6.4 (c-d). A tremendous increment in AFD was observed in GPEs compared to that of nanofibers which is depicted as histograms in Fig. 6.4 (e-h). It was clearly observed that after electrolyte saturation the fibers became swollen and entangled, providing intimate contact with each other. The nanofibers exhibit swelling behavior due to their high permeability to electrolyte, and porosity (~81%) with a massively interconnected porous network structure. Moreover, the polar β-phase in PVDF provides good affinity to the polar electrolyte. Further, the topographical studies were carried out by AFM. 2-D and 3-D AFM images of interconnected PCAL nanofibers within a scanned area of 20×20 μm^2 are shown in Fig. 6.5. The AFM images of Celgard® 2400 and PVDF nanofibers are shown in Fig. 6.6.
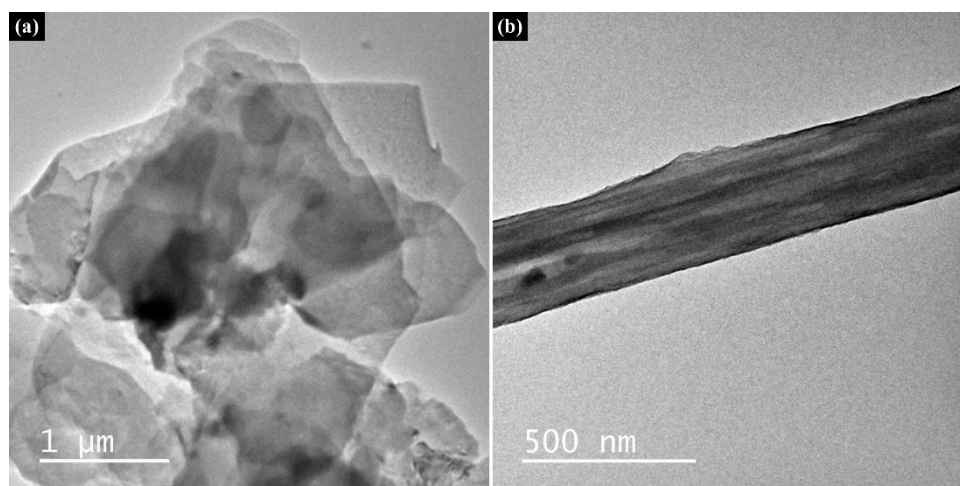
Fig. 6.3 TEM images of (a) CAL and (b) PCAL nanofibers.
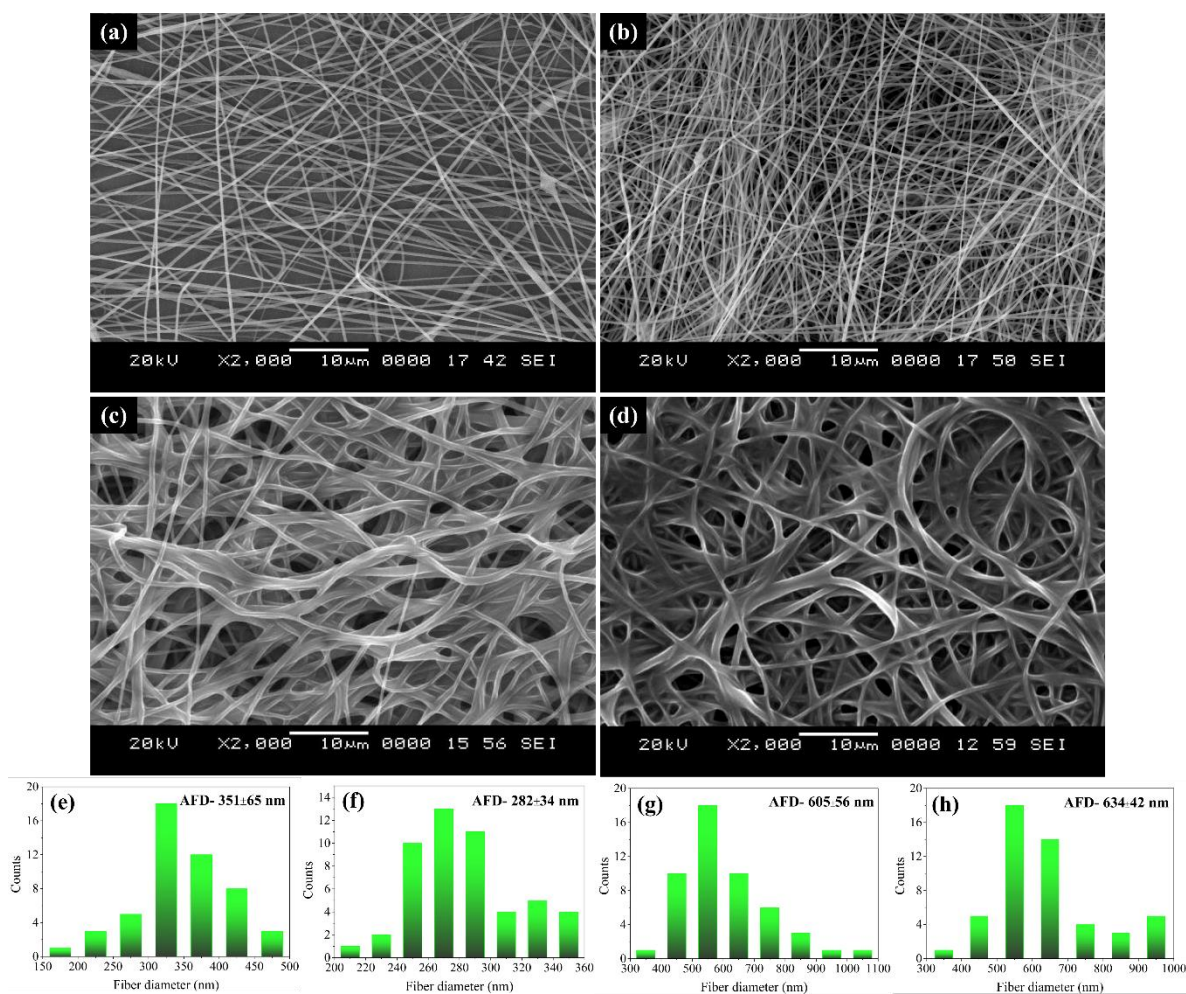
Fig. 6.4 SEM images of (a-b) PVDF and PCAL nanofibers and (c-d) GPE of PVDF and PCAL nanofibers after submerging in 1M LiPF$_6$ liquid electrolyte, (e-h) corresponding fiber diameter histogram.

The AFM image provides information regarding the microstructure and the surface roughness values of the nanofibers. The surface roughness values in terms of root mean square (RMS) roughness obtained for Celgard® 2400, PVDF, and PCAL nanofibers are 85, 350, and 209 nm, respectively. The Celgard membrane possesses low surface roughness value due to its smooth surface. The electrospun nanofibers exhibited higher surface roughness compared to Celgard® 2400, which ensures good adherence with electrolyte that leads to low interfacial resistance. The composite nanofibers exhibited less surface roughness compared to that of PVDF nanofibers. This can be attributed to the smaller pore size and the less number of pores present in

nanofibers (Jeddi et al. 2013). SEM and AFM studies give insight into the highly porous nature of nanofibers with smaller and uniformly distributed pores. This can further
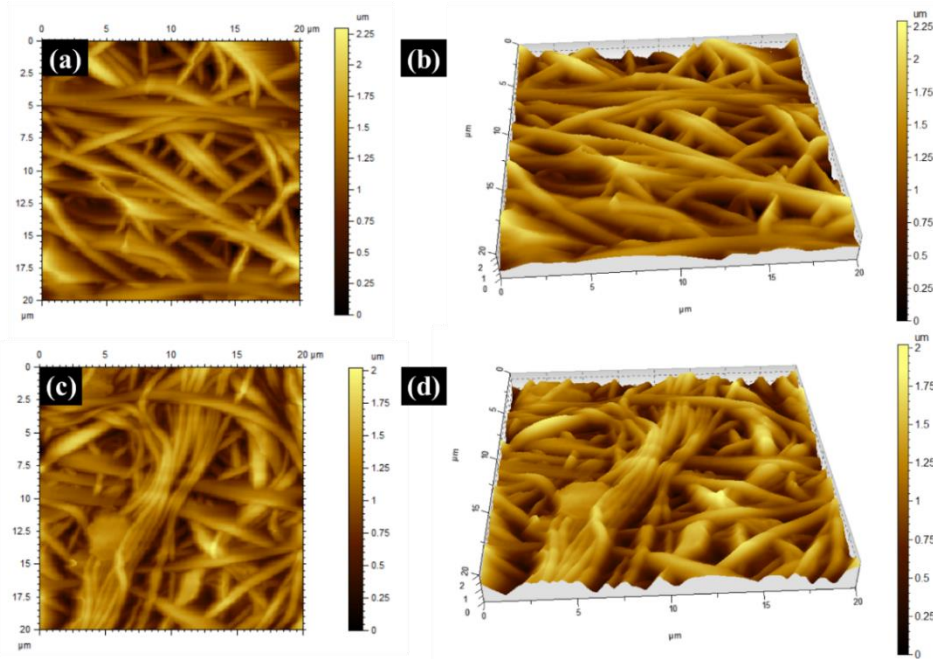
Fig. 6.5 (a) 2-D and (b) 3-D AFM images of PCAL nanofibers and (c) 2-D and (d) 3-D AFM images GPE of PCAL nanofibers after submerging in LiPF$_6$ liquid electrolyte.
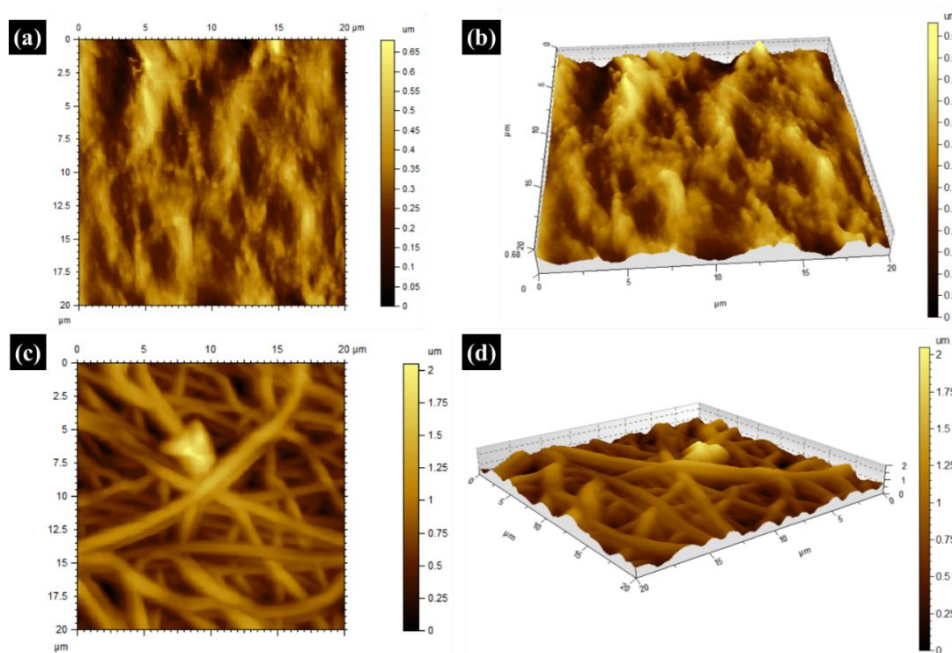
Fig. 6.6 (a) 2-D and (b) 3-D AFM images of Celgard® 2400 and (c) 2-D and (d) 3-D AFM images GPE of PVDF nanofibers after submerging in LiPF$_6$ liquid electrolyte.

improve the adhesion between the separator membrane and electrode, which leads to lower interfacial resistance (Fang et al. 2014).

6.1.4. Porosity measurements

The porosity measurements were carried out by n-butanol uptake method (Raja and Stephan 2014). In this method, the nanofiber membrane was immersed in n-butanol for 2 h, and the extra solvent was wiped out using tissue paper before the measurement. The porosity was calculated using the equation,

$$Porosity\ (\%) = \frac{M_B/\rho_B}{M_B/\rho_B + M_m/\rho_p} \times 100 \tag{6.2}$$

where, M_B and M_m are the mass of n-butanol absorbed membrane and dry membrane, respectively. ρ_B and ρ_p are the densities of n-butanol (0.810 g.cm^{-3}) and PVDF (1.78 g.cm^{-3}). The porosity values obtained for PVDF and PCAL nanofibers are 72 and 81% respectively. The porosity values of nanofibers are much higher than that of the commercial Celgard® 2400 membrane (41%). The high porosity of PCAL nanofibers will be beneficial for the electrolyte absorption and hence easy ion transport.

6.1.5. Liquid electrolyte uptake behavior and wettability studies

The liquid electrolyte uptake behavior was studied by soaking the nanofiber membrane in the LiPF$_6$ electrolyte for 2 h inside the glove box, and extra electrolyte was wiped using tissue paper prior to the measurement. The electrolyte uptake percentage was calculated by the equation,

$$Electrolyte\ uptake(\%) = \frac{M_w - M_d}{M_d} \times 100 \tag{6.3}$$

where, M_w and M_d are the mass of wet membrane and dry membrane, respectively. The PVDF nanofibers exhibited electrolyte uptake of 296% and, a tremendous increase in electrolyte uptake of 445% was observed in PCAL nanofibers. On the other hand, the commercial Celgard® 2400 membrane exhibited an electrolyte uptake of 70%, which is much less than that of the PVDF and PCAL nanofibers. The increased porosity observed in PVDF nanofibers after the inclusion of CAL nanosheets may help to hold enormous amount of liquid electrolyte in the nanofibers membrane.

The wettability of the separator membrane with liquid electrolyte plays an important role in battery performance since the absorption of electrolyte is required for ion transport in batteries. The wettability studies of nanofiber membranes were carried out using a dynamic contact angle analyzer. The PCAL nanofibers exhibited an excellent wettability towards the $LiPF_6$ electrolyte with a contact angle of 12.8°. PVDF and commercial Celgard® 2400 membranes exhibited a contact angle of 22.4 and 53.1°, respectively (Fig. 6.7). The improved wettability of the separator membrane with electrolyte facilitates lower internal resistance and enhancement in rate capability (Man et al. 2014). The lower contact angle value in PCAL nanofibers can be ascribed to the presence of hydrophilic groups present in the composite nanofibers and the superior capillary force exerted by the pores (Chen et al. 2014).
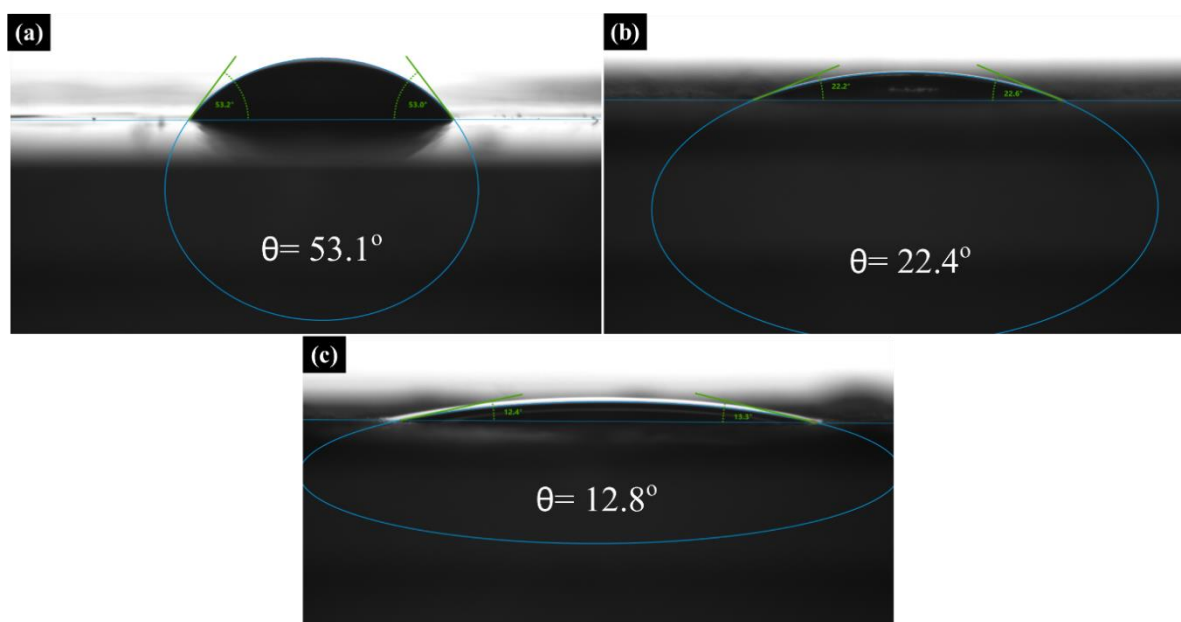
Fig. 6.7 Contact angle images of (a) Celgard® 2400 (b) PVDF and (c) PCAL membranes with 1 M $LiPF_6$ liquid electrolyte.

6.1.5. AC Ionic conductivity measurement

The ionic conductivity measurements were done by AC impedance spectroscopy with a frequency range of 42 Hz to 1 MHz and an AC amplitude of 10 mV. Fig. 6.8 shows the Nyquist plot of commercial Celgard® 2400, PVDF, and PCAL GPE. The disappearance of the semicircular portion was observed in the plot, which indicates that

ions are the current carriers, and thus, the total conductivity in GPE is the result of conduction by ions (Zhu et al. 2013). The ionic conductivity was calculated using the equation,

$$\sigma = \frac{t}{R \times A} \tag{6.4}$$

where, t is the thickness of the membrane, R is the bulk resistance measured from the intercept of the Nyquist plot with the real axis, and A is the electrode area. The PCAL nanofibers exhibited an ionic conductivity of 3.54×10^{-3} S.cm^{-1}, which is much higher than that of PVDF nanofibers (1.02×10^{-3} S.cm^{-1}) and commercial Celgard® 2400 separator (3.72×10^{-4} S.cm^{-1}). The increase in ionic conductivity can be attributed to the high electrolyte uptake due to the presence of a fully interconnected porous structure in nanofibers (Zhu et al. 2016).
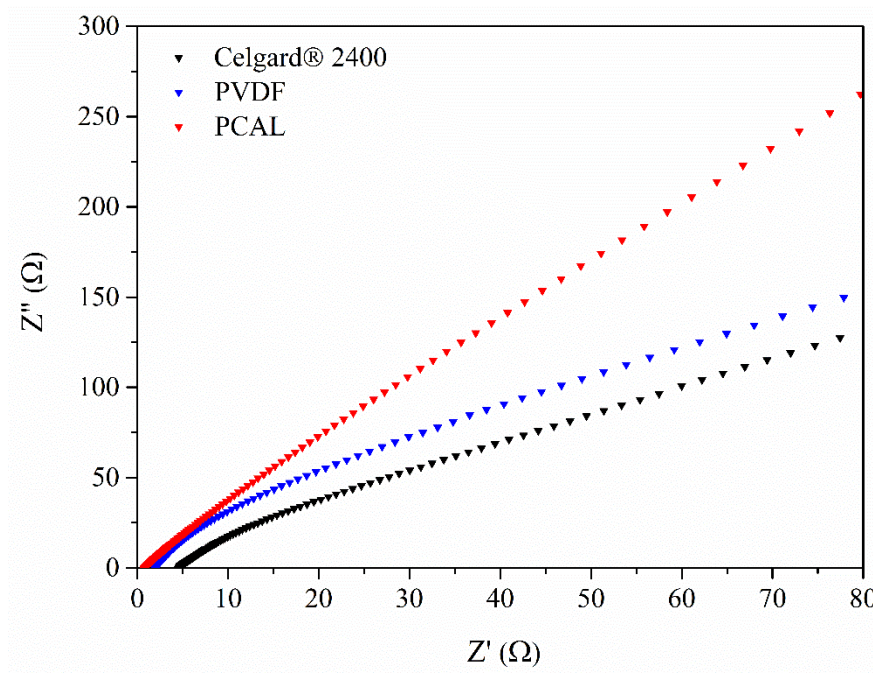
Fig. 6.8 Nyquist plot of Celgard® 2400, PVDF, and PCAL based GPEs.

In addition to this, the ion movements in separators were studied using the physical parameters such as MacMullin number (N_M) and tortuosity (τ). These parameters provide information regarding the deterioration of ionic conductivity of liquid electrolytes in the presence of separator membranes. The MacMullin number and tortuosity were calculated using the following equations,

$$N_M = \frac{\sigma_0}{\sigma_{eff}} \tag{6.5}$$

$$\tau = \sqrt{N_M \times P} \tag{6.6}$$

where, σ_0 and σ_{eff} are the ionic conductivities of the liquid electrolyte (8×10^{-3} S.cm^{-1}) and separator membrane soaked in liquid electrolyte and P is the porosity of the membrane (Kufian and Majid 2010; Patel et al. 2003; Xiang et al. 2007). The N_M and τ for Celgard® 2400, PVDF and PCAL separator membranes are presented in Table 6.1. The PCAL exhibited lower N_M than that of PVDF and Celgard® 2400 membrane indicating its lower deterioration on battery performance. The higher value of N_M for Celgard® 2400 membrane is due to its lower porosity. The τ value relates to the porous structure of separator to ionic conductivity. The relatively high ionic conductivity, low N_M and τ values of the PCAL separator membrane can be attributed to the high porosity with a fully interconnected porous network and good affinity of the separator to the electrolyte.

Table 6.1 The effective ionic conductivity, porosity, MacMullin number, and tortuosity values of separator membranes.

Porous Separator	σ_{eff} (S.cm^{-1})	P (%)	N_M	τ
Celgard® 2400	3.72×10^{-4}	41	21.51	2.97
PVDF	1.02×10^{-3}	72	7.84	2.38
PCAL	3.54×10^{-3}	81	2.26	1.35

6.1.6. Chronoamperometry and Linear sweep voltammetry studies

The lithium-ion transference number was obtained by chronoamperometry technique with a DC polarization method by biasing the system at 1.5 V. The GPE was loaded in between two SS blocking electrodes and the variation of current with time was measured. The chronoamperometric profile corresponding to PCAL GPE is shown in Fig. 6.9. The Ionic transference number is calculated by using the equation,

$$t_{ion} = \frac{I_t - I_e}{I_t} \tag{6.7}$$

where, I_t and I_e correspond to total current and electronic current, respectively. The transference number obtained is 0.98, and as the electric field applied, there was a sudden drop in current at the onset, which implies that the conduction in GPE is accomplished by ions (Perera and Vidanapathirana 2017). The large transference number in PCAL GPE can be attributed to the presence of polarity of PVDF and the presence of hydroxyl groups in the nanofibers. The presence of polarity in PVDF due to the *in situ* stretching by electrospinning and PVDF-filler interaction may hinder the movement of PF_6^- ions in $LiPF_6$ electrolyte that assist in Li^+ ion movement (Zhu et al. 2014). In addition to this, the hydroxyl groups present in the CAL layered crystals in PCAL nanofibers, that will form hydrogen bonds with fluorine atoms in PF_6^- anions (Fig. 6.10). This interaction hinders the movement of PF_6^- ions in the electrolyte system and subsequently favors the Li^+ ion transport in electrolyte. As a result, the Li^+ ion transference number and thus the ionic conductivity increases.
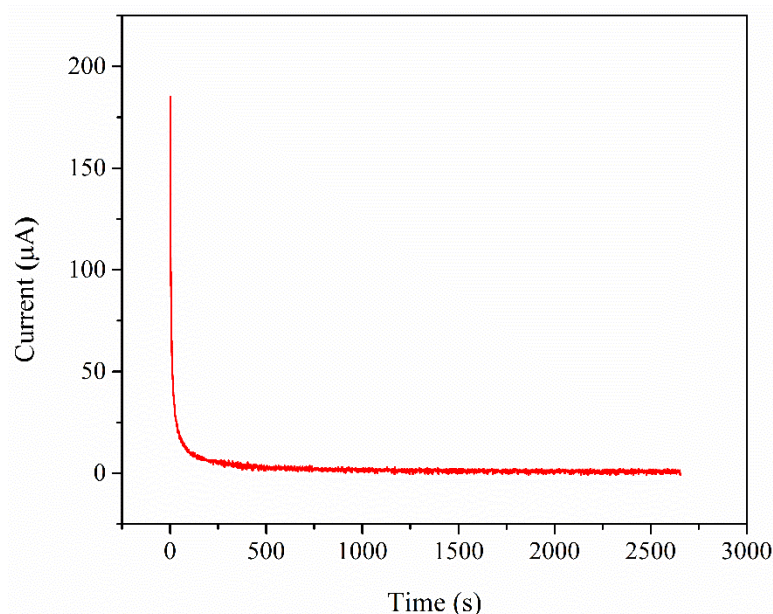
Fig. 6.9 Chronoamperometry profile for PCL based GPE at room temperature.

The electrochemical stability is an important parameter for LIB performance. The electrochemical stability window was obtained by a linear sweep voltammetric study of SS/GPE/Li system in the potential range of 1-5.5 V at a scan rate of 5 mV.s⁻¹. Here SS acts as a working electrode and Li metal acts as both the counter and reference electrode. The electrochemical stability window obtained for SS/GPE/Li system is
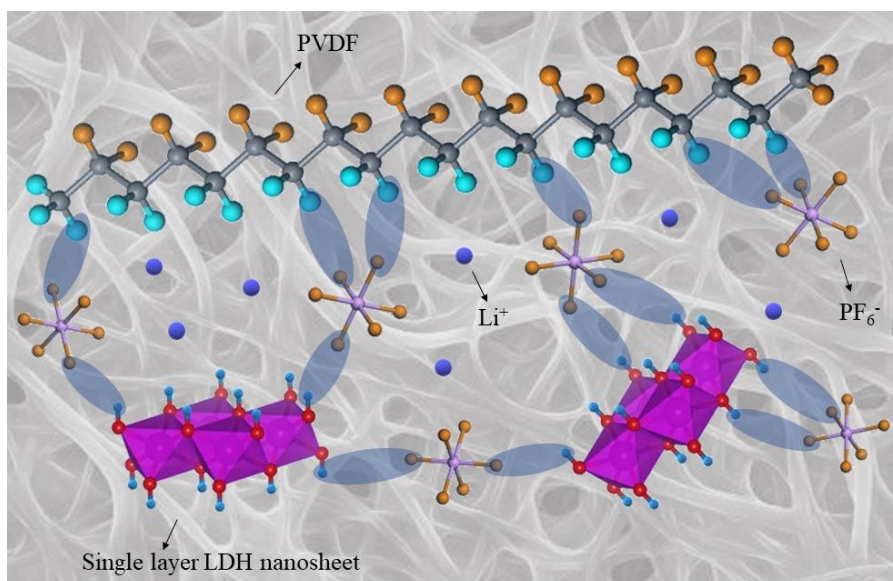
Fig. 6.10 Schematic representation of the interaction between nanofibers and LiPF$_6$ electrolyte.
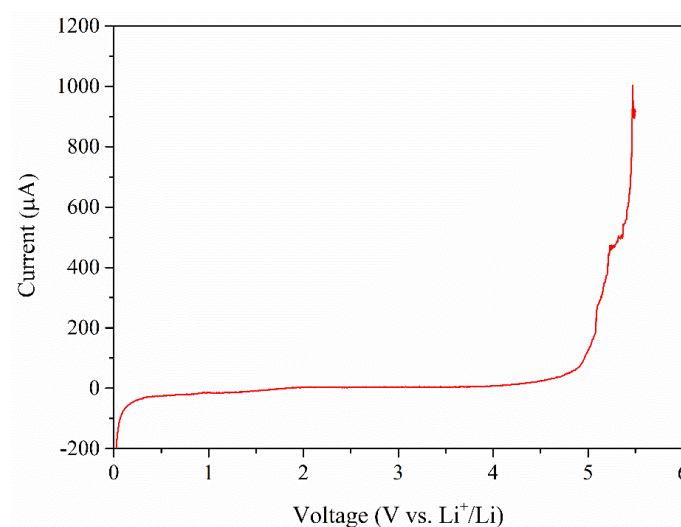
Fig. 6.11 Linear sweep voltammogram of PCAL based GPE at room temperature.

shown in Fig. 6.11. It is observed that PCAL GPE is stable up to ~5 V, which is in line with that of commercial LIBs. Up to 5 V, only a slight change in current was observed. Around 5 V there was a small increment in current and beyond this voltage, it started increasing. This is mainly due to the dissociation of the polymer electrolyte. The high electrochemical oxidation limit of PCAL GPE can be attributed to the high affinity of PCAL nanofibers to the electrolyte. The dipole-dipole interaction between CO groups in electrolyte and -CF$_2$- groups in PVDF contribute to the electrochemical stability of

PCAL GPE. In addition to this, the highly interconnected porous structure, high porosity, and unique morphological features of nanofibers help to improve the electrochemical stability of PCAL GPE.

6.1.7. Thermal shrinkage studies
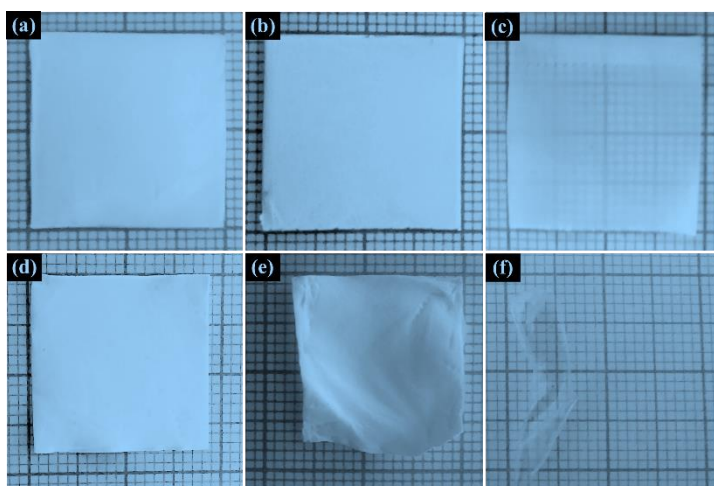
Fig. 6.12 Thermal shrinkage behavior of (a & d) PCAL, (b& e) PVDF, and (c& f) Celgard® 2400 separator membranes at room temperature and 160 °C for 1 h respectively.

The thermal stability of battery separator is one of the key parameters for the safety of battery. If the normal working temperature of a battery system is exceeded by the local temperature inside the battery, then there is a possibility of shrinkage of the separator membrane, which leads to the short circuit of electrodes (Writer 2019). Hence a careful study of thermal shrinkage has to be done for battery separators. In this work, the separator membranes (PCAL, PVDF, and Celgard® 2400) of dimension 2×2 cm^2 were heated at 160 °C for 1 h in a hot air oven. The thermal shrinkage ratio (TSR) was calculated by the equation,

$$TSR(\%) = \frac{S_0 - S}{S_0} \times 100 \tag{6.8}$$

where, S_0 and S denotes the area of separator before and after the thermal treatment. Fig. 6.12 shows the thermal shrinkage behavior of PCAL, PVDF, and Celgard® 2400 separator membranes at room temperature and 160 °C for 1 h respectively. PVDF and Celgard® 2400 membranes exhibited TSR of 26.75 and 76.25 %. In contrast, the PCAL

membrane exhibited a negligible TSR of 14.5% indicating the excellent dimensional stability of the membrane upon heating. This can be correlated to the high melting temperature exhibited by PCAL nanofibers (~174.6 °C) which is the superposition of melting temperatures corresponding to all the crystalline phases present in PCAL nanofibers, such as α and β. So the addition of CAL into PVDF improved the thermal dimensional stability of nanofibers, thereby making it a promising material for battery separator.

6.1.8. Mechanical properties
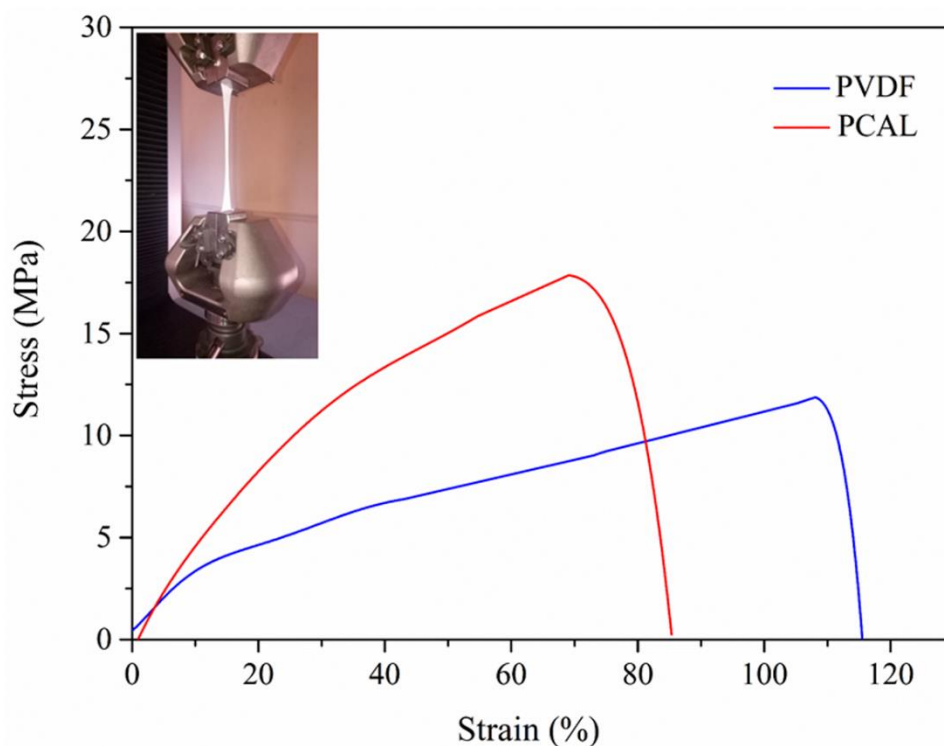
Fig. 6.13 Stress-strain curves of PVDF and PCAL nanofibers.

Mechanical property of separator membrane is a key parameter to withstand the tension during the winding of battery assembly. The stress-strain curves of PVDF and PCAL nanofibers are shown in Fig. 6.13. The PVDF and PCAL nanofibers exhibited a tensile strength of 11.86 and 17.84 MPa, respectively. A significant improvement in tensile strength was observed after the addition of CAL. The slight variation in elongation can be ascribed to the presence of CAL which will hinder the movement of the polymeric chain and lessen the elongation.

6.1.9. Charge-discharge performance of Li/GPE/LiCoO₂ cell
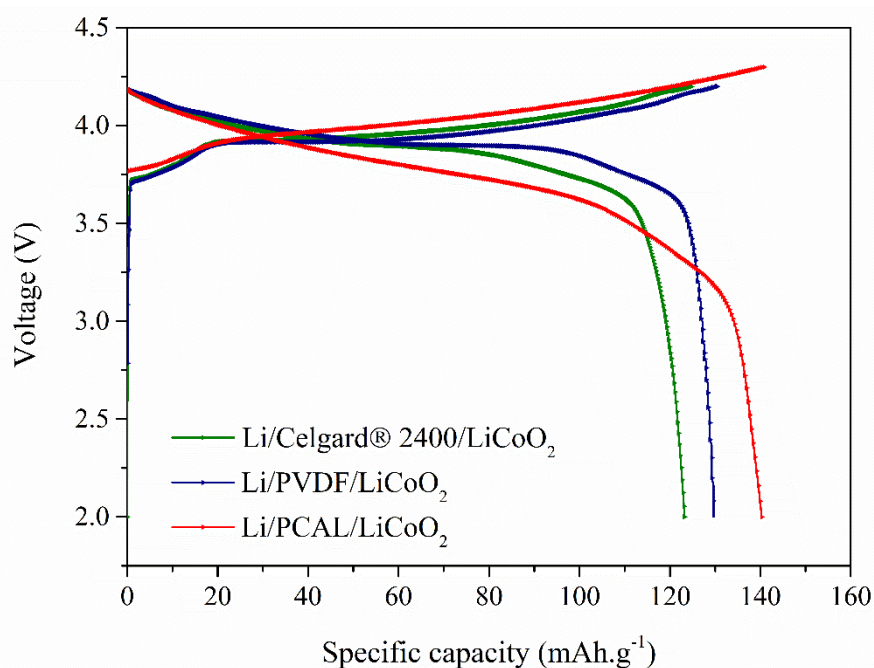
Fig. 6.14 Initial charge-discharge profile of Li/GPE/LiCoO₂ cells with Celgard® 2400, PVDF and PCAL based GPEs at a C-rate of 0.1C.

In order to study the cycle performance, CR2032 coin cell was used with LiCoO₂ as cathode and Li metal as reference and counter electrode. The Li/GPE/ LiCoO₂ coin cell assembly was subjected to a cut off voltage of 2 to 4.2 V at a C-rate of 0.1C. The initial charge-discharge profile of GPE based systems (PCAL, PVDF and Celgard® 2400) is shown in Fig. 6.14. The PCAL, PVDF, and Celgard® 2400 based GPE systems exhibited an initial discharge capacity of 140.31, 129.63, and 123.23 mAh.g^{-1} and charge capacity of 140.99, 130.38, and 124.87 mAh.g^{-1} respectively. The discharge capacity of PCAL based cell was much higher than that of the commercial Celgard® 2400 separator. Even though the discharge capacity of a battery is mostly reliant on the type of cathode material, the separator membrane also has a major contribution to it. The substantial wettability, ionic conductivity, electrolyte uptake, and porosity of the separator membrane can be the main reason for the significant discharge capacity of the cell. The cycling behavior, along with coulombic efficiency of Li/PCAL/LiCoO₂ cell are shown in Fig. 6.15. The remarkable result observed in PCAL based GPE is that the coulombic efficiency of the cell was retained as 99% even after 30 cycles. This can be

attributed to the high porosity and fully interconnected morphology of nanofibers. The difference between charge-discharge capacity is very less, which may be due to the high Li-ion transference number exhibited by PCAL nanofibers.
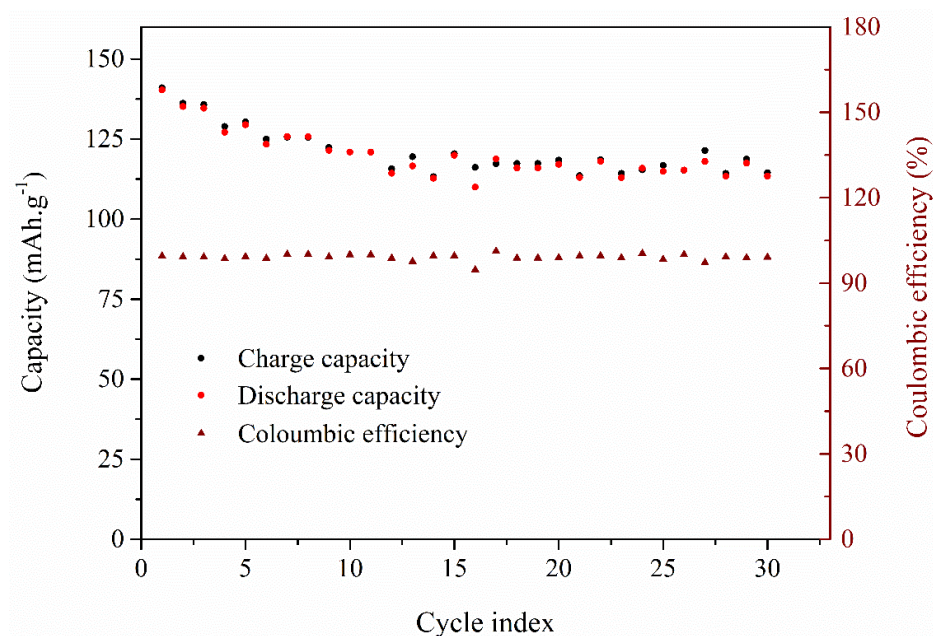
Fig. 6.15 Cycling profile along with coulombic efficiency of Li/PCAL/LiCoO$_2$ cell over 30 cycles at a C-rate of 0.1C.

To provide more insight into the cycling behavior of Li/GPE/ LiCoO$_2$ cell testing was carried out at different C-rates and is shown in Fig. 6.16. The Li/PCAL/ LiCoO$_2$ cell exhibited good cycling behavior compared to that of Celgard® 2400 and PVDF based GPEs. The Li/PCAL/ LiCoO$_2$ cell displayed the highest discharge capacities of 140.31, 130.66, 115.98, and 109.69 mAh.g^{-1} at C-rates of 0.1, 0.2, 0.5, and 1C respectively. However, a drop in discharge capacity at high C-rate was observed, which can be attributed to the influence of ohmic polarization (Jeong et al. 2010). At high C-rates the ohmic drop will be more significant. The stability of discharge capacity at high C-rate is due to the faster Li$^+$ ion movement towards the vicinity of electrode, facilitating the continuous supply of Li$^+$ ions. Moreover, the porous structure of PCAL based GPEs could be beneficial for high discharge capacity than that of commercial Celgard® 2400, and PVDF based GPEs.
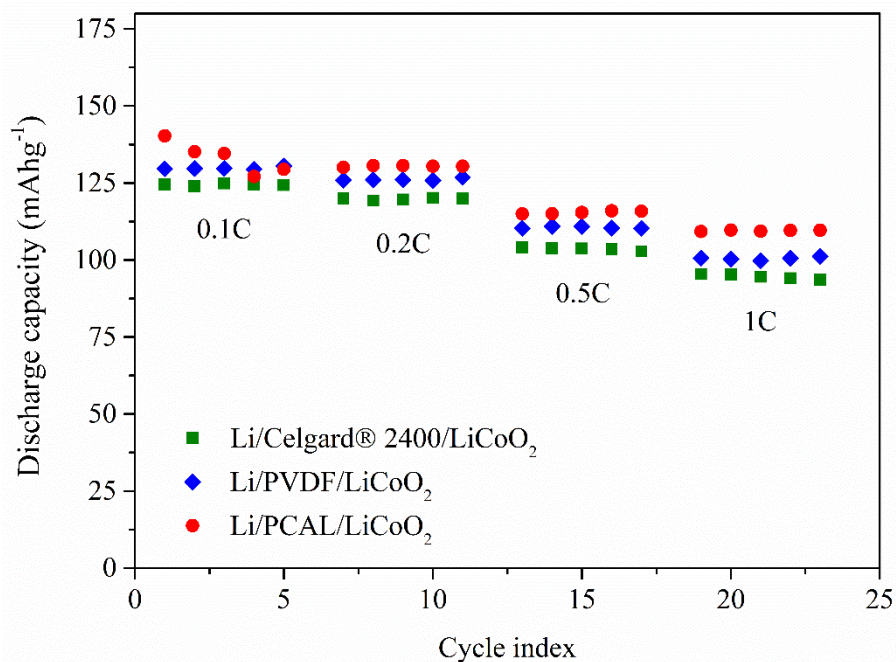
Fig. 6.16 Discharge capacities of Li/GPE/LiCoO$_2$ cells with Celgard® 2400, PVDF, and PCAL based GPEs at different C-rate.

6.2. SUMMARY AND CONCLUSIONS

Herein, an environment-friendly approach was introduced to synthesize CAL by the co-precipitation method and used as a filler material for PVDF nanofibers. The β-phase content increased to 82.79 % in PCAL compared to that of PVDF, which is mainly due to the PFDF-CAL interaction and *in situ* stretching due to electrospinning. The PCAL GPE showed excellent morphological features along with high porosity and electrolyte uptake. Moreover, there was a drastic increment in ionic conductivity, Li-ion transference number, and electrochemical stability, which is superior to that of PVDF and commercial Celgard® 2400 separators. This is mainly due to high electrolyte uptake due to the presence of a highly interconnected porous structure. Furthermore, Li/PCAL/LiCoO$_2$ cell exhibited exceptional initial discharge capacities compared to that of PVDF and commercial Celgard® 2400 based GPEs. Interestingly, the coulombic efficiency of the cell was retained as 99% even after 30 cycles. Overall this Li/PCAL/LiCoO$_2$ cell revealed the possibility to be used as a separator membrane for high-performance LIBs.

CHAPTER 7

CHAPTER 7

CONCLUSIONS

PART-I

The following conclusions are drawn from the results and discussions in the *chapters 3 and 4*.

The ZMO nanofibers with superior specific surface area and bifunctional water splitting electrocatalytic activity were successfully fabricated using sol-gel assisted electrospinning method followed by calcination. SAN was proven to be an efficient binder to acquire ZMO nanofibers with improved morphological features. It was observed that the AFD of the ceramic nanofibers decreased as a function of the calcination temperature, which is due to the crystallite growth as well as densification. Mesoporous nature of ZMO nanofibers was revealed by the results BET studies. The highest specific surface area of 79.51 $m^2.g^{-1}$ was obtained for the fibers calcined at 773 K and the surface area values of these nanofibers decrease when the calcination temperature was increased. A plausible mechanism of formation of tetragonal spinel ZMO nanofibers were proposed based on the results obtained from XRD and XPS studies. Moreover, the nanofibers exhibited good electrocatalytic performance towards water-splitting. The ZMO nanofibers calcined at 773 K exhibited the maximum electrocatalytic activity towards HER and nanofibers calcined at 993 K considered to be effective for OER.

PART-II

The following conclusions are drawn from the results and discussions in the *chapters 5 and 6*.

PCAL composite nanofibers were fabricated using electrospinning method. Here a new synthesis route was proposed for CAL. The structural, morphological and thermal properties of PCAL nanofibers were investigated using various characterization techniques. The AFD decreased upon the addition of CAL to PVDF whereas, the β phase increased compared to pristine PVDF. The drastic improvement in the β phase content was correlated with the co-operative effect of PVDF-filler

interaction and *in situ* stretching due to electrospinning. A plausible mechanism of interaction between LDH and PVDF in PCAL composite nanofibers were proposed. These nanofibers were explored in piezoelectric nanogenerator application using an in-house developed experimental set up. The nanofibers delivered a maximum output voltage of 4.1 and 5.72 V for hand slapping and frequency-dependent mechanical vibration mode. The composite nanofibers exhibited a high dielectric constant and low dielectric loss, promising its applications in electronic devices. Additionally, these nanofibers were employed in LIBs, as GPE. They have exhibited high ionic conductivity, Li-ion transference number, electrolyte uptake and improved charge-discharge profile compared to PVDF and commercial Celgard® 2400 separator.

SCOPE FOR FURTHER WORK

- A Comparative study can be done on the physico-chemical properties of sol-gel assisted electrospun ZMO nanofibers from SAN and other different polymeric binders.

- The performance of these nanofibers can be further improve by the doping of noble metals/rare earth elements.

- Applications of ZMO nanofibers can be explored in:

  - Sensors

  - Batteries as electrode material

  - Fuel cells as electrodes

- Piezoelectric coefficient of PCAL nanofibers can be studied.

- PCAL nanofibers can be explored in magnesium ion and sodium ion batteries, fuel cells, and filtration membranes.

APPENDIX-I

I.1. XRD pattern of precursor nanofiber

The XRD pattern correspond to SAN/ZnAc/MnAc precursor nanofiber is shown in Fig. I.1. The amorphous nature of precursor nanofabric is due to the presence of SAN. Traces of ZnAc and MnAc were also confirmed from the XRD pattern.
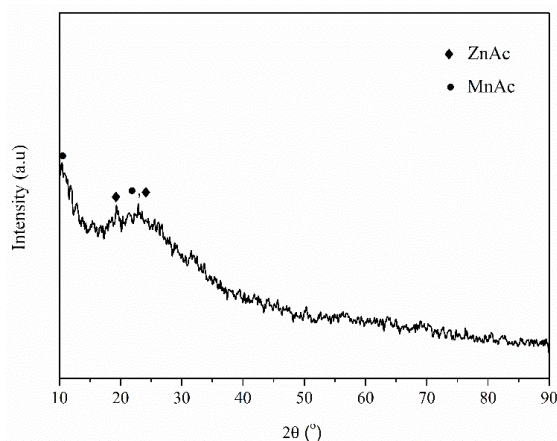
Fig. I.1 XRD pattern of precursor nanofiber.

I.2. Deconvoluted XRD patterns of ZMO nanofibers
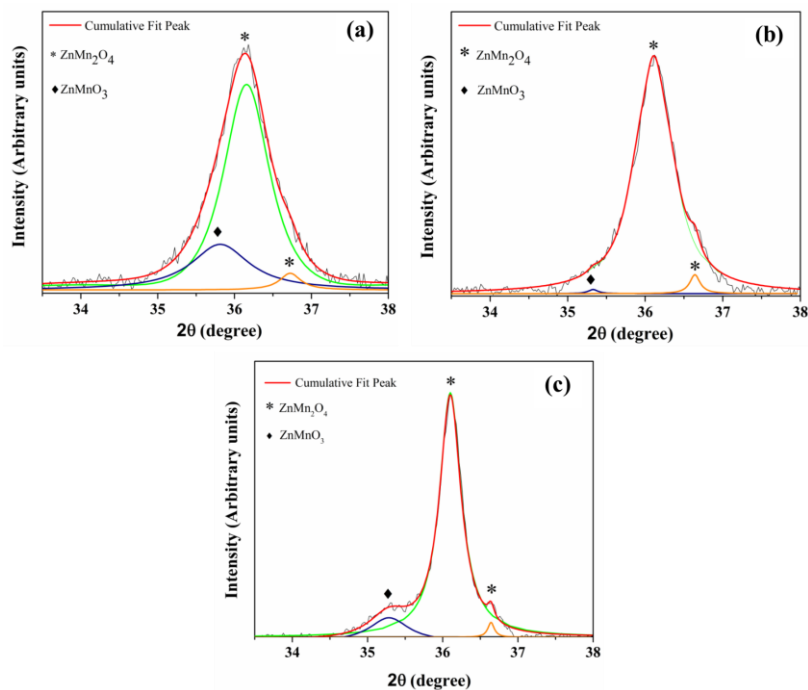
Fig. I.2 Deconvoluted XRD peak at (211) plane of ZMO nanofibers calcined at (a) 773 K (b) 873 K and (c) 973 K.

Fig. I.1 shows the deconvoluted peak at (211) plane of ZMO nanofibers calcined at (a) 773 K (b) 873 K and (c) 973 K respectively. It is inferred that this peak may well be due to the crystallization of $ZnMnO_3$ phase (indexed using ICDD card no. 28-1468 line diffraction pattern of hexagonal $ZnMnO_3$).

I.2. EDS Analysis

EDS results of ZMO nanofibers at different calcination temperature are shown in Table I.1. Theoretical values of mass and atomic percentage are compared with that of experiment values obtained. Fig. I.3 shows the EDS spectra of ZMO nanofibers calcined at 773 K. When the calcination temperature is 773 K the mass percent and atomic percentage values are close to theoretical value. The deviation increases as the calcination temperature is increased. So it is observed that the mass and atomic percent of elements increases with increase in calcination temperature.
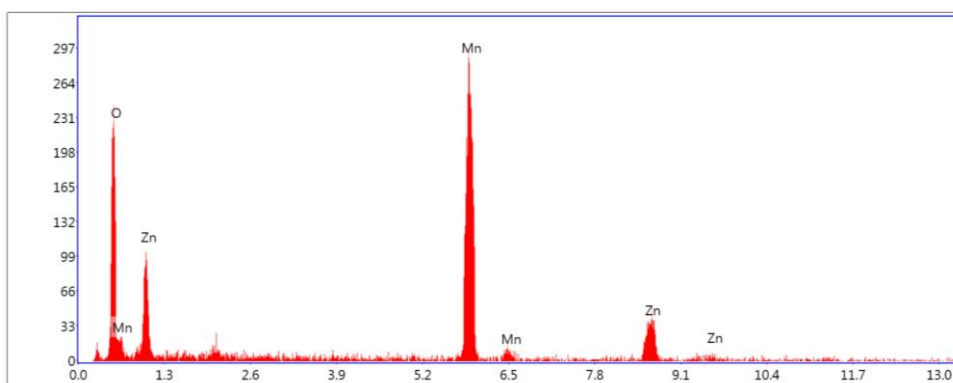
Fig. I.3 EDS spectra of $ZnMn_2O_4$ nanofibers obtained by calcination at 773 K

Table I.1 EDS results of ZMO nanofibers obtained at different calcination temperature.

Element	Mass percentage (%)				Atomic percentage (%)			
	ZMO-773	ZMO-873	ZMO-973	Theoretical	ZMO-773	ZMO-873	ZMO-973	Theoretical
Zn	23.09	36.68	40.24	27.33	11.99	20.10	22.66	14.29
Mn	49.98	38.98	36.90	45.92	30.88	25.42	24.73	28.57
O	26.93	24.34	22.87	26.75	57.14	54.48	52.61	57.14

I.3. Porosity analysis

Fig. I.4 shows the BJH pore size distribution curve of ZMO nanofibers obtained at different calcination temperatures.
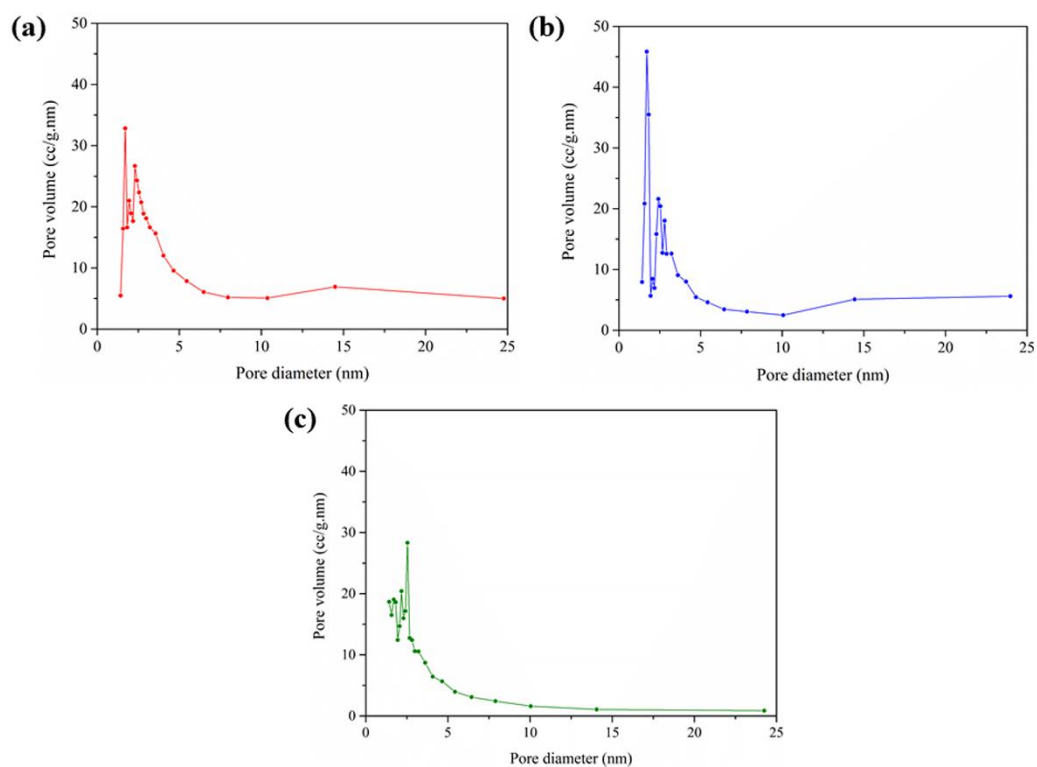
Fig. I.4 Pore size distribution curves correspond to (a) ZMO-773 (b) ZMO-873 and (c) ZMO-973.

I.4. HER and OER performance of Pt/C/GE and RuO₂/GE
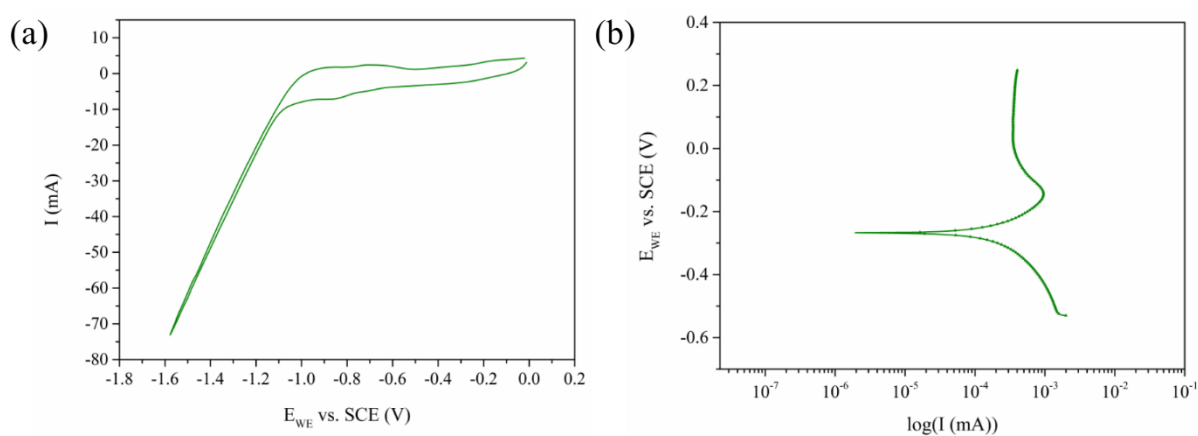
Fig. I.5 (a-b). CV curve and Tafel plot for HER of Pt/C/GE.
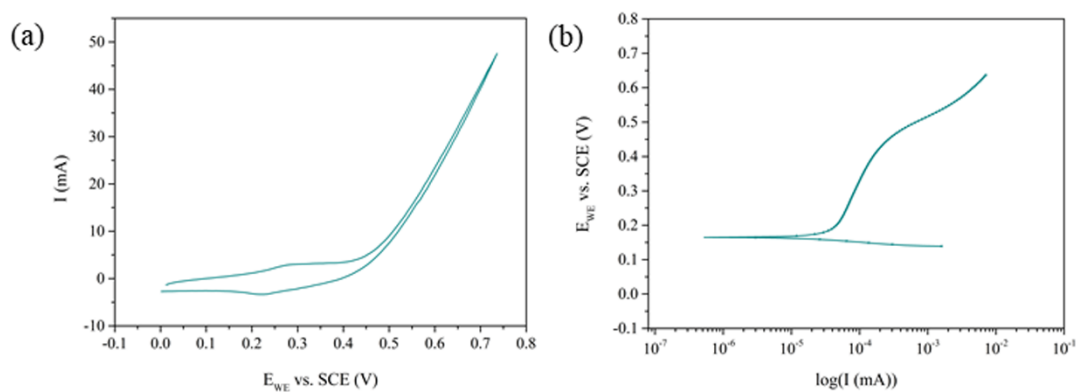
Fig. I.6 (a-b). CV curve and Tafel plot for OER of RuO$_2$/GE.

CV curve and Tafel plot corresponding to HER of Pt/C/GE are shown in Fig. I.4 (a-b). Pt/C/GE exhibited an onse potential of -0.935 V for HER. CV curve and Tafel plot corresponding to OER of RuO$_2$/GE are shown in Fig. I.6 (a-b). RuO$_2$/GE exhibited an onse potential of 0.405 V for OER.

II.1. XRD pattern of the precipitate formed amidst the experiment
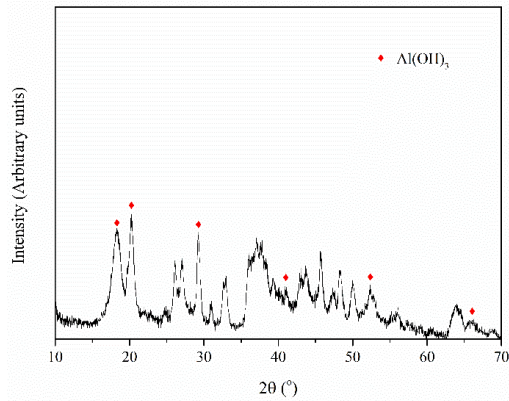
Fig. II.1 XRD pattern of the precipitate formed amidst the experiment.

The formation of $Al(OH)_3$ was confirmed by XRD analysis of partially reacted Al sheet, which was taken amidst the experiment.

II.2. Deconvolution of XRD patterns of PCAL nanofibers
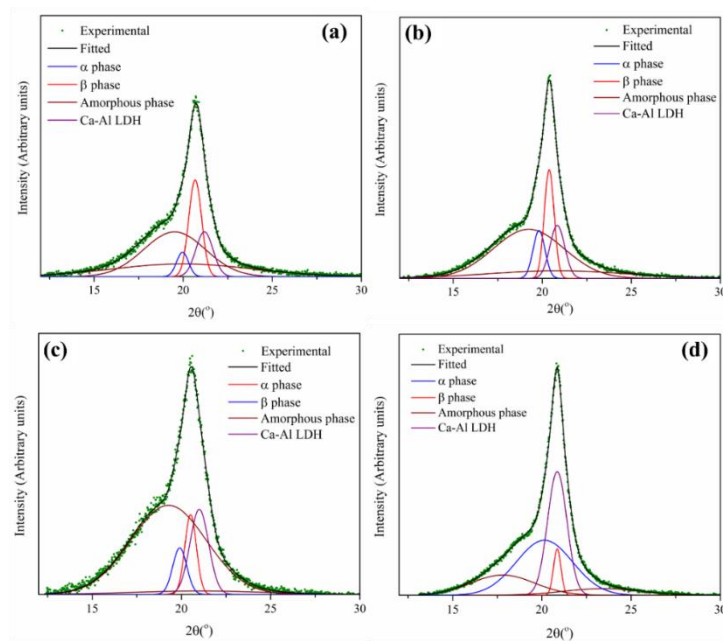
Fig. II.2 Deconvoluted XRD patterns of (a) PCAL-2.5 (b) PCAL-7.5 (c) PCAL-10 and (d) PCAL-12.5.

Table II.1 Comparison of various piezoelectric nanogenerators based on PVDF.[a]

Polymer/Nanofiller	Experimental Method	Output voltage (V)	Power density (μWcm^{-2})	Excitation mode	References
PVDF/Ag	Electrospinning	2	-	Mechanical vibration	(Issa et al. 2017)
PVDF/Fe-ZnO	Solution casting	2.4	1.17	Mechanical vibration	(Parangusa n et al. 2018)
PVDF/CuO	Spin coating	2.8	-	Mechanical compressive stress	(Xue et al. 2013)
PVDF/ZnO	Drop casting	1.81	0.21	Mechanical Hitting	(Singh et al. 2018)
PVDF/BaTiO$_3$	Electrospinning	0.48	-	Swinging limbs during Human walking	(Lee et al. 2016)
PVDF/BaTiO$_3$	3-D printing	4	-	Finger tapping	(Bodkhe et al. 2017)
PVDF/CNT	Electrospinning	3.7	-	Mechanical displacement	(Lu et al. 2017)
PVDF/Zn-Al LDH	Spin coating	4.9	-	Mechanical pressure	(Nguyen et al. 2018)
PVDF/Co-Al LDH	Spin coating	6.3	-	Mechanical pressure	(Tian et al. 2017)
PVDF/ZnO	Spin coating	0.4	-	Mechanical vibration	(Choi et al. 2017)

PVDF/Graphene	Electrospinning	0.064	-	Impact load	(Abbasipour et al. 2017)
PVDF/Halloysite nanotube	Electrospinning	0.1	-	Impact load	(Abbasipour et al. 2017)
PVDF/Ca-Al LDH	Electrospinning	4.1	0.2	Hand slapping	Present work
		5.72		Mechanical vibration	

[a] The comparison has been carried out irrespective of the nanogenerator size.

REFERENCES

Abouali, S., Akbari Garakani, M., Zhang, B., Xu, Z.-L., Kamali Heidari, E., Huang, J., Huang, J., and Kim, J.-K. (2015). "Electrospun Carbon Nanofibers with in Situ Encapsulated Co_3O_4 Nanoparticles as Electrodes for High-Performance Supercapacitors." *ACS Applied Materials & Interfaces*, 7(24), 13503–13511.

Abbasipour, M., Khajavi, R., Yousefi, A. A., Yazdanshenas, M. E., and Razaghian, F. (2017). "The piezoelectric response of electrospun PVDF nanofibers with graphene oxide, graphene, and halloysite nanofillers: a comparative study." *Journal of Materials Science: Materials in Electronics*, 28(21), 15942–15952.

Abdolmohammad-Zadeh, H., and Kohansal, S. (2012). "Determination of mesalamine by spectrofluorometry in human serum after solid-phase extraction with Ni-Al layered double hydroxide as a nanosorbent." *Journal of the Brazilian Chemical Society*, 23(3), 473–481.

Ahn, Y., Lim, J. Y., Hong, S. M., Lee, J., Ha, J., Choi, H. J., and Seo, Y. (2013). "Enhanced Piezoelectric Properties of Electrospun Poly(vinylidene fluoride)/Multiwalled Carbon Nanotube Composites Due to High β-Phase Formation in Poly(vinylidene fluoride)." *The Journal of Physical Chemistry C*, 117(22), 11791–11799.

Alghoraibi, I., and Alomari, S. (2018). "Different Methods for Nanofiber Design and Fabrication." *Handbook of Nanofibers*, Springer, Cham, 1–46.

Alonso, E., Hutter, C., Romero, M., Steinfeld, A., and Gonzalez-Aguilar, J. (2013). "Kinetics of Mn_2O_3–Mn_3O_4 and Mn_3O_4–MnO Redox Reactions Performed under Concentrated Thermal Radiative Flux." *Energy & Fuels*, 27(8), 4884–4890.

Aravindan, V., Suresh Kumar, P., Sundaramurthy, J., Ling, W. C., Ramakrishna, S., and Madhavi, S. (2013). "Electrospun NiO nanofibers as high performance anode material for Li-ion batteries." *Journal of Power Sources*, 227, 284–290.

Arora, A. K., Rajalakshmi, M., Ravindran, T. R., and Sivasubramanian, V. (2007).

"Raman spectroscopy of optical phonon confinement in nanostructured materials." *J. Raman Spectrosc.*, 38(6), 604–617.

Arvand, M., and Ghodsi, N. (2014). "Electrospun TiO$_2$ nanofiber/graphite oxide modified electrode for electrochemical detection of l-DOPA in human cerebrospinal fluid." *Sensors and Actuators, B: Chemical*, 204, 393–401.

Asokan, K., Park, J. Y., Choi, S. W., and Kim, S. S. (2010). "Nanocomposite ZnO-SnO$_2$ nanofibers synthesized by electrospinning method." *Nanoscale Research Letters*, 5(4), 747–752.

Azad, A. M. (2006). "Fabrication of transparent alumina (Al$_2$O$_3$) nanofibers by electrospinning." *Materials Science and Engineering A*, 435–436, 468–473.

Bessekhouad, Y., and Trari, M. (2002). "Photocatalytic hydrogen production from suspension of spinel powders AMn$_2$O$_4$(A=Cu and Zn)." *International Journal of Hydrogen Energy*, 27(4), 357–362.

Bhagwan, J., Kumar, N., Yadav, K. L., and Sharma, Y. (2018). "Probing the electrical properties and energy storage performance of electrospun ZnMn$_2$O$_4$ nanofibers." *Solid State Ionics*, 321, 75–82.

Bodkhe, S., Turcot, G., Gosselin, F. P., and Therriault, D. (2017). "One-Step Solvent Evaporation-Assisted 3D Printing of Piezoelectric PVDF Nanocomposite Structures." *ACS Applied Materials and Interfaces*, 9(24), 20833–20842.

Cai, X., Lei, T., Sun, D., and Lin, L. (2017). "A critical analysis of the α, β and γ phases in poly(vinylidene fluoride) using FTIR." *RSC Advances*, 7(25), 15382–15389.

Calleja, A., Sort, J., Ricart, S., Granados, X., Palmer, X., Vlad, V. R., Puig, T., and Obradors, X. (2016). "Composite films combining electrospun fiber network and epitaxial oxide by chemical solution deposition." *Journal of Sol-Gel Science and Technology*, 80(2), 277–284.

Cannavale, A., Fiorito, F., Manca, M., Tortorici, G., Cingolani, R., and Gigli, G. (2010). "Multifunctional bioinspired sol-gel coatings for architectural glasses." *Building and*

Environment, 45(5), 1233–1243.

Cao, Y., Zou, X., Wang, X., Qian, J., Bai, N., and Li, G. D. (2016). "Effective detection of trace amount of explosive nitro-compounds by ZnO nanofibers with hollow structure." *Sensors and Actuators, B: Chemical*, 232, 564–570.

Chakraborty, M., Mitra, M. K., and Chakraborty, J. (2017). "One-pot synthesis of CaAl-layered double hydroxide–methotrexate nanohybrid for anticancer application." *Bulletin of Materials Science*, 40(6), 1203–1211.

Chen, J., Wang, S., Ding, L., Jiang, Y., and Wang, H. (2014). "Performance of through-hole anodic aluminum oxide membrane as a separator for lithium-ion battery." *Journal of Membrane Science*, 461, 22–27.

Chen, Z., Li, H., Xie, G., and Yang, K. (2018). "Core–shell structured Ag@C nanocables for flexible ferroelectric polymer nanodielectric materials with low percolation threshold and excellent dielectric properties." *RSC Advances*, 8(1), 1–9.

Choi, M., Murillo, G., Hwang, S., Kim, J. W., Jung, J. H., Chen, C.-Y., and Lee, M. (2017). "Mechanical and electrical characterization of PVDF-ZnO hybrid structure for application to nanogenerator." *Nano Energy*, 33, 462–468.

Choquette, Y., Brossard, L., Lasia, A., and Menard, H. (2016). "Study of the Kinetics of Hydrogen Evolution Reaction on Raney Nickel Composite-Coated Electrode by AC Impedance Technique." *ChemInform*, 21(34), 4–11.

Chuangchote, S., Jitputti, J., Sagawa, T., and Yoshikawa, S. (2009). "Photocatalytic Activity for Hydrogen Evolution of Electrospun TiO_2 Nanofibers." *ACS Applied Materials & Interfaces*, 1(5), 1140–1143.

Cooley, J. F. (1902). "Apparatus for electrically dispersing fluids." *US Patent 692,631*, 693(631), 1–6.

Courtel, F. M., Abu-Lebdeh, Y., and Davidson, I. J. (2012). "$ZnMn_2O_4$ nanoparticles synthesized by a hydrothermal method as an anode material for Li-ion batteries." *Electrochimica Acta*, 71, 123–127.

De Sá, F. P., Cunha, B. N., and Nunes, L. M. (2013). "Effect of pH on the adsorption of Sunset Yellow FCF food dye into a layered double hydroxide (CaAl-LDH-NO$_3$)." *Chemical Engineering Journal*, 215–216, 122–127.

Dharmaraj, N., Park, H. C., Lee, B. M., Viswanathamurthi, P., Kim, H. Y., and Lee, D. R. (2004). "Preparation and morphology of magnesium titanate nanofibres via electrospinning." *Inorganic Chemistry Communications*, 7(3), 431–433.

Doh, S. J., Kim, C., Lee, S. G., Lee, S. J., and Kim, H. (2008). "Development of photocatalytic TiO 2 nanofibers by electrospinning and its application to degradation of dye pollutants." *Journal of Hazardous Materials*, 154(1–3), 118–127.

Driessens, F. C. M., and Rieck, G. D. (1966). "Phase equilibria in the system ZnMnO in air." *Journal of Inorganic and Nuclear Chemistry*, 28(8), 1593–1600.

Dutta, K., and Pramanik, A. (2013). "Synthesis of a novel cone-shaped CaAl-layered double hydroxide (LDH): Its potential use as a reversible oil sorbent." *Chemical Communications*, 49(57), 6427–6429.

Elias, L., and Hegde, A. C. (2016). "Synthesis and characterization of Ni-P-Ag composite coating as efficient electrocatalyst for alkaline hydrogen evolution reaction." *Electrochimica Acta*, 219, 377–385.

Esfahani, H., Jose, R., and Ramakrishna, S. (2017). "Electrospun ceramic nanofiber mats today: Synthesis, properties, and applications." *Materials*, 10(11), 1238.

Fan, F. R., Tang, W., and Wang, Z. L. (2016). *Flexible Nanogenerators for Energy Harvesting and Self-Powered Electronics*. *Advanced Materials*, 4283–4305.

Fang, L.-F. F., Shi, J.-L. L., Li, H., Zhu, B.-K. K., and Zhu, L.-P. P. (2014). "Construction of porous PVDF coating layer and electrochemical performances of the corresponding modified polyethylene separators for lithium ion batteries." *Journal of Applied Polymer Science*, 131(21), 1–9.

Feynman, R. P. (1992). "There's plenty of room at the bottom (transcript of a talk from 1959)." *Journal of Microelectromechanical Systems*, 1(1), 60–66.

Formhals, A. (1944, May 30). "Method and apparatus for spinning." US patent, US2349950 A. http://www.google.com/patents/US2349950 .

Fu, R., Chen, S., Lin, Y., Zhang, S., Jiang, J., Li, Q., and Gu, Y. (2017). "Improved piezoelectric properties of electrospun poly(vinylidene fluoride) fibers blended with cellulose nanocrystals." *Materials Letters*, 187(September 2016), 86–88.

George, G., and Anandhan, S. (2014). "Electrospun nickel oxide nanofiber webs for thermistor applications." *International Journal of Plastics Technology*, 18(3), 374–382.

George, G., and Anandhan, S. (2015). "A comparative study on the physico–chemical properties of sol–gel electrospun cobalt oxide nanofibres from two different polymeric binders." *RSC Advances*, 5(99), 81429–81437.

George, G., Elias, L., Hegde, A. C., and Anandhan, S. (2015). "Morphological and structural characterisation of sol-gel electrospun Co_3O_4 nanofibres and their electro-catalytic behaviour." *RSC Advances*, 5(51), 40940–40949.

Ghashghaie, S., Bazargan, A. M., Ganji, M. E., Marzbanrad, E., Zamani, C., Raissi, B., Keyanpour-Rad, M., and Bahrevar, M. A. (2011). "An investigation on the behavior of electrospun ZnO nanofibers under the application of low frequency AC electric fields." *Journal of Materials Science: Materials in Electronics*, 22(9), 1303–1307.

Goriparti, S., Miele, E., De Angelis, F., Di Fabrizio, E., Proietti Zaccaria, R., and Capiglia, C. (2014). "Review on recent progress of nanostructured anode materials for Li-ion batteries." *Journal of Power Sources*, 257, 421–443.

Gregorio, R., and Cestari, M. (1994). "Effect of crystallization temperature on the crystalline phase content and morphology of poly(vinylidene fluoride)." *Journal of Polymer Science Part B: Polymer Physics*, 32(5), 859–870.

Gu, S. Y., Ren, J., and Wu, Q. L. (2005). "Preparation and structures of electrospun PAN nanofibers as a precursor of carbon nanofibers." *Synthetic Metals*, 155(1), 157–161.

Guan, H., Shao, C., Wen, S., Chen, B., Gong, J., and Yang, X. (2003). "Preparation and

characterization of NiO nanofibres via an electrospinning technique." *Inorganic Chemistry Communications*, 6(10), 1302–1303.

Guan, Y., Feng, Y., Mu, Y., Fang, L., Zhang, H., and Wang, Y. (2016). "Ultra-tiny ZnMn2O4 nanoparticles encapsulated in sandwich-like carbon nanosheets for high-performance supercapacitors." *Nanotechnology*, 27(47).

Guillemet-Fritsch, S., Chanel, C., Sarrias, J., Bayonne, S., Rousset, A., Alcobe, X., and Sarriòn, M. L. M. (2000). "Structure, thermal stability and electrical properties of zinc manganites." *Solid State Ionics*, 128(1–4), 233–242.

Haider, A., Haider, S., and Kang, I.-K. (2018). "A comprehensive review summarizing the effect of electrospinning parameters and potential applications of nanofibers in biomedical and biotechnology." *Arabian Journal of Chemistry*, 11(8), 1165–1188.

Han, S. O., Youk, J. H., Min, K. D., Kang, Y. O., and Park, W. H. (2008). "Electrospinning of cellulose acetate nanofibers using a mixed solvent of acetic acid/water: Effects of solvent composition on the fiber diameter." *Materials Letters*, 62(4–5), 759–762.

Ilahi, N. A., Suryana, R., Nurrosyid, F., and Linda Kusuma, N. T. (2017). "Electrospinning Titanium Dioxide (TiO2) nanofiber for dye sensitized solar cells based on Bryophyta as a sensitizer." *Journal of Physics: Conference Series*, 795, 012033.

Issa, A., Al-Maadeed, M., Luyt, A., Ponnamma, D., and Hassan, M. (2017). "Physico-Mechanical, Dielectric, and Piezoelectric Properties of PVDF Electrospun Mats Containing Silver Nanoparticles." *C- Journal of carbon research*, 3(4), 30.

ISO. (2015). *Technical Specification 80004-1:2015 - Nanotechnologies – Vocabulary – Part 1: Nano-objects*, ISO, Geneva.

ISO. (2015). *Technical Specification 80004-2:2015 - Nanotechnologies – Vocabulary – Part 2: Nano-objects*, ISO, Geneva.

Itoh, H., Li, Y., Chan, K. H. K., and Kotaki, M. (2016). "Morphology and mechanical

properties of PVA nanofibers spun by free surface electrospinning." *Polymer Bulletin*, 73(10), 2761–2777.

Jahan, N., Mighri, F., Rodrigue, D., and Ajji, A. (2017). "Enhanced electroactive β phase in three phase PVDF/CaCO₃ /nanoclay composites: Effect of micro-CaCO₃ and uniaxial stretching." *Journal of Applied Polymer Science*, 134(24).

Jeddi, K., Zhao, Y., Zhang, Y., Konarov, A., and Chen, P. (2013). "Fabrication and Characterization of an Effective Polymer Nanocomposite Electrolyte Membrane for High Performance Lithium/Sulfur Batteries." *Journal of The Electrochemical Society*, 160(8), A1052–A1060.

Jeong, H. S., Hong, S. C., and Lee, S. Y. (2010). "Effect of microporous structure on thermal shrinkage and electrochemical performance of Al₂O₃/poly(vinylidene fluoride-hexafluoropropylene) composite separators for lithium-ion batteries." *Journal of Membrane Science*, 364(1–2), 177–182.

Jiang, Y., Wang, W., Jing, C., Cao, C., and Chu, J. (2011). "Sol-gel synthesis, structure and magnetic properties of Mn-doped ZnO diluted magnetic semiconductors." *Materials Science and Engineering B: Solid-State Materials for Advanced Technology*, 176(16), 1301–1306.

Jing, C., Jiang, Y., Bai, W., Chu, J., and Liu, A. (2010). "Synthesis of Mn-doped ZnO diluted magnetic semiconductors in the presence of ethyl acetoacetate under solvothermal conditions." *Journal of Magnetism and Magnetic Materials*, 322(16), 2395–2400.

Joseph, D. P., and Venkateswaran, C. (2011). "Bandgap Engineering in ZnO By Doping with 3d Transition Metal Ions." *Journal of Atomic and Molecular Physics*, 2011, 11.

Kalluri, S. (2016). "Nano-engineering and advanced characterizations of layered-structure electrode materials for lithium-ion and sodium-ion batteries." Doctor of Philosophy thesis, University of Wollongong, Australia.

Karan, S. K., Das, A. K., Bera, R., Paria, S., Maitra, A., Shrivastava, N. K., and Khatua,

B. B. (2016). "Effect of γ-PVDF on enhanced thermal conductivity and dielectric property of Fe-rGO incorporated PVDF based flexible nanocomposite film for efficient thermal management and energy storage applications." *RSC Advances*, 6(44), 37773–37783.

Khalifa, M., Mahendran, A., and Anandhan, S. (2016). "Probing the synergism of halloysite nanotubes and electrospinning on crystallinity, polymorphism and piezoelectric performance of poly(vinylidene fluoride)." *RSC Advances*, 6(115), 114052–114060.

Khalifa, M., Janakiraman, S., Ghosh, S., Venimadhav, A., and Anandhan, S. (2019a). "PVDF/halloysite nanocomposite-based non-wovens as gel polymer electrolyte for high safety lithium ion battery." *Polymer Composites*, 40(6), 2320–2334.

Khalifa, M., Mahendran, A., and Anandhan, S. (2019b). "Synergism of graphitic-carbon nitride and electrospinning on the physico-chemical characteristics and piezoelectric properties of flexible poly(vinylidene fluoride) based nanogenerator." *Journal of Polymer Research*, 26(3).

Kim, D.-C., and Ihm, S.-K. (2001). "Application of Spinel-Type Cobalt Chromite as a Novel Catalyst for Combustion of Chlorinated Organic Pollutants." *Environmental Science & Technology*, 35(1), 222–226.

Kim, J. G., Lee, S. H., Kim, Y., and Kim, W. B. (2013). "Fabrication of Free-Standing $ZnMn_2O_4$ Mesoscale Tubular Arrays for Lithium-Ion Anodes with Highly Reversible Lithium Storage Properties." *ACS Applied Materials & Interfaces*, 5(21), 11321–11328.

Kim, J. H., Yoo, S. J., Kwak, D. H., Jung, H. J., Kim, T. Y., Park, K. H., and Lee, J. W. (2014). "Characterization and application of electrospun alumina nanofibers." *Nanoscale Research Letters*, 9(1), 1–6.

Kim, S. W., Lee, H. W., Muralidharan, P., Seo, D. H., Yoon, W. S., Kim, D. K., and Kang, K. (2011). "Electrochemical performance and ex situ analysis of $ZnMn_2O_4$ nanowires as anode materials for lithium rechargeable batteries." *Nano Research*, 4(5),

505–510.

Kufian, M. Z., and Majid, S. R. (2010). "Performance of lithium-ion cells using 1 M $LiPF_6$ in EC/DEC (v/v = 1/2) electrolyte with ethyl propionate additive." *Ionics*, 16(5), 409–416.

Kumar, B. S., Gudla, V. C., Ambat, R., Kalpathy, S. K., and Anandhan, S. (2019). "Graphene nanoclusters embedded nickel cobaltite nanofibers as multifunctional electrocatalyst for glucose sensing and water-splitting applications." *Ceramics International*, 45(18), 25078–25091.

Kumar, B. S., Shanmugharaj, A. M., Kalpathy, S. K., and Anandhan, S. (2017). "Some new observations on the structural and phase evolution of nickel titanate nanofibers." *Ceramics International*, 43(9), 6845–6857.

Kundu, M., Costa, C. M., Dias, J., Maceiras, A., Vilas, J. L., and Lanceros-Méndez, S. (2017). "On the Relevance of the Polar β-Phase of Poly(vinylidene fluoride) for High Performance Lithium-Ion Battery Separators." *Journal of Physical Chemistry C*, 121(47), 26216–26225.

Lee, C., Wood, D., Edmondson, D., Yao, D., Erickson, A. E., Tsao, C. T., Revia, R. A., Kim, H., and Zhang, M. (2016). "Electrospun uniaxially-aligned composite nanofibers as highly-efficient piezoelectric material." *Ceramics International*, 42(2), 2734–2740.

Lee, D. U., Kim, B. J., and Chen, Z. (2013). "One-pot synthesis of a mesoporous $NiCo_2O_4$ nanoplatelet and graphene hybrid and its oxygen reduction and evolution activities as an efficient bi-functional electrocatalyst." *Journal of Materials Chemistry A*, 1(15), 4754.

Li, B., Zhang, B., Nie, S., Shao, L., and Hu, L. (2017). "Optimization of plasmon-induced photocatalysis in electrospun Au/CeO_2 hybrid nanofibers for selective oxidation of benzyl alcohol." *Journal of Catalysis*, 348, 256–264.

Li, C., Chen, R., Zhang, X., Shu, S., Xiong, J., Zheng, Y., and Dong, W. (2011). "Electrospinning of CeO_2-ZnO composite nanofibers and their photocatalytic

property." *Materials Letters*, 65(9), 1327–1330.

Li, D., Herricks, T., and Xia, Y. (2003). "Magnetic nanofibers of nickel ferrite prepared by electrospinning." *Applied Physics Letters*, 83(22), 4586–4588.

Li, S. R., Sun, Y., Ge, S. Y., Qiao, Y., Chen, Y. M., Lieberwirth, I., Yu, Y., and Chen, C. H. (2012). "A facile route to synthesize nano-MnO/C composites and their application in lithium ion batteries." *Chemical Engineering Journal*, 192, 226–231.

Li, X., Hao, X., Abudula, A., and Guan, G. (2016). "Nanostructured catalysts for electrochemical water splitting: current state and prospects." *Journal of Materials Chemistry A*, 4(31), 11973–12000.

Li, Y., Porwal, H., Huang, Z., Zhang, H., Bilotti, E., and Peijs, T. (2016). "Enhanced Thermal and Electrical Properties of Polystyrene-Graphene Nanofibers via Electrospinning." *Journal of Nanomaterials*, 2016, 1–8.

Lobo, L. S., and Kumar, A. R. (2016). "Investigation of structural and electrical properties of $ZnMn_2O_4$ synthesized by sol–gel method." *J Mater Sci: Mater Electron*, 27(7), 7398–7406.

Lu, B., Cao, D., Wang, P., Wang, G., and Gao, Y. (2011). "Oxygen evolution reaction on Ni-substituted Co_3O_4 nanowire array electrodes." *International Journal of Hydrogen Energy*, 36(1), 72–78.

Luo, L., Qiao, H., Chen, K., Fei, Y., and Wei, Q. (2015). "Fabrication of electrospun ZnMn2O4 nanofibers as anode material for lithium-ion batteries." *Electrochimica Acta*, 177, 283–289.

Lu, X., Qu, H., and Skorobogatiy, M. (2017). "Piezoelectric Micro- and Nanostructured Fibers Fabricated from Thermoplastic Nanocomposites Using a Fiber Drawing Technique: Comparative Study and Potential Applications." *ACS Nano*, 11(2), 2103–2114.

Ma, J., Zhang, Q., Mayo, A., Ni, Z., Yi, H., Chen, Y., Mu, R., Bellan, L. M., and Li, D. (2015). "Thermal conductivity of electrospun polyethylene nanofibers." *Nanoscale*,

7(40), 16899–16908.

Maensiri, S., and Nuansing, W. (2006). "Thermoelectric oxide $NaCo_2O_4$ nanofibers fabricated by electrospinning." *Materials Chemistry and Physics*, 99(1), 104–108.

Mahapatra, A., Mishra, B. G., and Hota, G. (2013). "Electrospun Fe_2O_3-Al_2O_3 nanocomposite fibers as efficient adsorbent for removal of heavy metal ions from aqueous solution." *Journal of Hazardous Materials*, 258–259, 116–123.

Malakhov, S. N., Khomenko, A. Y., Belousov, S. I., Prazdnichnyi, A. M., Chvalun, S. N., Shepelev, A. D., and Budyka, A. K. (2009). "Method of manufacturing Nonwovens by electrospinning from polymer melts." *Fibre Chemistry*, 41(6), 355–359.

Mallick, S., Ahmad, Z., Touati, F., and Shakoor, R. A. (2019). "Improvement of humidity sensing properties of PVDF-TiO_2 nanocomposite films using acetone etching." *Sensors and Actuators, B: Chemical*, 288(March), 408–413.

Man, C., Jiang, P., Wong, K., Zhao, Y., Tang, C., Fan, M., Lau, W., Mei, J., Li, S., Liu, H., and Hui, D. (2014). "Enhanced wetting properties of a polypropylene separator for a lithium-ion battery by hyperthermal hydrogen induced cross-linking of poly(ethylene oxide)." *J. Mater. Chem. A*, 2(30), 11980–11986.

Manna, S., and Nandi, A. K. (2007). "Piezoelectric β Polymorph in Poly(vinylidene fluoride)-Functionalized Multiwalled Carbon Nanotube Nanocomposite Films." *The Journal of Physical Chemistry C*, 111(40), 14670–14680.

Mansouri, S., Sheikholeslami, T. F., and Behzadmehr, A. (2019). "Investigation on the electrospun PVDF/NP-ZnO nanofibers for application in environmental energy harvesting." *Journal of Materials Research and Technology*, 8(2), 1608–1615.

Martins, P., Costa, C. M., Benelmekki, M., Botelho, G., and Lanceros-Mendez, S. (2012). "On the origin of the electroactive poly(vinylidene fluoride) β-phase nucleation by ferrite nanoparticles via surface electrostatic interactions." *CrystEngComm*, 14(8), 2807–2811.

Matysiak, W., Tański, T., and Zaborowska, M. (2018). "Electrospinning process and

characterization of PVP/hematite nanofibers." *IOP Conference Series: Materials Science and Engineering*, 461 (1), 012050.

McCann, J. T., Chen, J. I. L., Li, D., Ye, Z. G., and Xia, Y. (2006). "Electrospinning of polycrystalline barium titanate nanofibers with controllable morphology and alignment." *Chemical Physics Letters*, 424(1–3), 162–166.

Meng, M., Wu, S. X., Ren, L. Z., Zhou, W. Q., Wang, Y. J., Wang, G. L., and Li, S. W. (2014). "Enlarged Mn 3s splitting and room-temperature ferromagnetism in epitaxially grown oxygen doped $Mn_2N_{0.86}$ films." *Journal of Applied Physics*, 116(17), 173911.

Min, J. W., Yim, C. J., and Im, W. Bin. (2014). "Preparation and electrochemical characterization of flower-like $Li_{1.2}Ni_{0.17}Co_{0.17}Mn_{0.5}O_2$ microstructure cathode by electrospinning." *Ceramics International*, 40(1), 2029–2034.

Mistry, B. D. (1991). A Handbook of spectroscopic data chemistry (UV, IR, PMR, 13CNMR and mass spectroscopy). Annals of the Rheumatic Diseases, Oxford Book Co., Jaipur.

Moulder, J. F. (1992). Handbook of X-ray Photoelectron Spectroscopy: A Reference Book of Standard Spectra for Identification and Interpretation of XPS Data. Physical Electronics Division, Perkin-Elmer Corporation, Eden Prairie.

Muresan, L. M. (2015). "Corrosion Protective Coatings for Ti and Ti Alloys Used for Biomedical Implants." *Intelligent Coatings for Corrosion Control*, Butterworth-Heinemann, Boston, 585–602.

Nádherný, L., Jankovský, O., Sofer, Z., Leitner, J., Martin, C., and Sedmidubský, D. (2015). "Phase equilibria in the Zn–Mn–O system." *Journal of the European Ceramic Society*, 35(2), 555–560.

Nagai, N., Takeuchi, M., Kimura, T., and Oka, T. (2003). "Existence of optimum space between electrodes on hydrogen production by water electrolysis." *International Journal of Hydrogen Energy*, 28(1), 35–41.

Ngang, H. P., Ahmad, A. L., Low, S. C., and Ooi, B. S. (2017). "Preparation of

PVDF/SiO$_2$ composite membrane for salty oil emulsion separation: Physicochemical properties changes and its impact on fouling propensity." *IOP Conference Series: Materials Science and Engineering*, 206, 012083.

Nguyen, T. M. T., Ippili, S., Eom, J. H., Jella, V., Van Tran, D., and Yoon, S. G. (2018). "Enhanced Output Performance of Nanogenerator Based on Composite of Poly Vinyl Fluoride (PVDF) and Zn:Al Layered-Double Hydroxides (LDHs) Nanosheets." *Transactions on Electrical and Electronic Materials*, 19(6), 403–411.

Nor, N. A. M., Jaafar, J., Ismail, A. F., Mohamed, M. A., Rahman, M. A., Othman, M. H. D., Lau, W. J., and Yusof, N. (2016). "Preparation and performance of PVDF-based nanocomposite membrane consisting of TiO$_2$ nanofibers for organic pollutant decomposition in wastewater under UV irradiation." *Desalination*, 391, 89–97.

Ouyang, Z. W., Chen, E. C., and Wu, T. M. (2015). "Enhanced piezoelectric and mechanical properties of electroactive polyvinylidene fluoride/iron oxide composites." *Materials Chemistry and Physics*, 149, 172–178.

Padmanathan, N., and Selladurai, S. (2014). "Mesoporous MnCo$_2$O$_4$ spinel oxide nanostructure synthesized by solvothermal technique for supercapacitor." *Ionics*, 20(4), 479–487.

Park, J. Y., and Kim, S. S. (2009). "Growth of Nanograins in Electrospun ZnO Nanofibers." *Journal of the American Ceramic Society*, 92(8), 1691–1694.

Parangusan, H., Ponnamma, D., and AlMaadeed, M. A. A. (2018). "Investigation on the effect of γ-irradiation on the dielectric and piezoelectric properties of stretchable PVDF/Fe–ZnO nanocomposites for self-powering devices." *Soft Matter*, 14(43), 8803–8813.

Parra, M. R., and Haque, F. Z. (2014). "Aqueous chemical route synthesis and the effect of calcination temperature on the structural and optical properties of ZnO nanoparticles." *Journal of Materials Research and Technology*, 3(4), 363–369.

Patel, K. K., Paulsen, J. M., and Desilvestro, J. (2003). "Numerical simulation of porous

networks in relation to battery electrodes and separators." *Journal of Power Sources*, 122(2), 144–152.

Peiteado, M., Caballero, A. C., and Makovec, D. (2007). "Phase evolution of $Zn_{1-x}Mn_xO$ system synthesized via oxalate precursors." *Journal of the European Ceramic Society*, 27(13–15), 3915–3918.

Peng, H., and Wu, T. (2009). "Nonvolatile resistive switching in spinel $ZnMn_2O_4$ and ilmenite $ZnMnO_3$." *Applied Physics Letters*, 95(15), 2012–2015.

Perera, K., and Vidanapathirana, K. (2017). "Impedance spectroscopy, DC polarization, XRD and SEM studies on an ionic liquid based gel polymer electrolyte to be used for dye sensitized solar cells." *Materials Discovery*, 7, 30–33.

Ponnamma, D., Erturk, A., Parangusan, H., Deshmukh, K., Ahamed, M. B., and Al Ali Al-Maadeed, M. (2018). "Stretchable quaternary phasic PVDF-HFP nanocomposite films containing graphene-titania-$SrTiO_3$ for mechanical energy harvesting." *Emergent Materials*, 1(1–2), 55–65.

Priya, L., and Jog, J. P. (2003). "Polymorphism in Intercalated Poly(vinylidene fluoride)/ Clay Nanocomposites." *Journal of Applied Polymer Science*, 89, 2036.

Qi, Q., Zhang, T., Liu, L., and Zheng, X. (2009). "Synthesis and toluene sensing properties of SnO_2 nanofibers." *Sensors and Actuators, B: Chemical*, 137(2), 471–475.

Qin, W., Xu, L., Song, J., Xing, R., and Song, H. (2013). "Highly enhanced gas sensing properties of porous SnO_2-CeO_2 composite nanofibers prepared by electrospinning." *Sensors and Actuators, B: Chemical*, 185, 231–237.

Raja, M., and Stephan, A. M. (2014). "Natural, biodegradable and flexible egg shell membranes as separators for lithium-ion batteries." *RSC Adv.*, 4(102), 58546–58552.

Rajesh, J. A., Min, B. K., Kim, J. H., Kang, S. H., Kim, H., and Ahn, K. S. (2017). "Facile hydrothermal synthesis and electrochemical supercapacitor performance of hierarchical coral-like $ZnCo_2O_4$ nanowires." *Journal of Electroanalytical Chemistry*, 785, 48–57.

Ramakrishna, S., Fujihara, K., Teo, W. E., Lim, T. C., and Ma, Z. (2005). *An introduction to electrospinning and nanofibers*. *An Introduction to Electrospinning and Nanofibers*, World Scientific, Singapore.

Reneker, D. H., and Chun, I. (1996). "Nanometre diameter fibres of polymer, produced by electrospinning." *Nanotechnology*, 7(3), 216–223.

Sachin Kumar, B., Tarafder, K., Shetty, A. R., Hegde, A. C., Gudla, V. C., Ambat, R., Kalpathy, S. K., and Anandhan, S. (2019). "Polymorph nickel titanate nanofibers as bifunctional electrocatalysts towards hydrogen and oxygen evolution reactions." *Dalton Transactions*, 48(33), 12684–12698.

Samanta, K., Dussan, S., Katiyar, R. S., and Bhattacharya, P. (2007). "Structural and optical properties of nanocrystalline $Zn_{1-x}Mn_xO$." *Applied Physics Letters*, 90(26), 261903.

Sambandam, B., Michael, R. J. V., and Manoharan, P. T. (2015). "Oxygen vacancies and intense luminescence in manganese loaded ZnO microflowers for visible light water splitting." *Nanoscale*, 7(33), 13935–13942.

Sebastian, M. S., Larrea, A., Gonçalves, R., Alejo, T., Vilas, J. L., Sebastian, V., Martins, P., and Lanceros-Mendez Ag B-Poly, S. (2016). "Understanding nucleation of the electroactive β-phase of poly(vinylidene fluoride) by nanostructures." *RSC Advances,* 6, 113007.

Senthil, T., and Anandhan, S. (2014). "Structure–property relationship of sol–gel electrospun ZnO nanofibers developed for ammonia gas sensing." *Journal of Colloid and Interface Science*, 432, 285–296.

Shamitha, C., Senthil, T., Wu, L., Kumar, B. S., and Anandhan, S. (2017). "Sol–gel electrospun mesoporous $ZnMn_2O_4$ nanofibers with superior specific surface area." *Journal of Materials Science: Materials in Electronics*, 28, 15846–15860.

Shao, C., Guan, H., Liu, Y., Li, X., and Yang, X. (2004). "Preparation of Mn_2O_3 and Mn_3O_4 nanofibers via an electrospinning technique." *Journal of Solid State Chemistry*,

177(7), 2628–2631.

Shepelin, N. A., Glushenkov, A. M., Lussini, V. C., Fox, P. J., Dicinoski, G. W., Shapter, J. G., and Ellis, A. V. (2019). "New developments in composites, copolymer technologies and processing techniques for flexible fluoropolymer piezoelectric generators for efficient energy harvesting." *Energy and Environmental Science*, 12(4), 1143–1176.

Shetty, S., Ekbote, G. S., Mahendran, A., and Anandhan, S. (2019). "Polymorphism, dielectric and piezoelectric response of organo-modified Ni–Co layered double hydroxide nanosheets dispersed electrospun PVDF nanofabrics." *Journal of Materials Science: Materials in Electronics*, 30, 20703–20715.

Shi, K., Sun, B., Huang, X., and Jiang, P. (2018). "Synergistic effect of graphene nanosheet and BaTiO3 nanoparticles on performance enhancement of electrospun PVDF nanofiber mat for flexible piezoelectric nanogenerators." *Nano Energy*, 52, 153–162.

Singh, H. H., Singh, S., and Khare, N. (2018). "Enhanced β-phase in PVDF polymer nanocomposite and its application for nanogenerator." *Polymers for Advanced Technologies*, 29(1), 143–150.

Sing, K. S. W. (2009). "Reporting physisorption data for gas/solid systems with special reference to the determination of surface area and porosity (Recommendations 1984)." *Pure and Applied Chemistry*, 57(4), 603–619.

Song, W.-J., Joo, S. H., Kim, D. H., Hwang, C., Jung, G. Y., Bae, S., Son, Y., Cho, J., Song, H.-K., Kwak, S. K., Park, S., and Kang, S. J. (2017). "Significance of ferroelectric polarization in poly (vinylidene difluoride) binder for high-rate Li-ion diffusion." *Nano Energy*, 32, 255–262.

Stafiniak, A., Boratyński, B., Baranowska-Korczyc, A., Szyszka, A., Ramiczek-Krasowska, M., Pramowska, J., Fronc, K., Elbaum, D., Paszkiewicz, R., and Tłaczała, M. (2011). "A novel electrospun ZnO nanofibers biosensor fabrication." *Sensors and Actuators, B: Chemical*, 160(1), 1413–1418.

Sun, D., Chang, C., Li, S., and Lin, L. (2006). "Near-Field Electrospinning." *Nano Letters*, 6(4), 839–842.

Tang, Q., Jiang, L., Liu, J., Wang, S., and Sun, G. (2014). "Effect of Surface Manganese Valence of Manganese Oxides on the Activity of the Oxygen Reduction Reaction in Alkaline Media." *ACS Catalysis*, 4(2), 457–463.

Tauc, J. (1970). "Absorption edge and internal electric fields in amorphous semiconductors." *Materials Research Bulletin*, 5(8), 721–729.

Taylor, G., and Dyke, M. D. Van. (1969). "Electrically driven jets." *Proceedings of Royal Society of London. A*, 313, 453–475.

Tian, R., Xu, Q., Lu, C., Duan, X., and Xiong, R.-G. (2017). "Spontaneous polarization switching and piezoelectric enhancement of PVDF through strong hydrogen bonds induced by layered double hydroxides." *Chemical Communications*, 53(56), 7933–7936.

Veerabhadraiah, A., Ramakrishna, S., Angadi, G., Venkatram, M., Kanivebagilu Ananthapadmanabha, V., Hebbale NarayanaRao, N. M., and Munishamaiah, K. (2017). "Development of polyvinyl acetate thin films by electrospinning for sensor applications." *Applied Nanoscience,* 7(7), 355–363.

Vijayakumar, G. N. S., Devashankar, S., Rathnakumari, M., and Sureshkumar, P. (2010). "Synthesis of electrospun ZnO/CuO nanocomposite fibers and their dielectric and non-linear optic studies." *Journal of Alloys and Compounds*, 507(1), 225–229.

Wang, C., Hsieh, T.-C., and Cheng, Y.-W. (2010). "Solution-Electrospun Isotactic Polypropylene Fibers: Processing and Microstructure Development during Stepwise Annealing." *Macromolecules*, 43(21), 9022–9029.

Wang, M., Bao, W. J., Wang, J., Wang, K., Xu, J. J., Chen, H. Y., and Xia, X. H. (2014). "A green approach to the synthesis of novel 'Desert rose stone'-like nanobiocatalytic system with excellent enzyme activity and stability." *Scientific Reports*, 4, 1–8.

Wang, Y., Aponte, M., Leon, N., Ramos, I., Furlan, R., Evoy, S., and Santiago-Avilés,

J. J. (2004). "Synthesis and characterization of tin oxide microfibres electrospun from a simple precursor solution." *Semiconductor Science and Technology*, 19(8), 1057–1060.

Wang, Y. R., Zheng, J. M., Ren, G. Y., Zhang, P. H., and Xu, C. (2011). "A flexible piezoelectric force sensor based on PVDF fabrics." *Smart Materials and Structures*, 20(4).

Wang, Z. L., and Song, J. (2006). "Piezoelectric nanogenerators based on zinc oxide nanowire arrays." *Science*, 312(5771), 242–246.

Writer, B. (2019). "Lithium-Ion Batteries: A Machine-Generated Summary of Current Research." *Lithium-Ion Batteries*, Springer, Cham.

Wu, H., Lin, D., Zhang, R., and Pan, W. (2007). "Facile Synthesis and Assembly of Ag/NiO Nanofibers with High Electrical Conductivity." *Chemistry of Materials*, 19(8), 1895–1897.

Wu, Q. Y., Liang, H. Q., Gu, L., Yu, Y., Huang, Y. Q., and Xu, Z. K. (2016). "PVDF/PAN blend separators via thermally induced phase separation for lithium ion batteries." *Polymer*, 107, 54–60.

Xiang, H. F., Jin, Q. Y., Chen, C. H., Ge, X. W., Guo, S., and Sun, J. H. (2007). "Dimethyl methylphosphonate-based nonflammable electrolyte and high safety lithium-ion batteries." *Journal of Power Sources*, 174(1), 335–341.

Xue, X., Deng, P., Yuan, S., Nie, Y., He, B., Xing, L., and Zhang, Y. (2013). "CuO/PVDF nanocomposite anode for a piezo-driven self-charging lithium battery." *Energy & Environmental Science*, 6(9), 2615.

Yan, L., Hong, S., Li, M. L., and Li, Y. S. (2009). "Application of the Al_2O_3-PVDF nanocomposite tubular ultrafiltration (UF) membrane for oily wastewater treatment and its antifouling research." *Separation and Purification Technology*, 66(2), 347–352.

Yang, G., Xu, X., Yan, W., Yang, H., and Ding, S. (2014a). "Facile synthesis of interwoven ZnMn2O4 nanofibers by electrospinning and their performance in Li-ion

batteries." *Materials Letters*, 128, 336–339.

Yang, X., Shao, C., Liu, Y., Mu, R., and Guan, H. (2005). "Nanofibers of CeO2 via an electrospinning technique." *Thin Solid Films*, 478(1–2), 228–231.

Yang, Z., and Xu, B. (2007). "Supramolecular hydrogels based on biofunctional nanofibers of self-assembled small molecules." *Journal of Materials Chemistry*, 17(23), 2385–2393.

Zhang, P., Li, X., Zhao, Q., and Liu, S. (2011). "Synthesis and optical property of one-dimensional spinel ZnMn$_2$O$_4$ nanorods." *Nanoscale Research Letters*, 6(1), 323.

Zhang, T., Yue, H., Qiu, H., Zhu, K., Zhang, L., Wei, Y., Du, F., Chen, G., and Zhang, D. (2015). "Synthesis of graphene-wrapped ZnMn$_2$O$_4$ hollow microspheres as high performance anode materials for lithium ion batteries." *RSC Adv.*, 5(120), 99107–99114.

Zhang, X., and Lu, Y. (2014). "Centrifugal Spinning: An Alternative Approach to Fabricate Nanofibers at High Speed and Low Cost." *Polymer Reviews*, 54(4), 677–701.

Zhang, Y., He, X., Li, J., Miao, Z., and Huang, F. (2008). "Fabrication and ethanol-sensing properties of micro gas sensor based on electrospun SnO$_2$ nanofibers." *Sensors and Actuators, B: Chemical*, 132(1), 67–73.

Zhang, Z., Shao, C., Li, X., Wang, C., Zhang, M., and Liu, Y. (2010a). "Electrospun nanofibers of p-type NiO/ n-type ZnO heterojunctions with enhanced photocatalytic activity." *ACS Applied Materials and Interfaces*, 2(10), 2915–2923.

Zhang, Z., Shao, C., Li, X., Zhang, L., Xue, H., Wang, C., and Liu, Y. (2010b). "Electrospun nanofibers of ZnO-SnO$_2$ heterojunction with high photocatalytic activity." *Journal of Physical Chemistry C*, 114(17), 7920–7925.

Zhao, M., Cai, B., Ma, Y., Cai, H., Huang, J., Pan, X., He, H., and Ye, Z. (2014). "Self-assemble ZnMn$_2$O$_4$ hierarchical hollow microspheres into self-supporting architecture for enhanced biosensing performance." *Biosensors and Bioelectronics*, 61, 443–447.

Zhou, H., Ding, X., Yin, Z., Xu, G., Xue, Q., Li, J., Jiao, S., and Wang, X. (2014). "Fabrication and electrochemical characteristics of electrospun $LiMn_2O_4$ nanofiber cathode for Li-ion batteries." *Materials Letters*, 117, 175–178.

Zhu, M., Lan, J., Tan, C., Sui, G., and Yang, X. (2016). "Degradable cellulose acetate/poly- l -lactic acid/halloysite nanotube composite nanofiber membranes with outstanding performance for gel polymer electrolytes." *Journal of Materials Chemistry A*, 4(31), 12136–12143.

Zhu, Y., Wang, F., Liu, L., Xiao, S., Yang, Y., and Wu, Y. (2013). "Cheap glass fiber mats as a matrix of gel polymer electrolytes for lithium ion batteries." *Scientific Reports*, 3(1), 3187.

Zong, X., Kim, K., Fang, D., Ran, S., Hsiao, B. S., and Chu, B. (2002). "Structure and process relationship of electrospun bioabsorbable nanofiber membranes." *Polymer*, 43(16), 4403–4412.

BIO-DATA

SHAMITHA C

Permanent address:

> Nallakkandiyil house,
> PO Pinarayi,
> Kannur-670741
> Kerala, INDIA.

Contact Details:

> Email ✉: shamithac2@gmail.com
>
> Phone ▯ : +91-9447004652

Academic Qualifications:

> Master of Technology in Nanoscience and Technology (2014) from Pondicherry University, Puducherry, India.
>
> Bachelor of Technology in Electronics and Communication Engineering (2011) from Kannur University, Kerala, India.

Research publications:

> Articles in International Journals: 03
> Articles in the Pipeline: 01
> Articles in Conference Proceedings: 02

List of publications based on Ph.D Research Work

In peer-reviewed journals:

Published:

- Shamitha, C., Senthil, T., Wu, L., Kumar, B. S., and Anandhan, S. (2017). "Sol–gel electrospun mesoporous $ZnMn_2O_4$ nanofibers with superior specific surface area." *Journal of Materials Science: Materials in Electronics*, 28, 15846–15860.

- Shamitha, C., Mahendran, A., and Anandhan, S. (2019). "Effect of polarization switching on piezoelectric and dielectric performance of electrospun nanofabrics of poly(vinylidene fluoride)/Ca–Al LDH nanocomposite." *Journal of Applied Polymer Science*, 48697, 1–12.

- Shamitha, C., Shetty, A. R., Hegde, A. C., and Anandhan, S. (2019b). "Sol-gel electrospun $ZnMn_2O_4$ nanofibers as bifunctional electrocatalysts for hydrogen and oxygen evolution reactions." *Materials Research Express*, 6(11).

In pipeline:

- Shamitha, C., Janakiraman, S., Ghosh, S., Venimadhav, A., Prabhu, K.N., Anandhan, S. "PVDF/Ca-Al layered double hydroxide composite gel polymer electrolyte for high-performance Li-ion batteries".

In conference proceedings:

- Shamitha, C., Senthil, T., Wu, L., Kumar, B. S., and Anandhan, S. "Structural and morphological characterization of $ZnMn_2O_4$ nanofibers obtained by sol-gel electrospinning." *International Conference on 'Nanoscience and Technology' (ICONSAT-2018), CeNS, Bengaluru, India, March 2018.*

- Shamitha, C., Mahendran, A., and Anandhan, S. "Enhanced piezoelectric and dielectric performance of PVDF Nanofibers via polarization switching due to the cooperative effect of layered double hydroxide nanosheets and *in situ* Stretching by electrospinning," *International Conference on 'Advancements in Polymeric Materials APM-2019', CIPET-Chennai, India, January 2019.*